Domain Wall Motion and Magnetization Switching Driven by Magnetic/Laser Fields

Yichuan Wang

Doctor of Philosophy

University of York

Physics

September 2018

Abstract

The work presented in this thesis mainly focus on the domain wall motion in planar Permalloy nanowires and magnetization switching in ferromagnetic Co/Pt thin films studied with both static Kerr imaging and dynamic pump and probe time-resolved magneto-optical Kerr effect (TR-MOKE) measurement techniques. The aim is to provide insightful support for the future novel data storage devices based on magnetic nanostructures. A spatially resolved wide-field magneto-optical Kerr imaging system has been successfully built during this project. The dependence of the coercivity of the Permalloy nanowires on different notch depth and geometries have been investigated systematically. The results show that the depinning field is strongly dependent on the detailed notch geometry. We have found that even the notches with same triangular feature, but different orientations will have a large depinning field difference. Our micromagnetic simulations support the experimental observations and show the correlation between the notch geometry, and the domain wall pinning and depinning processes. The laser-induced precession dynamics in Co/Pt thin films with multiple layers have been investigated by pump and probe TR-MOKE. By fitting the experimental curves via phenomenological formula, the effective Gilbert damping constants α_{eff} are retrieved. The results show that α_{eff} has a significant external field and layer repetition number dependences. The more Co/Pt layer repeats number, the higher value of α_{eff}. This enhancement of the α_{eff} value with more Co/Pt layer repeats could be due to the interfacial effect or decoherence. As the lattice mismatching in the Co/Pt structures increases with the thickness, the increased dislocation may promote electron hopping between two different sites which enhances the intrinsic damping in the thicker films. Combing the TR-MOKE system with the Kerr imaging, the magneto-optical responses of the ferromagnetic Co/Pt films with different Co thicknesses under the action of femtosecond laser beam have been explored systematically. We have developed a new approach to study the helicity dependence in the all optical switching (AOS) by varying the degree of helicity. Our results demonstrate unambiguously that the laser helicity plays an essential role in the AOS. We have further established a detailed relationship between domain switching percentage and the degree of the pumping laser helicity.

Contents

List of Figures

List of Tables

Acknowledgements

Firstly, I would like to sincerely thank to my supervisors Dr. Jing Wu and Prof. Yongbing Xu, for their guidance in academy and support in life, without their help, I would not be where I am today, my gratitude is far beyond words.

I would like to thank my thesis advisor Prof. Nigel Woolsey and Prof. Sarah Thompson for their inspirations and kind suggestions. Also, I appreciate all the technicians and support staffs, they are Dr. Iain Will, Dr. Jon Barnard, Mr. Jonathan Creamer, Mr. Ian Wright, who providing professional technical assistance to my projects.

I would like to thank my colleagues and friends, for those wonderful and unforgettable days we spend together. I would like to thank Mr. Xianyang Lu and Mr. Xiangyu Zheng for providing help with the experiments, Mr. Junlin Wang for instructing me to do image analysis and Mr. Guanqi Li for useful discussions about the theory.

Most importantly, I would like to give the endless grateful to my beloved family, for their selfless dedication and encouragement, they are the reason that keep me motivated throughout all the difficulties.

Declaration of Authorship

I declare that this thesis titled, “Domain Motion and Magnetization Switching Driven by Magnetic/Laser Fields”, and the work presented in it are my own. I confirm that: This work was done wholly or mainly while in candidature for a research degree at University of York and has not been submitted previously for a degree at this or any other university.

All sources are acknowledged as references. I am responsible for all the research work described in this thesis except for the following collaborations: the Permalloy nanowire samples were designed by myself and fabricated by Dr. Li Chen. The Co/Pt samples are provided by Prof. Jianwang Cai.

Chapter 1 Introduction

1.1 Developing of Magnetism and Magnetic Storage Devices

Magnetism is one of the oldest areas of Physics research. The first discovery of a magnetic material is not documented, though it is thought to have occurred in Ancient Greece, in a region of Greece called Magnesia. The phenomena of magnetism are believed to have gained its name from this area and the magnetic material would have been discovered as a lodestone [1], a naturally occurring magnetized magnetite. The first ever record describing the use of a magnetic compass is in a book by Shen Kuo, written in the 11^{th} century [2]. The book describes how a steel needle could be magnetized by being rubbed with a lodestone. By then hanging this magnetized needle from a silk strand it was observed that the needle orientated either north or south. We now know that this is a result of the magnetic moments inside the magnetized needle trying to align themselves with the Earth's own magnetic field. However, although the compass has greatly helped adventurers to explore the world, the application of magnetism was limited prior to the 19^{th} century. Before then no other practical uses for magnetic materials were found and the origin of their magnetism remained shrouded in mystery.

That was the situation until 1820, when Hans Christian Oersted, after whom the CGS unit of magnetic field (H) is named, discovered the link between magnetism and electricity. Oersted noticed that a magnetic needle moved when a current carrying wire was placed close to it and that the effect was not significantly diminished by placing barriers, such as glass or wood, between the wire and the needle [3]. A modern understanding of magnetic phenomena in condensed matter was considerably developed by Pierre Curie and Pierre Weiss in the early 1900s, as research works in magnetism became more systematic and intense due to its enormous potential of its applications. The present day understanding of magnetism is based on the theory of the motion and interactions of electrons in the atoms known as quantum electrodynamics. This stems from the work and theoretical models of Ernest Ising and Werner Heisenberg. The earliest application of magnetism as an information storage medium was in 1888, when Oberlin Smith invented magnetic wire recording. Several

decades later, Fritz Pfleumer invented magnetic tape as a means of storing audio information, which revolutionised audio recording, reproduction and broadcasting [4].

Consequently, people gradually began to pay more attention to magnetic storage technology over the following years. More recently, Professor Peter Grünberg and Professor Albert Fert independently found that the resistance of a multilayer structure was greatly dependent on an applied field, known as the Giant Magnetoresistance Effect (GMR). The magnetoresistance ratio (MR ratio) of the typical sandwich structure used, consisting of two ferromagnetic (FM) layers separated by a thin non-magnetic layer (NM), can easily reach around 80% for such a simple Fe/Cr/Fe multilayer [5]. For their significant contribution, Prof. Grünberg and Prof. Fert were jointly presented with the 2007 Nobel Prize in Physics, and the discovery of GMR triggered a revolutionary development in a brand-new field in magnetism, spin transport electronics, known as spintronics.

Spintronics, now a rapidly expanding branch of research, aims to exploit spin properties, in addition to the charge degrees of freedom utilised in solid state physics and related devices. In future years, the use of recording devices is predicted to increase substantially, due to the information explosion and the data carrier revolution. As a consequence, this rapidly and greatly expanding market demands non-volatile, high density, fast access time storage with low power consumption. Such a proposition requires decades of fundamental research and debate, extensive development of correlated industries, and, unavoidably, huge investment. One possibility might be to utilise the intrinsic angular momentum, or the spin, of an electron as an extra degree of freedom within electronic devices. With the evolution of storage devices since the discovery of GMR effect, hard disk drive (HDD) areal density (AD) has been improved by seven orders of magnitude and HDD prices have decreased drastically, by about five orders of magnitude [6].

As can be seen in Figure 1, from 1980 to 1990, HDD areal density increased at a rate of 25% per year. From 1990 to 1997, AD almost doubled every two years, due to the introduction of thin film media and magnetoresistive (MR) sensors. After the appearance of the giant-magnetoresistance (GMR) head, created by IBM in 1998, AD grew even more quickly than before, reaching over 12 Gb/in^2 in 2000 [7]. In the

previous five decades, the data storage industry had focused exclusively on a method called longitudinal magnetic recording. In this method the magnetization of each data bit is aligned horizontally in the disk. Storage capacity was largely increased with longitudinal recording by shrinking the size of the magnetic grains in each data bit - as the magnetic grains became smaller, more data could be stored on the same area of the disk. Unfortunately, the reduction of the grain size cannot be continued indefinitely, due to superparamagnetic limits, which refers to the fluctuation of magnetization triggered by thermal agitation. When the area density of a longitudinal medium reaches over 100 Gb/in^2, the magnetic energy holding the bits in place on the medium becomes comparable to the ambient thermal energy within the disk drive itself. As a result, the magnetization of the tiny bits will no longer stay fixed in a reliable state and may flip between one another's magnetization state, thus causing data loss [8].

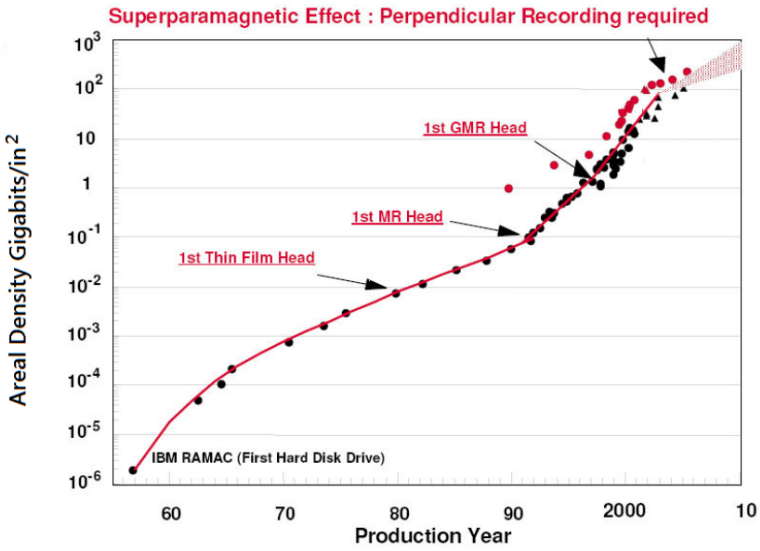

Figure 1. The history of data storage density of HDD Drive [6].

As indicated in Figure 1, the rate of increase of areal density started to slow down after 2003 due to this superparamagnetic limit in longitudinal media. Therefore, conventional longitudinal recording no longer satisfies the enormous demand for high density media. As a result, new materials and techniques needed to be applied. One of the most important candidates was perpendicular media, which was predicted to have a potential AD around ten times greater than the maximum capacity in longitudinal recording, owing to geometry and coercivity advantages. In 2005, Toshiba Corporation announced the world's first commercial HDD based on perpendicular

recording. It was a ground-breaking technology that set new benchmarks for data density, boosting the capacity of a single 1.8 inch hard-disk platter to 320 gigabits [9]. Over the years immediately following the Toshiba Corporation's invention of HDD with perpendicular recording, storage drives with densities of 300-400Gb/in^2 were becoming available commercially. As a result, by 2010, most of the high capacity drives were perpendicular based drives. A comparison between longitudinal and perpendicular recording technology is presented in Figure 2.

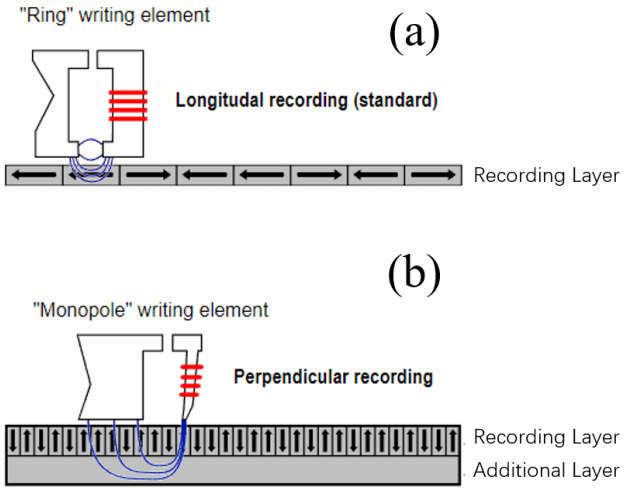

Figure 2. Cross-section of longitudinal and perpendicular recoding technology [9].

Looking more closely at the inside of a typical data storage device, it can be seen that a large number of small grains are magnetized together to form a single data bit. This results in the internal signal to noise ratio (SNR) being dominated by transition noise, originating from irregularities or jaggedness in the magnetization transitions between the adjacent grains [10]. According to the statistical nature of grain size and the easy magnetization axis of polycrystalline grains in a magnetic medium, the intrinsic SNR of a magnetic signal in a recording system can be approximately calculated by SNR(dB)=10log$N$ [11], where N is the number of grains in a bit. In an acceptable range of SNR (20dB-30dB), each bit must contain a minimum of 100-1000 grains [12]. The most effective way to increase the areal density of recording media would be to reduce the grain size. However, it is impossible to maintain the magnetization state in a very tiny grain due to thermal fluctuations. The characteristic relaxation time τ for the thermal activity over the energy barriers is given by [13]:

$$\tau = {f_0}^{-1} e^{\frac{E_B}{K_B T}} \tag{1.1}$$

where f_0 is the attempt frequency which is around10^9 to10^{12} Hz, k_B is Boltzmann's constant and T is the ambient temperature, and E_B is the magnitude of the energy barrier. This is defined as follows [14]:

$$E_B = K_u V \left(1 - \frac{H}{H_0}\right)^n \tag{1.2}$$

where K_u is the anisotropy constant, n is between 1.5 and 2.0 depending on geometrical and other factors, V is the grain volume and H_0 is the intrinsic switching field from the anisotropy system. The grains become unstable when the ratio of magnetic energy (K_uV), to thermal energy (k_BT), drops below a certain value [15]. Equation 1.2 reveals that the energy required to reverse the magnetization of a grain is proportional to its size and the magnetic coercivity of the material, while inversely proportional to the temperature. The larger the grain size and the higher the magnetic coercivity of the material, the more stable the medium becomes. For long-term stability of a grain, the value of K_uV/k_BT must be greater than 40 in a non-magnetic environment [10]. But for practical purposes, the stability ratio K_uV/k_BT is commonly required to be larger than 40-80 owing to the effects of the distribution of grains, intergranular coupling, saturation magnetization and other 5 properties of the media [13].

Based on the discussion above, one potential solutions for high density recording is to use small grain materials with high anisotropy, which refers to high coercivity. The grain of a perpendicular medium has a small diameter and large length, due to the geometry advantage, so the demagnetization field favours transition in perpendicular materials. Consequently, the perpendicular media have fewer critical non-linear transition shifts with higher thermal stability and areal density compared to longitudinal magnetic media [16]. Because of the high anisotropy, the perpendicular magnetic media grains have a strong orientation, which leads to less medium noise, sharper recorded transition and higher side-track writing capability [17]. Overall, perpendicular magnetic media has proven to be ideally suited for high density recording and as such it plays a crucial role when coping with the increasing demand for hard drive storage.

The requirements for magnetic recording are high areal density of recording media and the fast-internal transfer rate of recording device. As such magnetoresistive random-access memory (MRAM) becomes one of the strongest candidates for the next generation of storage devices. MRAM has exhibited many advantages as a fast, low-power, high-endurance, non-volatile memory form that can be integrated with a complementary metal-oxide semiconductor (CMOS) [18].

The read-out process of MRAM bits is performed based on the tunnelling magnetoresistance (TMR) effect in the magnetic tunnel junctions (MTJs) [19, 20]. TMR is similar to GMR devices, but while MTJs also have a sandwich like structure, the free layer and pinned layer are separated by an insulator (such as MgO) which acts as the tunnelling barrier.

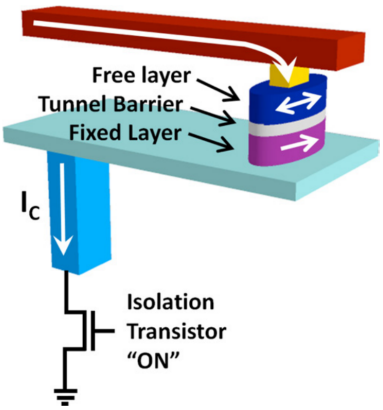

Figure 3.Typical architecture for a 1 transistor—1 MTJ memory cell. The MTJ is composed of a bi-stable free layer and a pinned layer separated by a tunnelling oxide [21].

The magnetoresistance ratio of the TMR effect has been reported at up to 604%, which is much greater than the value GMR effect [22, 23]. Therefore, the latest HDD read heads have replaced GMR with TMR heads to increase storage performance. In terms of the writing process in MRAM, the latest technology being applied to switch the magnetization of the free layer is to use spin-polarized currents via a spin transfer torque (STT) effect [24, 25]. The most important parameter in the writing process is the threshold current density (J_c), which is proportional to the magnetic damping constant (α) [26]. Thus, the study of the magnetization dynamics in magnetic materials, especially magnetic damping, is important for further understanding and designing MRAM devices with better performance.

To understand the fundamental limitations and the switching process of magnetic recording media, a detailed investigation of the theoretical background of magnetization dynamics is required. There are two important magnetization dynamics excited by different stimuli. One is the precessional magnetization dynamics triggered by an applied external magnetic field. The other is laser-induced magnetization dynamics, including ultrafast demagnetization and the magneto-optical effect, dominated by the interaction between light and magnetization. The rest of this chapter will give the basic framework of related fields from four aspects: domain wall motion and its applications; ultrafast demagnetization; laser induced magnetization procession; and all-optical switching.

1.2 Time Scales in Magnetism

The time scale for magnetization dynamics varies from the extremely long - from the billions of years connected to geological events such as the reversal of the earth magnetic poles - to the femtosecond time regime connected to the exchange interaction between two electron spins [27]. The demand for an ever-increasing speed of storage of information in magnetic media and the intrinsic limitations that relate to the generation of magnetic field pulses by current, have triggered intense interest in finding a new approach to manipulate magnetization by means of more than mere magnetic fields. Traditionally, magnetic storage devices have all used an external magnetic field or spin-polarized current to reverse the magnetization of magnetic logic bits. The time scale of this is normally measured in nanoseconds, which involves the domain wall motion and magnetic precession, and the magnetic precession time scale (10^{-10}–10^{-9} s) is considered to set the limiting time scale for field-driven magnetization reversal. Since Beaurepaire *et al* first demonstrated sub picosecond demagnetization by a 60 fs laser pulse in 1996 [28], manipulating the magnetization with ultrashort laser pulses has become a new challenge. Femtosecond laser pulses offer an intriguing possibility: to probe a magnetic system on a time scale that corresponds to the exchange interaction (10^{-15} s), which is responsible for the existence of magnetic order, while being much faster than the time scale of spin-orbit interaction (10^{-12}–10^{-11} s) or magnetic precession [29]. Consequently, the option of femtosecond laser excitation leads to the question of whether it would be possible to reverse magnetization faster than within half a precessional period.

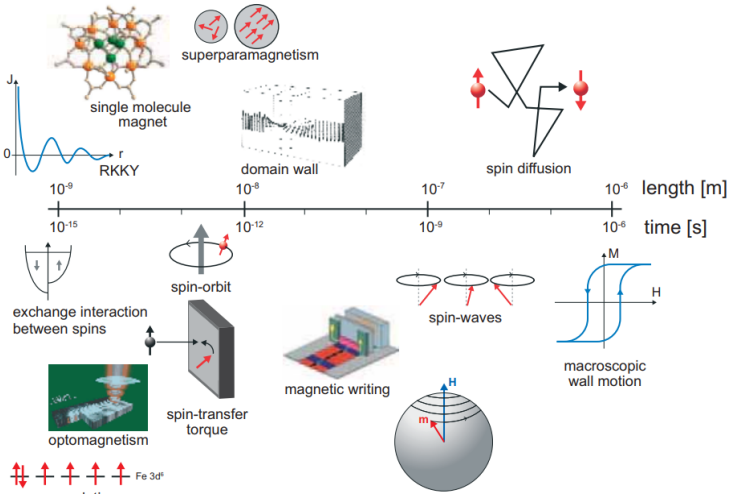

Figure 4. Time and length scales in magnetism [27].

1.3 Applications of Domain Walls motion

One of the most important scientific topics in the study of magnetism regards domain walls (DWs) motion. Domain walls are omnipresent in magnetic materials. Different types of DWs exist at the interfaces between regions of oppositely aligned magnetization and separate the magnetic domains, such as Néel walls, where the spins rotate within the film plane, and Bloch walls, where the spins point out of the film plane [30]. Nowadays, the DWs motion in nanowires and the relationship between thermal fluctuation, pinning and depinning of DWs have attracted lots of attention due to the potential applications for magnetic storage. The manipulation of the DWs motion in a magnetic material is the key to make the next generation of high-level technology realistic. Patterned magnetic nanowires is one suitable candidate for data storage and logic devices, which would allow non-volatile, fast switching times and low power consumption for the data storage purpose.

In 2005, Allwood *et al* proposed a magnetic logic architecture termed 'domain wall logic'. This uses no transistors, shows great simplicity and exhibits very little heat increase caused by data switching [31]. They suggest that the circuits of semiconductor electronics devices could be completely constructed using in-planar magnetic wires with submicron widths. Figure 5 gives an illustration of domain wall logic gate designs. The operating principle of the magnetic logic gate uses an in-plane rotating field which acts as both clock and power supply. The DWs propagate through the nanowires and the high shape anisotropy of the nanowires ensure the magnetization prefers to align with the long axis of the nanowires. Compared with the traditional logic gates based on transistors, domain logic gates have a simpler geometric design and can be integrated together into one circuit for the performance of any computational calculation purpose, which offers high integration densities with lower power dissipation.

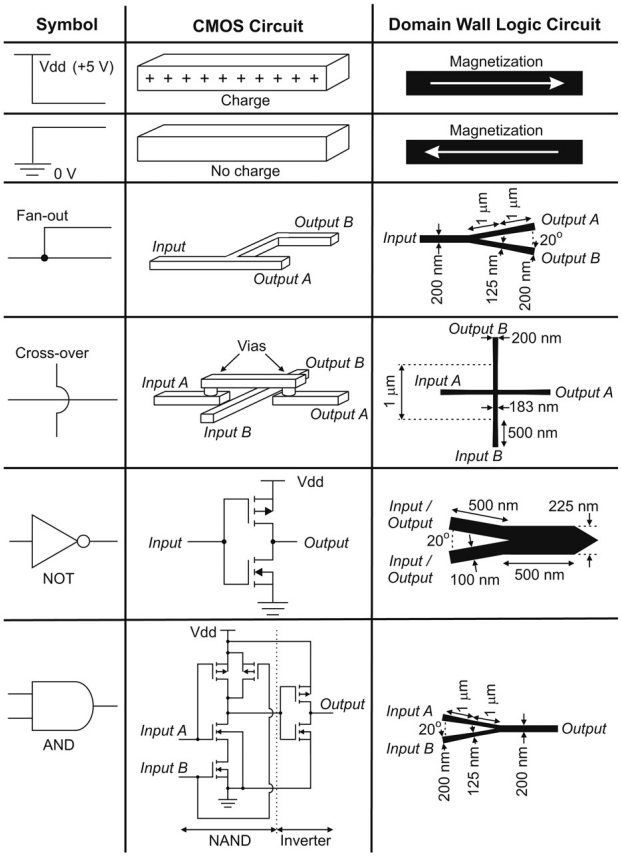

Figure 5. Symbols for electronic logic gate, together with the appropriate CMOS circuit element and a schematic drawing of the optimised domain-wall logic element [31].

Besides the domain wall logic gate devices, there is another potential application based on the motion of DWs in nanowires. Parkin *et al* (2008) suggested one completely new concept for magnetic data storage [32]. This was a revolutionary three-dimensional memory device with low cost but high performance and reliability, based on domain walls motion. Racetrack memory, as it is known, uses magnetic DWs to store information in tall columns of magnetic material, arranged perpendicularly on the surface of a silicon wafer. The racetrack consists of a ferromagnetic nanowire, with data information encoded as a pattern of magnetic domains along a portion of the wire, in which successive DWs along the racetrack alternate between head-to-head and tail-to-tail configurations. The spacing between consecutive DWs, namely the bit length, is controlled by pinning sites (notches) fabricated along the racetrack.

To control the DWs motion, pulses of highly spin-polarized current move the entire pattern of DWs coherently along the wire, forward and backward, to pass the read and write elements. The wires are twice the length of the stored DWs pattern,

therefore the motion of the DWs can be bidirectional. In racetrack memory, uniform magnetic field cannot be used to shift the pattern of DWs along the wire, as the neighbouring DWs would move in opposite direction, and thus annihilate one another. Here, Figure 6 gives a schematic architecture of racetrack memory, both vertically (a) and horizontally (b). The vertical configuration offers the highest density, by storing the pattern in a U-shape nanowire normal to the substrate surface, controlling the DWs motion through a three-dimensional regime. The horizontal configuration has the nanowires parallel to the substrate surface, with each track serviced by one read and write element, making access time, potentially, highly competitive.

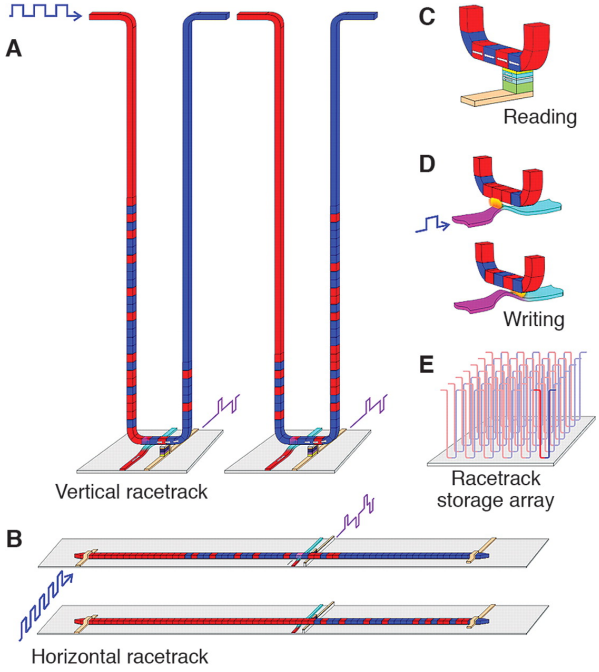

Figure 6. Schematics of racetrack memory, (A) demonstration of vertical configuration, (B) demonstration of horizontal configuration, (C) data are read by measuring the tunnel magnetoresistance of a MTJ connected to the racetrack, (D) writing data by a fringing field of a DW moved in a second ferromagnetic nanowire oriented at right angles to the storage nanowire, (E) arrays of vertical racetracks on a chip [32].

Recently, the propagation of the DWs in Permalloy nanowires for shift register memory and logic circuits has been successfully demonstrated. Permalloy is considered to be a potential candidate for the next generation of DWs based storage devices, due to its clear superiority in controlling the DWs motion. However, no matter what application is proposed, the DWs motion and their interaction with the ambient environment is a study of great importance.

1.4 Laser-Induced Magnetization Dynamics

In magnetic memory devices, the logical bits "1" and "0" are stored by setting the magnetization states of individual magnetic domains as either "up" or "down." The conventional way to record a magnetic bit is to reverse the magnetization by applying an external magnetic field. Intuitively, one would expect that switching could be infinitely fast, limited only by the attainable strength and shortness of the magnetic field pulse. However, recent experiments on magnetization reversal, using uniquely short and strong magnetic field pulses generated by relativistic electrons from the Stanford Linear Accelerator, suggest that there is a speed limit on such a switching. It was shown that deterministic magnetization reversal does not take place if the magnetic field pulse is shorter than 2 ps [33].

The first experimental studies of laser-induced demagnetization in ferromagnetic materials were performed on Ni thin film by Agranat *et al* in 1984 [34]. They found that the sample was not successfully demagnetized when pumped by a light pulse of duration 5-20 ps, while a demagnetization was observed by laser pulses with a duration of 40 ns. Consequently, the authors claimed that the demagnetization and spin relaxation time took place at nanosecond timescale. At the beginning of the 1990s, Vaterlaus *et al* estimated the spin-lattice relaxation time in Gd films to be 100±80 ps by using a time resolved spin-polarized photoemission technique, with a 10 ns pump pulse and a 30 ps probe pulse [35, 36]. Normally, the available laser source at that time was with a pulse width between 60 ps to 10 ns, which was about the same duration or even longer than the time scale of interest. To study the intrinsic timescales and get a better understanding of the ultrafast process, ultra-short light pulses were needed.

In 1996, the discovery of ultrafast demagnetization of a Ni thin film by a 60 fs optical laser pulse triggered the new and booming field of ultrafast laser manipulation of magnetization [28]. Beaurepaire *et al* demonstrated a truly remarkable observation. A Ni film exposed to an intense 60 fs laser pulse becomes demagnetized in less than one picosecond. Using the magneto-optical Kerr effect as a probe beam, an ultrafast decrease could be observed in the magnetization, followed by a slower recovery (see Figure 7). Meanwhile, from the time dependence of hysteresis loops (not shown here, see Figure 1(b) [28]), they deduced that the remnant magnetization undergoes a drastic

decrease within 2.3 ps after laser pulse excitation. By way of contrast, the electron thermalisation time was about 260 fs, with estimates based on transient reflectivity.

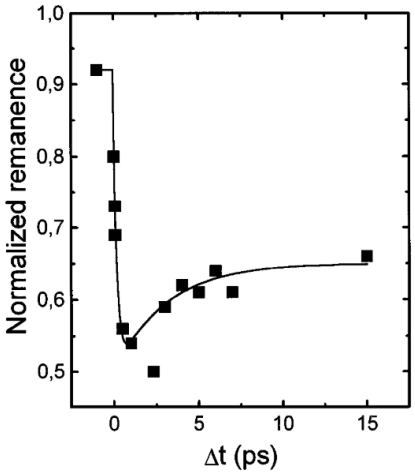

Figure 7. Transient remnant longitudinal MOKE signal of a Ni (20 nm)/MgF_2(100 nm) film for 7 mJ/cm^2 pump fluence. The line is a guide to the eye [28].

Since then, in order to understand the physics of ultrafast optical manipulation of magnetism, a systematic study started. In 2008, Carpene *et al* carried out pump-probe experiments in Fe thin films [37]. In their experiments the reflectivity response was observed to have around 150 fs delay after the magnetization response. This even-faster demagnetization, taking place on a time scale less than 100 fs, was attributed to the electron-magnon interaction with a time constant of 50 to 75 fs. The observed dynamic was much faster than the spin-lattice relaxation time, which is generally between 10 to 100 ps. Clearly, the excitation by a femtosecond laser pulse puts a magnetic system into a highly nonequilibrium state. Consequently, conventional macrospin approximation and thermodynamics are no longer valid to describe such an observation. In the sub-picosecond time domain, typical times are comparable to or even shorter than the characteristic time of spin-orbit interaction (10^{-12}–10^{-11} s), and the magnetic anisotropy becomes a time-dependent. Although the spin-orbit coupling is an important ingredient of the magnetic anisotropy mechanism, the latter is the result of a balance between different crystal field-split states. Therefore, the typical anisotropy energy is considerably lower than that of spin-orbit coupling, which is also translated into the corresponding longer response times. In such extremely short time scales, even the exchange interaction should be considered as time dependent. All these issues inevitably complicate a theoretical analysis of this problem.

In addition to the pursuit of the mechanism behind the ultrafast optical magnetism, a further topic which has been subject to heated debate is: what do time resolved pump-probe experiments really detect genuinely? Is it a simple optical excitation or a genuine magnetic excitation? To interrogate this, B. Koopmans *et al* conducted experiments on Cu/Ni/Cu wedges [38]. They concluded that, based on the difference between the Kerr ellipticity and rotation, the loss of magneto-optical contrast cannot be directly related to an instantaneous demagnetization. Conversely, in 2009, Zhang *et al* tried to solve this long-term dispute theoretically. By constructing a phase-sensitive polarization versus magnetization plot through a first-principles investigation of ferromagnetic nickel, a new paradigm for the magneto-Kerr effect was proposed. They claimed the optical response reflects the magnetic signal where the laser pulse is longer than the charge dephasing time [39]. Theo Rasing *et al* acknowledged the work of Zhang as no doubt a step toward a better understanding of the results of time-resolved magneto-optical experiments. However, the Zhang's research team did not consider pump-and-probe experiments at all. There is only one pulse in the model, which considers only the M_{xy} component of the magnetization tensor, while the relation between the calculated off-diagonal components of the magnetization tensor M_{xy} and the net magnetization of the sample M_{zz} remains unclear [29]. As the study involves numbers of simplifications and leaves many questions unanswered, Theo Rasing *et al* contended that the so called 'new paradigm' might be a slight overstatement.

Overall, the ultrafast laser-induced magnetization dynamic is a very complex process involving various components with different underlying physics. Additionally, experimental studies of ultrafast magnetization dynamics are often obstructed by artefacts, and thus the interpretations of the same data are regularly subject to intense debates. The exact physics of demagnetization in ferromagnetic metals remains an area of considerable debate. All of this makes the ultrafast laser-induced magnetization dynamic a worthwhile field for further research.

1.4.1 Laser-Induced Fast Magnetization Precession

Another important sub-field in laser-induced ultrafast magnetization dynamics is laser-induced magnetization precession. Nurmikko *et al* were the first to observe damped oscillation in the magnetization response after femtosecond laser excitation in ferromagnetic/antiferromagnetic exchange coupled bilayer films [40]. Later, in 2002, B. Koopmans *et al* successfully demonstrated the coherent magnetic precession by all-optical pump-probe experiments in Ni thin films [41, 42]. The frequency of coherent precession was discovered by the same method used in traditional ferromagnetic resonance (FMR), and thus this laser-induced magnetization precession is also known as all-optical FMR.

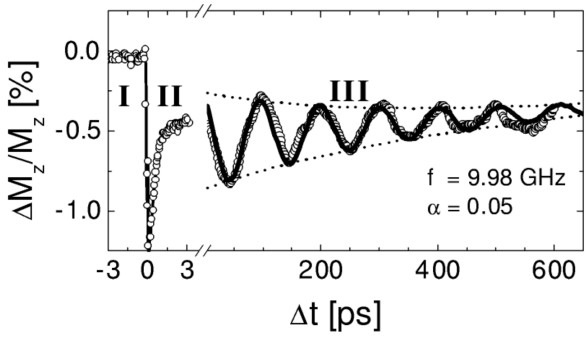

Figure 8. Typical measurement on a 7 nm Ni film, displaying the perpendicular component of the magnetization as a function of delay time [42].

When studying magnetization precession, an external field is applied away-from easy axis directions of the thin film, in order to create a noncollinear geometry of the anisotropy, applied, and demagnetization fields. Up to this point, the precession process has been well described. As we can see from Figure 9, before pump beam reaches to the sample surface ($\Delta t<0$), the magnetization **M** points to the initial equilibrium orientation $\theta_{Equilibrium}$, which is determined by the subtle balance between the external field H_0 and the anisotropy field H_A. At Figure 9 b) the pump beam reaches the sample surface and heats the sample, triggering a drastic decrease of the **M** ($\Delta t=0$). This is caused by a change in magnitude of the temperature-dependent magnetization. While the sample is subjected to such sudden heating by the pump beam, not only does the magnetization decrease but the anisotropy field also changes, due to thermal agitation (also known as quench). Thus, a new equilibrium orientation $\theta_{Equilibrium}$' is

formed, leading an initial precession of the **M**' around its new equilibrium orientation (Figure 9 b)). However, this precession is undetectable since the small effect on $\mathbf{M_z}$ is completely masked by the strong recovery variation magnitude of **M** ($0<\Delta t<10$ ps), and at this stage, the entire system is incoherent. After the heat has diffused into the sample, which usually takes about 10 ps for metallic films, the initial magnetization **M** and anisotropy field H_A recover, so that the initial equilibrium orientation is restored. However, the magnetization **M** is still not pointing to the equilibrium orientation due to its displacement at stage 3 (Figure 9 c)) and will continue to precess along the $\theta_{Equilibrium}$ for hundreds of picoseconds.

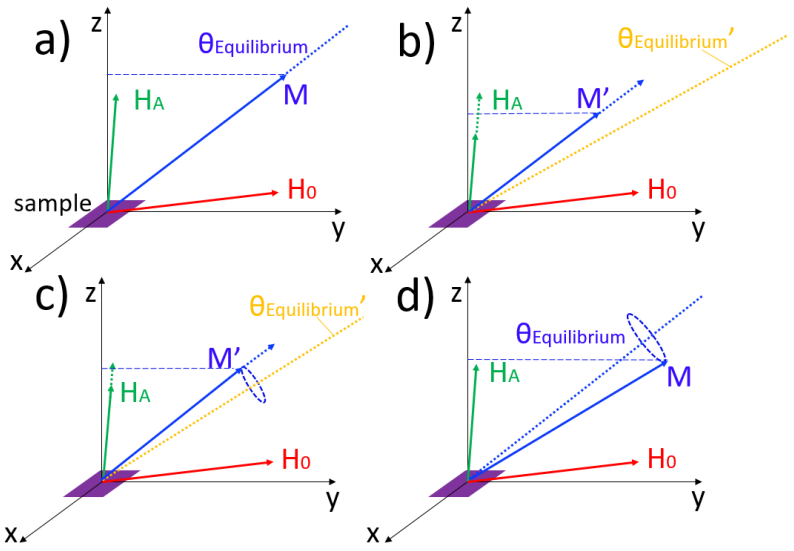

Figure 9. a)-d) correspond to different time regime occurring in the ultrafast laser-induced magnetization precession. Here, M, M', H_A and H_0 are magnetization, magnetization after quenching, anisotropy field and external field, respectively.

Coherent precession starts when the system is in a quasi-equilibrium state and the temperatures of all three subsystems are equal or very close. Compared with the mechanism of ultrafast demagnetization, laser-induced magnetization precession is not overly complicated. Although the electrons, spins, and lattices also interact with each other, the initial demagnetization is not a subject of particular interest. More importantly, laser-induced magnetization precession provides us a more sufficient and convenient approach to investigate coherent magnetization, and as such essential magnetic properties, such as damping constant and precessional frequency, can be extracted from the obtained Kerr signal.

1.4.2 All-Optical Switching

During the study of ultrafast magnetization dynamics, a number of unexpected and exhilarating phenomenon have been observed. In 2001, Hohlfeld *et al* demonstrated ultrafast magnetization on GdFeCo film. In their experiment an external magnetic field was directed antiparallel to the magnetization and a strength smaller than the coercive field was applied. Surprisingly, femtosecond laser excitation of the sample led to a total demagnetization and a slow recovery of the magnetic order with the magnetization reversed. Although the demagnetization occurred at the sub-picosecond time scale, the medium remained in the demagnetized state for a few picoseconds, and then exhibited slow recovery of the magnetization, which was completed in about 750 ps [43]. The mechanism behind the observation was explained by circularly polarized femtosecond laser pulses which act as equally short magnetic field pulses via the Inverse Faraday Effect (IFE). Consequently, this naturally leads to the question: can such optically induced field pulses be used to completely reverse the magnetization without any applied external field? In 2007, Stanciu *et al* achieved magnetization reversal by using a single femtosecond laser pulse without the help of any external magnetic field [44]. The experiments were performed by placing the GdFeCo under a Kerr microscope, so that domains with "up" and "down" magnetization could be observed as white or black regions (see Figure 10). Since then excitement has built over the potential applications of this, as it provides a low consumption way to control magnetism at speeds that are 2 or 3 orders of magnitude faster than traditional precessional switching. Naturally all-optical switching (AOS) has since been extensively studied, both theoretically and experimentally.

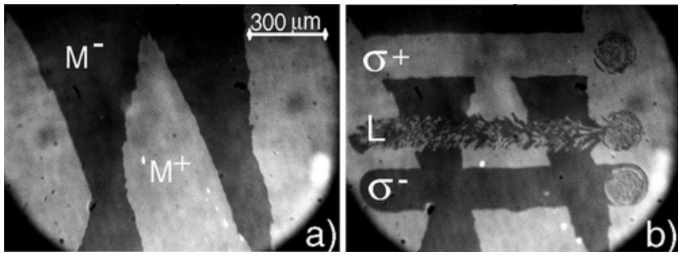

Figure 10. The effect of ultrashort polarized laser pulses on magnetic domains in $Gd_{22}Fe_{74.6}Co_{3.4}$, White and black areas correspond to up (M+) and down (M-) magnetic domains. σ+, σ-, L denote right-handed circularly, left-handed circularly and linearly polarized light, respectively, a) is before exposure to laser pulses and b) is after exposure to laser pulses[44].

In recent times, new interpretations have been proposed to explain the AOS phenomenon, since the traditional precessional reversing mechanism cannot be invoked, as a precessional reversing within such short time domain would require an enormous effective magnetic field up to 100 Tesla, as well as unrealistically strong damping. In 2011, by using element-resolved dynamics of the Fe and Gd magnetic moments measured via time-resolved XMCD [45], the previously investigated AOS phenomenon in GdFeCo has been shown due to a purely thermal effect. The laser-induced strong nonequilibrium state, followed by the creation of a transient ferromagnetic-like magnetization state, is the reason behind the magnetization reversal in GdFeCo. In other words, AOS observed in GdFeCo is thermal origin, which is irrelevant to or less affected by the laser helicity.

For a very long time, all-optical switching has been extensively studied in rare-earth (RM) based magnetic materials, such as GdFeCo [46, 47], TbCo [48, 49], TbFeCo [50-52]. However, recent experimental investigations have shown that all-optical switching is a more general phenomenon since it is not restricted to RE based ferrimagnetic films. There is some literature which demonstrates that all-optical switching can be observed in a variety of ferrimagnetic as well as ferromagnetic materials. S. Mangin *et al* investigated the RE based transition metal (TM) alloys, including Gd, Tb, Dy and Ho (RM), in order to study the influence of the RE variates and concentration in the AOS observation [53]. The net magnetization of the RE-TM alloys is given by the sum of the magnetization of the RE and TM sublattices. On the one hand, when the magnetization is pointing in the same direction as the magnetization of RE elements, the net magnetization will be named as RE dominant. On the other hand, when the magnetization is pointing along with the magnetization of TM elements, it will be TM dominant. The RE-TM alloys show a magnetic compensation temperature T_{comp} at which the two collinear sublattice magnetizations compensate, a net magnetization equal to zero. S. Mangin's work shows that AOS is observed for all of the studied ferrimagnetic alloys and is independent of the RE element, but only for a narrow window of RE concentrations, around 25%. Besides, the AOS is observed only when T_{comp} is near or above room temperature (RT), indicating that heating across T_{comp} favours the observation of AOS in RE-TM alloys. Furthermore, S. Mangin *et al* also investigated observations of AOS on RE-free

synthetic ferrimagnetic heterostructures (SFI). SFIs exhibit strong perpendicular magnetization anisotropy, consisting of two distinct and antiferromagnetically coupled magnetic sublattices. The two sublattices have different temperature dependences and show a T_{comp} near or above RT. Since they exhibit magnetic characteristics similar to the ones of RE-TM alloys and multilayers, AOS was successfully observed.

Since then studies of AOS have tended to focus in RE-TM ferrimagnetic magnetic materials, as well as RM-free SFI with two distinct and antiferromagnetically coupled sublattices. Another issue is proposed spontaneously, that is whether the AOS is specific to ferrimagnets or if it is a more general phenomenon which can also be observed in the ferromagnetic materials. In 2014, Lambert *et al* successfully demonstrated AOS in rare earth (RE) free ferromagnetic Co/Pt multilayers [54].

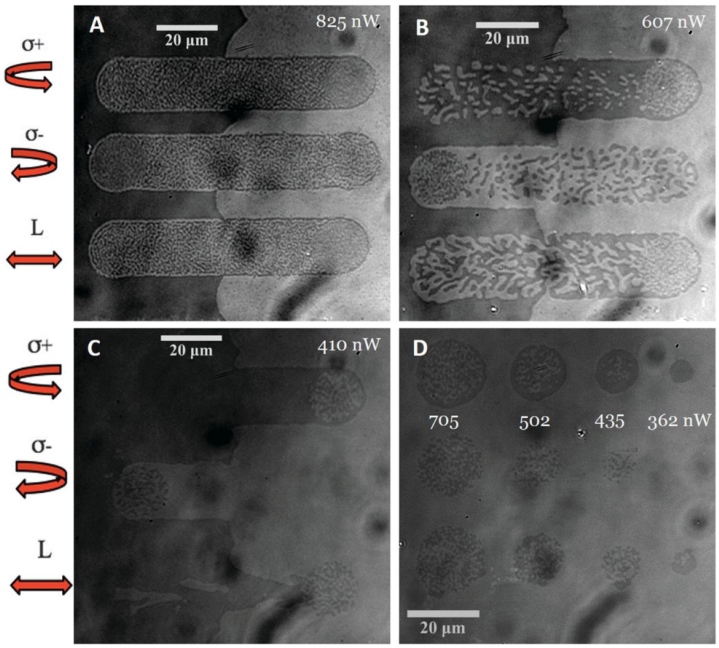

Figure 11. All-optical switching demonstrated on Co/Pt multilayer samples to various laser polarizations. A, B and C correspond to different pump power [54].

This is the first time AOS had ever been observed on ferromagnetic material. Lambert *et al* investigated the AOS observation in a large variate of ferromagnetic thin films with PMA included Co/Pt, Co/Pd, and Co/Ni multilayers [54]. The transition from AOS to thermal demagnetization (TD) in these ferromagnetic materials occurs by increasing the number of repeats, which was attributed to the demagnetising field increase. Despite the remarkable experiments they presented, there is, nevertheless, a

question mark hanging over their work, as we can see from Figure 11. From A to C, they gradually decreased the power of the pump laser pulse in order to study its influence on the final magnetization states after laser sweeping. According to the scale bars marked on the figures (white bar 20 μm), the three laser powers created the same size of laser scanned stripes. This is completely unrealistic during the actual experimental scenario. Besides, the results are also in contradiction with Figure 11 D, as Figure 11 D shown, when reducing the laser power from 705 nW to 362 nW, the diameter of laser spot is also shrinking.

Overall, these recent remarkable discoveries have triggered an intensive debate about the several mechanisms behind both ferrimagnetic and ferromagnetic AOS materials. After more than 10 years of experiments, as well as theoretical studies, the underlying physics of the AOS still remains a topic for debate, especially in terms of the roles of the helicity and the thermal effects of the pump laser. This is also one of the interests of this thesis.

1.5 Overview of the Thesis

The development of future storage devices requires fundamental physics research. As a result, the work presented in this thesis will mainly focus on: the domain walls motion in Permalloy nanowires; the light helicity influence on all optical switching in Co/Pt single layers, and finally; the magnetic precession dynamics in Co/Pt thin film. Lots of characterisation approaches and experimental techniques have been applied, including a focus magneto-optical Kerr microscope, spatial-resolved Kerr imaging, scanning electronic microscope (SEM), vibrating sample magnetometer (VSM) and pump-probe time-resolved MOKE (TR-MOKE).

In *Chapter 1*, I reviewed the evolution of the study of magnetism, and the development of applications based on the special properties in magnetism, especially those utilised in data storage devices. Moreover, a general review of the fields related to this thesis, including domain wall logic devices and laser induced magnetization dynamics has been presented.

In *Chapter 2*, I provide useful background information concerning the understanding of the experimental work presented in this thesis. A fundamental grounding of energy terms, domains theory, processional motion and interaction between photons and spins will be given. This knowledge is highly relevant to domain walls motion, magnetic precession motion and opto-magnetism.

In *Chapter 3*, it gives a detailed view of the experimental techniques used in this thesis. Magnetic characterisation techniques including SEM, VSM, MOKE, TR-MOKE, AFM will be addressed. Additionally, sample fabrication techniques and tools will be given.

From *Chapter 4* to *Chapter 6* contain my results. In the fourth chapter, nanowires with various notch geometries are investigated using a self-built wide field Kerr imaging system. Micromagnetic simulation is also induced to interpret the experimental results. The fifth chapter will study the magnetic precession dynamics in Co/Pt multilayer system, using time-resolved pump and probe techniques. The damping dependence with respect to layer repetition is presented. The sixth chapter mainly focuses on the influence of the laser helicity in all optical switching

experiment, which is still a hot topic in recent research activities, as the influence of the helicity and the thermal effect remains debatable. The AOS in Co/Pt is investigated, as is the mechanism behind the AOS. By varying the angle of the quarter-wave plate, the self-built Kerr imaging system is also induced to capture the magnetic domain states before and after laser scanning. As such, my results may provide an insightful support for explaining the AOS.

In the last chapter, *Chapter 7*, I give the general conclusions of my work. I will also make recommendations for future work. Complementary experiments that I am interested in will also be listed.

Chapter 2 Background Theory

2.1 Weiss Mean Field Theory

Pierre Weiss published his hypothesis on ferromagnetic materials; his theory gives a new understanding of ferromagnetic materials behaviour at the early stage of magnetism research. He speculated that magnetic moments μ in the ferromagnetic materials will interact with each other, and each one of them tries to align the other moments to its own direction. The theory explains that magnetic moments are in order, even in demagnetized state and these magnetic domains are consistently reorienting during magnetization process by external magnetic field. It predicted that the existence of tiny pieces of magnetic domains, and those magnetic domains will stay in the aligned order until the material reaches the Curie Temperature T_c, thus the ferromagnetic properties will transform to paramagnetic. The Weiss theory proposes that the mean (molecular) field H_m was proportional to the bulk magnetization M, so that [55]:

$$H_m = \alpha M \tag{2.1}$$

Here, α is the mean field constant. However, this is not applicable to the ferromagnets because of the variation of the magnetization from domain to domain, in this case, the term bulk magnetization M in Equation 2.2 is replaced by saturation magnetization M_S, so that:

$$H_m = \alpha M_s \tag{2.2}$$

The Weiss molecular field is the effect relating to the interatomic interactions, causing the neighbouring magnetic moments to try to align parallel to each other in order to reach the lowest energy state. This indicates that the interaction between magnetic moments causing the molecular field, which is an internal field that is strong enough to magnetize the material even in the absence of an external magnetic field. Thus, the effective magnetic field acting within a magnetic domain is given by:

$$H_{eff} = H_{external} + H_m \tag{2.3}$$

According to the Weiss theory, the calculated value of molecular field in iron to be of the order 10^3 T, which is far more than any manufactured field [55]. Moreover, the alignment of the magnetic moments or spontaneous magnetization can only occur when ferromagnetic materials are below their Curie temperature. Above the Curie temperature there will be a change in the susceptibility as the material becomes paramagnetic, therefore, giving the equation the Curie-Weiss law [55]:

$$\chi = \frac{M}{H} = \frac{C}{T - \theta} \tag{2.4}$$

Here, χ is the magnetic susceptibility of the material, which is the ratio of magnetization over magnetic field, C is the curie constant, T is the absolute temperature and θ is the Curie-Weiss constant, which is directly related to the molecular field. When higher than the Curie temperature, a ferromagnetic material becomes paramagnetic, and its susceptibility then follows the Curie-Weiss law, where the value of θ is approximately equal to T_C.

Even though Weiss theory seems to be inapplicable in modern magnetism, it is logical in describing the approximation of a coupling force between spin and can be used to describe basic understanding of ferromagnetism.

2.2 Energies in the magnetic materials

It is very important to study the magnetic system from the energetic point of view. The energies in the magnetic system will be induced to explain the formation of the magnetic domains and magnetic precession motion in the following sections of the thesis. In this section, I will start from four most important energies: exchange energy, magnetostatic energy, anisotropy energy and Zeeman energy, respectively.

2.2.1 Exchange Interaction

Weiss theory was a pioneer in explaining the spontaneous magnetization in ferromagnetic materials, it successfully predicted that the existence of magnetic domains in ferromagnetic materials. However, the theory did not explain the origin of those tiny pieces of magnetic domains.

Therefore, Heisenberg brought a new theory from quantum mechanical perspective to describe the domains [56]. He explained that the origins of these domains are the result of exchange interactions between magnetic moments in the ferromagnetic materials. Arising from the Pauli exclusion principle (two identical particles cannot occupy the same quantum states in a system), when the two particles with spin angular moment S_i and S_j, the exchange interaction of the two adjacent spins can be written as:

$$E_{exc} = -2J_{ex}S_i \cdot S_j \tag{2.5}$$

Here, in the expression, J_{ex} refers to the exchange integral, based on the sign of the exchange integral we can classify materials as ferromagnetic, antiferromagnetic and ferrimagnetic. When $J_{ex}>0$, the exchange energy is minimized when two adjacent spins are parallel (↑↑), so that the material is ferromagnetic, and when $J_{ex}<0$, the exchange energy is minimized when two adjacent spins are antiparallel (↑↓), if there is no net magnetization, then the material is characterized as antiferromagnetic, and if there is net magnetization but a reduced one as compared to ferromagnetic case, then the material is characterized as ferrimagnetic. Figure 12 is the Bethe-Slater curve, it gives the variation of exchange integral versus the ***a/r*** ratio the transition metals, as ***a*** is the radius of the atom and ***r*** is the radius of the 3d shell.

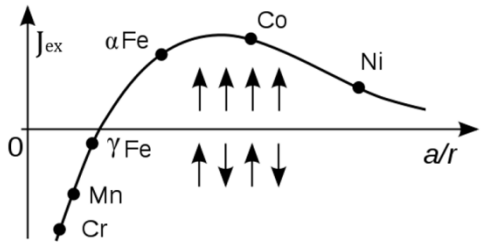

Figure 12. Bethe-Slater curve, the arrows indicates the direction of the spins [57].

Exchange interaction depends mainly on interatomic distance and it decreases rapidly with distance increases. This indicates that the summation of the total exchange interaction is limited to the nearest neighbour pairs only. The total exchange interaction can be written as:

$$E_{exc} = -2\sum_{i,j} J_{ex} S_i \cdot S_j \tag{2.6}$$

According to the Weiss mean field theory mentioned earlier, ferromagnetic is caused by a powerful molecular field which aligns the magnetic moments. But with the developing of the theory, Heisenberg precisely explains why the ferromagnetic moments tend to align parallel to each other, so it would be better to describe that the exchange forces leading the spins to be parallel.

2.2.2 Magnetostatic Energy

Magnetostatic energy originates from the dipole interaction of the magnetized material; it is also known as stray field energy, or demagnetization energy. The energy required to assemble the atomic dipoles in the magnetized sample so that it can be treated as a macroscopic magnetic dipole. When aligning the dipole magnets head to tail, the magnetic system will be in low energy configuration, which is much preferred than aligning them parallel to each other, the high energy configuration.

The field inside the magnetic material becomes equal to the applied field minus the field generated by magnetization inside the sample; this is called the demagnetization field. In general, the demagnetization field is originated from the poles at the sample surface opposing the magnetizing field. In such cases, the

demagnetization field is also known as the dipole field. The internal field in the magnetic material can be treated as:

$$H_{in} = H_{app} + H_{deg} \tag{2.7}$$

Here, the $\boldsymbol{H}_{in}$ is the field inside the magnetic material, $\boldsymbol{H}_{app}$ is the applied magnetic field and $\boldsymbol{H}_{deg}$ is the demagnetization field. The reason why it is called the demagnetizing field is because it acts in the opposite direction to the magnetization which produced it (see Figure 13).

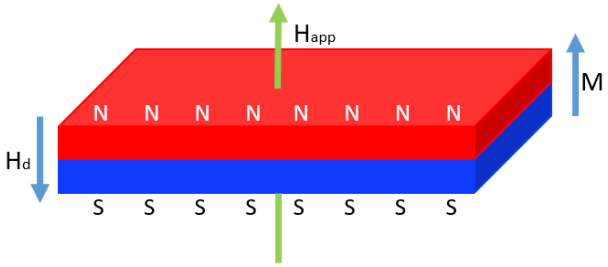

Figure 13. Schematic diagram of surface poles induced by the applied field and the demagnetization field due to the distribution of the surface poles.

However, the assumption that the magnetization is always normal to the sample surface is not valid when magnetization orientation is given relative to the sample axis a more general expression of the demagnetization field is given as:

$$H_d = -M \cdot n \tag{2.8}$$

Here $\boldsymbol{n}$ is the surface normal, for the sample with any shapes, the demagnetization field is thus expressed as:

$$H_d = -N_d M \tag{2.9}$$

The constant N_d is the demagnetization factor, it can be measured or estimated for most shapes of sample, for magnetic thin films, $N_d = 1$. Therefore, the magnetostatic energy can be evaluated as:

$$E_{static} = -\frac{\mu_0}{2} M \cdot H \tag{2.10}$$

Here, $\boldsymbol{\mu_0}$ is the permeability of free space, the factor of 1⁄2 is introduced to prevent from counting the interaction twice, because dipole pair interactions should not be

counted repeatedly. In short range distance, comparing with the powerful exchange interaction, the interaction of dipoles is much weaker. But in long distance, the dipoles interaction is dominant. Therefore, dipoles interaction is very important in describing the properties of magnetic moments over long distance, which is closely related to the formation of magnetic domains.

2.2.3 Anisotropy Energy

The magnetic properties of a magnetic material usually have a dependence of the direction of the magnetization with respect to the structural axis, this is known as magnetic anisotropy. The anisotropy of the magnetic material can be easily deducted from the hysteresis loops measured along various directions of the sample. There are several types of magnetic anisotropy, all of which can contribute to the free magnetic energy, these are shape anisotropy, magnetocrystalline anisotropy, magnetoelastic anisotropy, stress anisotropy, exchange anisotropy, etc. For the relevance of this thesis, the attention will be focused on shape anisotropy and magnetocrystalline anisotropy in the following subsections.

2.2.3.1 Shape Anisotropy

Magnetic shape anisotropy originates from the demagnetization field (introduced in 2.2.2). The demagnetization field of a single domain particle is given by Equation 2.9, the equation indicates that the demagnetization field of a single domain particle is proportional to the sample magnetization M.

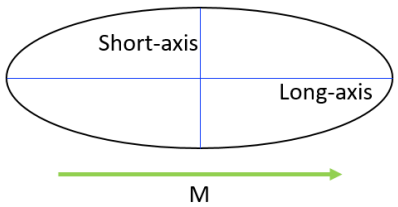

Figure 14. A single domain particle with long axis and short axis.

As we can see from Figure 14, considering a small single domain particle with an elliptical shape, due to the long range dipole interaction, the shape anisotropy energy density can be derived from the magnetostatic energy related to the demagnetization field produced by the magnetic dipoles on the sample surface which gives:

$$E_{Shape} = \frac{1}{2}\left(N_{long}cos^2\theta - N_{short}sin^2\theta\right)M^2 \qquad (2.11)$$

Here, N_{long} and N_{short} are the demagnetization factors of long-axis and short-axis of the sample, respectively. θ is the angle between the easy axis and the magnetization. If the sample is spherical, thus, the contribution of the shape anisotropy is zero.

However, shape anisotropy plays a more important role in nanostructures, especially in polycrystalline systems, in which the systems only have small magnetocrystalline anisotropy. Shape anisotropy primarily influences the magnetic states, because in such case, it is much stronger than the intrinsic anisotropies. In the experimental chapter-4 of this thesis, the Permalloy nanowires are dominated by the shape anisotropy, the easy axis is along the long axis of the nanowires due to the shape anisotropy effect for energy minimization. In addition, the saturation magnetic field is higher along the short axis than saturation magnetic field along the easy axis due to a greater magnetostatic energy for the short axis.

2.2.3.2 Magnetocrystalline Anisotropy

When we observe the magnetization curves by applying an external field along different directions, we may find that a magnetic material exhibits different properties depending on which direction it has been magnetized. This phenomenon indicates that different crystalline directions are not magnetically equivalent. The origin of magnetocrystalline anisotropy is from the coupling between the magnetic moments and the lattice [55]. More precisely, the magnetocrystalline anisotropy is attributed to spin-orbit coupling (SOC) as well as the crystalline electric field. In atomic physics, the coupling between the electron spin and the electronic orbital shape is known as SOC, which gives a direct channel between the spin and the lattice as an electron orbits around the atomic nucleus with a given orbital angular momentum. However, if the

crystalline electric field that results from the chemical bonding of the orbitals on a given atom with their local environment is less symmetry, then the molecular orbitals or bonding electron charge distributions will be energetically preferred to certain orientations. Therefore, the anisotropic crystalline electric field drives the orbital moments in a certain orientation and consequently determines the orientation of the spins via SOC. Here, two main specific types of magnetocrystalline anisotropy will be presented. One is the uniaxial anisotropy (UME); the most common anisotropy effect is connected to the existence of a single easy axis. The anisotropy energy density is given by:

$$E_k = \sum_{n=0}^{\infty} K_n sin^{2n}\theta = K_0 + K_1 sin^2\theta + K_2 sin^4\theta + \cdots \qquad (2.12)$$

Here θ is angle between the magnetization direction and the easy axis, K_0, K_1, K_2…, are the anisotropy constants, which are strongly temperature dependent. K_0 is independent of the angle and usually can be ignored because the energy will vary only when the magnetization moves from one direction to another.

Another case is cubic anisotropy, taking a single crystal iron for example, as illustrated in Figure 15, when applying and increasing external magnetic fields along different crystalline axis, the distinct bifurcation appears in the magnetization curves.

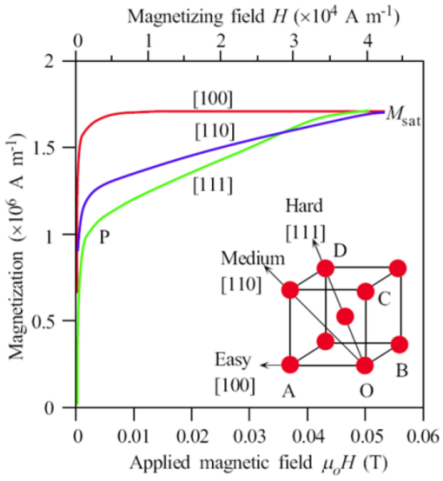

Figure 15. Magnetization curves of single crystal iron [58].

Due to the magnetocrystalline anisotropy, the saturation magnetization state will be reached to different fields along different magnetization directions, which can be used to define the easy and hard axis. As shown in Figure 15, for a typical body centred

cubic (BCC) structure like iron, <100> is the easy axis direction. The atom density is the lowest in <100>, along this direction the moments are saturated in a relatively low field. <111> is the hard direction, as we can see from the figure, the density of atom in the <111> is the highest, along this direction the magnetization vector reaches the saturation magnetization in a higher field. <110> is the intermediate direction. Comparing the red and green magnetization curves in the above figure, we can see that the saturation magnetization in <100> requires significantly lower field than in the <111> direction.

In a cubic crystal, the magnetocrystalline anisotropy energy is therefore usually written in terms of θ, the angle between the direction of magnetization and the axis of the cube:

$$E_k = K_1(\alpha_1^2\alpha_2^2+\alpha_2^2\alpha_3^2+\alpha_3^2\alpha_1^2) + K_2(\alpha_1^2\alpha_2^2\alpha_3^2) + \cdots \qquad (2.13)$$

where the α is the direction cosines of the magnetization along the coordinate axis. $\boldsymbol{K_1}$, $\boldsymbol{K_2}$, … are the anisotropy constant (unit: energy/volume). For example, the values of $\boldsymbol{K}$ of iron at 20°C are K_1=4.72 X 10^5 erg/cm^3, K_2=-0.075 X 10^5 erg/cm^3 [57], for iron as $\boldsymbol{K_1}$ >0 and ignoring the contribution of $\boldsymbol{K_2}$, $\boldsymbol{K_3}$, the anisotropy energy for <111> is higher than that for <100>, <010> and <001>, thus the <111> direction is the hard axis.

2.2.4 Zeeman Energy

Zeeman energy is also called external field energy, originates from the interactions between the magnetization and the external field, it is proportional to the negative of the cosine of the angle between the field and magnetization vector therefore the energy density is written as:

$$E_{Zee} = -\mu_0 H \cdot M_s \qquad (2.14)$$

Zeeman energy is the only energy term directly determined by the external field, the energy is at its minimum when all the magnetic moments in a sample are in alignment with the applied field.

2.3 Derivation of the Hysteresis Loop

The hysteresis loop shows the magnetization of a magnetic material in relation to the external magnetic field applied to it. As the material is magnetized, the domains within it will align with the external field at relatively low applied field due to the exchange interaction energy. A point will occur when the magnetization of the material does not increase as the field is increased. This indicates that all the domains in the ferromagnet have aligned with the external field, and this is known as the saturation magnetization. Then as the field is reduced back down to some of the magnetization will remain for the ferromagnetic sample, which is called the remanence. The magnetic hysteresis loop is formed by the magnetization reversal of the magnetic domains when an external magnetic is looped. It is the most common approach to directly reflect the magnetic properties of the material, which is extremely important in magnetism study.

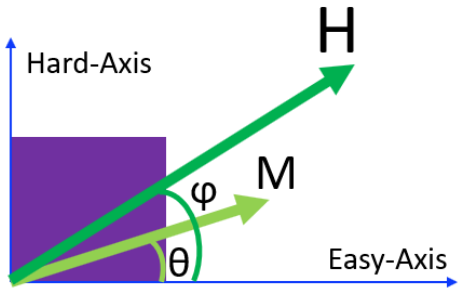

Figure 16, a single domain ferromagnet, $\boldsymbol{\theta}$ is the angle between $\boldsymbol{M}$ and easy axis; $\boldsymbol{\varphi}$ is the angle between applied field $\boldsymbol{H}$ and easy axis.

Let's start with an anisotropic ferromagnet with single easy axis, assume it is sufficiently small, so it consists of a single magnetic domain (all magnetic dipoles are aligned in the same direction in order to maximizing the total magnetization), the angle between the magnetization and the easy axis is θ, In the absence of an external field the energy of the ferromagnet is dominated by the anisotropy energy:

$$E_K = K_u sin^2\theta \tag{2.15}$$

When an external field is applied to the ferromagnet, in addition to the anisotropy energy we will also have the magnetostatics, which is given by:

$$E_{static} = HM_S cos(\varphi - \theta) \tag{2.16}$$

Then, the total energy of the system is given by the summation of Equation 2.15 and 2.16:

$$E_{total} = K_u sin^2\theta + HM_S cos(\varphi - \theta) \tag{2.17}$$

The equilibrium position of the single domain ferromagnet will be obtained by the partial derivative $\boldsymbol{E}_{total}$ with respect to θ is equal to zero:

$$\frac{dE_{total}}{d\theta} = 2K_u sin\theta cos\theta + HM_S \sin(\varphi - \theta) = 0 \tag{2.18}$$

The component of the magnetization in the field direction is given by:

$$\mathrm{M} = M_S \cos(\varphi - \theta) \tag{2.19}$$

Considering two particular cases, when φ=0, which mean the applied field is along the sample easy axis, thus θ=π, the entire system will be at its lowest energy according to Equation 2.18, and the magnetization is parallel with the external field. By solving the second partial derivative of $\boldsymbol{E}_{total}$ with respect to θ is large than zero, we can the energy will be minimized for all the magnetic field between: $-2K_u/M_s<H<2K_u/M_s$, therefore, the coercivity is given by:

$$H_c = 2\frac{K_u}{M_s} \tag{2.20}$$

We can tell from Equation 2.20 that materials with high M_s saturation magnetization would have low coercivity unless they have very high anisotropy.

Another case is when φ= π/2, which mean the applied field is along the sample hard axis, thus θ=π/2, the entire system will be at its lowest energy. By solving the second partial derivative of $\boldsymbol{E}_{total}$ with respect to θ is large than zero, only one condition can be satisfied, thus the anisotropy field is given by:

$$H_a = 2\frac{K_u}{M_s} \tag{2.21}$$

H_a is the anisotropy field, the field at which magnetization reaches saturation. For the field bellow the anisotropy field from the Equation 2.18, we also can obtain that

$2K_u\sin\theta+HM_s=0$, because the component of the magnetization is parallel to the applied external field, so $\sin\theta = -M/M_s$, substituting $-M/M_s$ into $2K_u \sin\theta + HM_s = 0$, we find:

$$M = M_s \frac{H}{H_a} \tag{2.22}$$

This indicates for the hard axis magnetization changes linearly with applied field until it reaches saturation.

Overall, the angle φ (direction of the applied field) will significantly affect the magnetization states, if the field is perfectly along the sample easy axis, the magnetization will flip over to the opposite direction when applied field reaches a critical value ($\boldsymbol{H_c}$), however, if there is a small angle between applied field and the sample easy axis, it will induce a torque on the magnetization leads to a rotation.

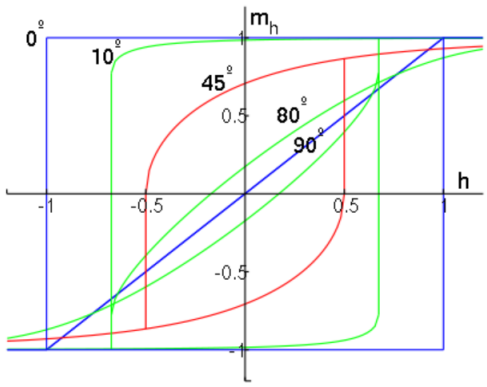

Figure 17. Hysteresis loops for different angles between the applied magnetic field and sample easy axis [59].

2.4 Magnetic Domains and Domain Walls

Figure 18 gives an illustration of magnetic domains. The magnetic domains are the regions of a magnetic material in which the magnetization is in the same direction. This means that the individual magnetic moments of the atoms are aligned with one another. At section 2.1, I mentioned that Weiss induced the existence of tiny magnetic domains in ferromagnetic materials to explain the demagnetization state. However, Weiss's mean field theory did not give the origin of the magnetic domains. After the brief introduction of the magnetic free energies exist in the material magnetic in the previous sections, the formation of the magnetic domains and domain walls thus can be explained from the energy point of view.

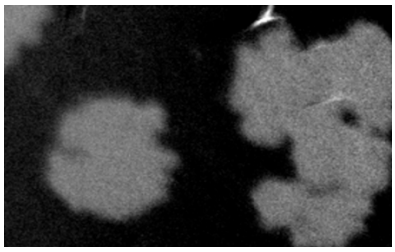

Figure 18. An illustration of magnetic domains in Co/Pt thin film obtained by Kerr imaging system, white and black contrast correspond to different domains.

2.4.1 Magnetic Domains

Magnetic dipoles interaction is very important in describing the properties of magnetic moments in long range distance, although the interaction of dipoles is much weaker compares with the exchange interaction that occurs in short range distance, but in long range distance, the dipoles interaction will be dominant.

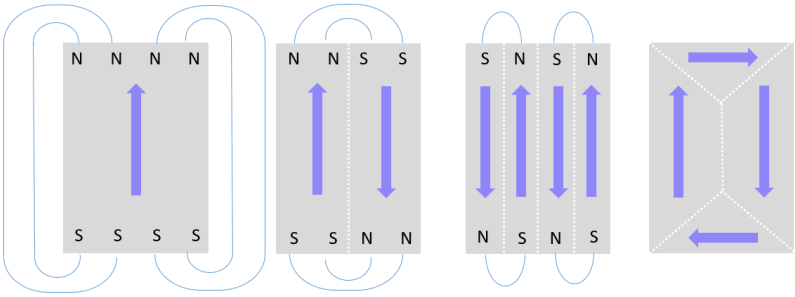

Figure 19. Magnetic domain formation due to reduction of the magnetostatic energy.

As one can see from Figure 19, a single domain magnetic material with magnetization throughout will create a large magnetic field extending into the space outside itself. This requires a lot of magnetostatic energy stored in the field. To reduce the magnetostatic energy, the material then divides into two domains with the magnetization in opposite directions, the field lines pass in opposite directions through each domain, reducing the field outside the material. To further reduce the energy, each of these domains can continue to form, resulting in more domains with magnetization points in alternating directions, thus even smaller amounts of field outside the material. Additional formation of the magnetic domains will cease when the energy for the formation of the additional domain wall is greater than the reduction in the magnetostatic energy. At this stage, each domain is magnetized to saturation in the direction of one of the easy axis, but the sum of the domain magnetization is zero (net magnetization is zero). The size of the magnetic domains also depends on another factor known as domain walls, which will be introduced in the following section.

2.4.2 Domain Walls

As introduced earlier, a larger single domain is unstable so that it divides into smaller domains in order to reduce the magnetostatic energy. Different domains are magnetized to saturation in the different directions of their easy axis. Due to the formation of magnetic domains is for energy minimization, therefore domain walls are formed along with magnetic domains spontaneously. Every time a region of magnetization divides into two domains, it creates a domain wall between the domains, where magnetic dipoles with magnetization pointing in different directions. In order to reduce the exchange energy, the system tends to align nearby dipoles point in the same direction. Conversely, the magnetostatic energy will prefer to align the dipoles in opposite direction, so that the system will be at its low energy state. Overall, domain wall configuration largely depends on the compromising between exchange energy and magnetostatic energy and magnetocrystalline energy.

Generally, the domain walls can be classified as two types (See Figure 20), one is Bloch walls, in these walls, the spins rotate normal to the plane of the wall. Another one is Néel wall, in Néel wall, the spins rotate within the plane of the wall [30].

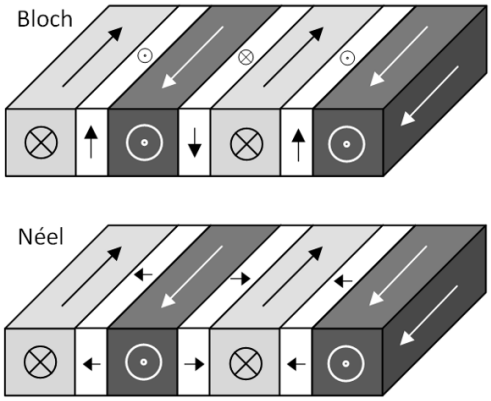

Figure 20. An illustration of two types of domain walls, Bloch wall and Néel wall [60].

2.4.2.1 Bloch Wall

As we can see from Figure 20 top, the magnetization of Bloch wall rotates along the axis perpendicular to the plane of the wall. Let us start from the simplest case, the Bloch with a total angular displacement of 180°, assuming the Bloch wall transition is over N lattice spacing wide, then the angle between the neighbouring spins will be θ=π/N, thus the corresponding variation of the exchange energy gives as:

$$\Delta E_{ex} = E_{ex} - E_{ex}^{\theta=0} \tag{2.23}$$

According to Equation 2.5, we can get:

$$\Delta E_{ex} = -2JS^2 cos\theta + 2JS^2 \approx 2JS^2 \frac{\theta^2}{2} = JS^2 \frac{\pi^2}{N^2} \tag{2.24}$$

Then the exchange energy variation per unit area of the 180° Bloch wall is given as:

$$\sigma_{ex} = \frac{\Delta E_{ex}^{total}}{a^2} = JS^2 \frac{\pi^2}{Na^2} \tag{2.25}$$

Here, ***J*** is the exchange integral, ***S*** is the spin angular momentum and ***a*** is the lattice constant. From this equation we can see that if ***N*** increases, the number of magnetic moments aligned offset the easy axis will also increase. Therefore, there will be an increase in the magnetocrystalline anisotropy energy per unit area, assuming that within the domains the spins are oriented along the easy axis and the neighbouring

domains are magnetized in opposite directions (θ=π), we can obtain the total anisotropy energy associated with the spins in the wall, replacing the sum by integral and taking into account that θ=π, we have:

$$E_a^{total} = \sum_{n=1}^{N} K_u \, sin^2\theta_n \approx \frac{1}{d\theta} K_u \int_0^{\pi} sin^2\theta d\theta = \frac{NK_u}{2} \tag{2.26}$$

Here, K_u is the magnetocrystalline anisotropy constant. Since anisotropy constant is per unit volume, the total anisotropy energy density per unit area of the Bloch wall is:

$$\sigma_a = \frac{NK_u}{2}\frac{a^3}{a^2} = \frac{NK_u a}{2} \tag{2.27}$$

Thus, the total energy per unit area of the Bloch wall will be the summation of both the contributions of the exchange energy and the magnetic anisotropy energy:

$$\sigma_{bloch} = \sigma_{ex} + \sigma_a = JS^2 \frac{\pi^2}{Na^2} + \frac{NK_u a}{2} \tag{2.28}$$

We can find the number of lattice spacing ***N*** that minimizes the energy density of the wall by the derivate $\boldsymbol{\sigma}_{bloch}$ respect to ***N***, thus ***N*** and domain wall with δ are given by:

$$N = \pi S \sqrt{\frac{2J}{K_u a^3}} \tag{2.29}$$

$$\delta = \mathrm{Na} = \pi S \sqrt{\frac{2J}{K_u a}} \tag{2.30}$$

We can see from the above equations that the domain wall width is proportional to the exchange energy, and inverse proportional to the magnetocrystalline energy.

2.4.2.2 Néel Wall

When a magnetic sample is ultra-thin, the thickness of the sample is comparable to the domain wall width. Therefore, in this case, the energy related to the demagnetization field on the sample surface at the Bloch wall becomes very large. The magnetostatic energy relative with the exchange and anisotropy energies will lead a transition of the Bloch wall rotation alignment. The unfavourable formation of Bloch wall in thin film will cause the walls transform to Néel wall [61].

The total energy per unit area of Néel wall can be calculated by including magnetostatic energy, the exchange energy and the magnetocrystalline energy to give:

$$\sigma_{\text{néel}} = 4\sqrt{A\left(K_u + \frac{\mu_0}{2}M_s^2\right)} \tag{2.31}$$

the exchange stiffness and the width of Néel wall can be written as:

$$\delta_{\text{néel}} = \pi\sqrt{\left(\frac{A}{K_u}\right) + \frac{2A}{\mu_0 M_s^2}} \tag{2.32}$$

Overall, the Néel wall is more favoured in the thin film due to it has a lower energy compares with the classic Bloch wall mode.

2.5 Precessional Motion

2.5.1 Single Spin Magnetization Dynamics

The traditional approach to switching of the magnetization is via magnetic field. Such switching process occurs with the precessional motion of magnetic moment, which can be described by the Landau-Lifshitz equation. To explain the onset of such a process, it is better to start from the motion of a single spin in an external magnetic field.

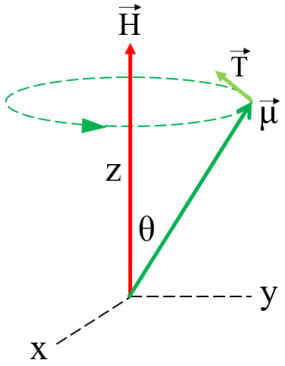

Figure 21. An isolated single spin in a magnetic field.

As depicted in Figure 21, when the single spin is placed in a magnetic field which is along the z-axis. θ is the angle between the applied magnetic field **H** and the magnetic moment **μ**. Thus, a torque **T** will act on the isolated spin perpendicular to the plane formed by the spin and the external magnetic field, the torque **T** is given by:

$$\boldsymbol{T} = \gamma \boldsymbol{L} \times \boldsymbol{H} = \boldsymbol{\mu} \times \boldsymbol{H} \tag{2.33}$$

where $\gamma = g\mu_B/\hbar$ is the gyromagnetic ratio, **L** is the angular momentum of the spin. Here $\boldsymbol{\mu} = \gamma \mathbf{L}$ represents the magnetic moment of the spin. A quantum mechanics description is used to express the action of this torque, which can also be derived classically as presented by J. Miltat [62]. The angular momentum **L** can be described by a spin vector as: $\mathbf{L} = \hbar\langle \mathbf{S} \rangle$. The temporal evolution of the mean value of spin can be described using the Schrödinger equation shown as [63]:

$$i\hbar \frac{d}{dt} \langle \boldsymbol{S} \rangle (t) = \langle [S, H(t)] \rangle \tag{2.34}$$

$$\boldsymbol{H}(t) = \gamma S \cdot H \tag{2.35}$$

(t) is the Hamiltonian of a signal spin under an applied external magnetic field. The three components of the Schrödinger equation, which make up the right part of Equation 2.34, can be expanded by using commutation rules as:

$$\begin{aligned}
[S_x, \boldsymbol{H}(t)] &= \gamma i\hbar\big(H_y(t)S_z - H_z(t)S_y\big) \\
\big[S_y, \boldsymbol{H}(t)\big] &= \gamma i\hbar(H_z(t)S_x - H_x(t)S_z) \\
[S_z, \boldsymbol{H}(t)] &= \gamma i\hbar\big(H_x(t)S_y - H_y(t)S_x\big)
\end{aligned} \tag{2.36}$$

According to above equations, the temporal evolution of spin can be rewritten as:

$$\frac{d}{dt}\langle \boldsymbol{S}\rangle(t) = \gamma\big(\langle \boldsymbol{S}\rangle(t) \times \boldsymbol{H}(t)\big) \tag{2.37}$$

The dynamics of the single spin in such a torque **T** are driven by:

$$\frac{d\boldsymbol{\mu}}{dt} = \gamma \boldsymbol{T} = \mu \times \boldsymbol{H} \tag{2.38}$$

Here $\boldsymbol{\mu}=\gamma\hbar\mathbf{S}$ represents the magnetic moment of the spin. Because the external field is $\mathbf{H}\cdot\mathbf{z}$, the equation above can be solved as:

$$\begin{aligned}
\mu_x(t) &= \mu cos\theta \sin(\omega t) \\
\mu_y(t) &= \mu sin\theta \cos(\omega t) \\
\mu_z(t) &= constant
\end{aligned}$$

These solutions indicate that the spin will rotate around the z-axis regardless of the angle θ. The angular frequency of the motion is linear function of the magnetic field $\omega = \gamma\mathbf{H}$, which is known as Larmor frequency, it is a no dissipation case and the spin cannot align along the direction of the external field. However, in the real scenario, the magnetization does not precess indefinitely and the rotation will damp out with the energy from the motion of magnetic moments, and gradually dissipate to the heat bath [64]. Instead, in order to explain and describe this dissipation, a phenomenological approach is used to create an equation with a damping constant representing all the possible intrinsic and extrinsic damping mechanisms for the magnetic materials.

2.5.2 The Landau-Lifshitz-Gilbert (LLG) Equation

During our experiments, measuring the dynamics of only one spin in the magnetic materials is impossible. If one assumes that a large number of spins behave almost the same as a single spin, it will allow a single macro-spin to be represented for all of the precessing spins in the magnetic materials. This assumption is a very important concept in the macro-spin model, which has been widely used by many researchers for analysing magnetization dynamics. Here, it is worth to mention that in this model, keeping the initial magnetization state the same and apply a uniform external magnetic field is necessary. However, in a practical experiment, the excited magnetization dynamics are not that uniform, because the disturbance and spin waves can be generated due to incoherent movement of spins. This is the major limit of the macro-spin model.

According to the assumption, the marco-spin can be written in the form as a magnetization vector $\boldsymbol{M}=\Sigma\boldsymbol{\mu}_i$, and the geometric relationship between the $\boldsymbol{M}$ and the spin operator $\langle \mathbf{S} \rangle$ is:

$$\boldsymbol{M} = \gamma\langle \boldsymbol{S} \rangle \tag{2.39}$$

Thus, the torque equation for a single spin can be extended to the macrospin scenario, and the Equation 2.37 in the previous section can be re-written in the form that governs the magnetization motion:

$$\frac{d\boldsymbol{M}}{dt} = \gamma(\boldsymbol{M}\times\boldsymbol{H}) \tag{2.40}$$

Equation 2.40 is known as the Landau-Lifshitz ($\boldsymbol{LL}$) equation [65], which describe the time evolution of the magnetization subjected to a magnetic field H. However, there is a limitation of the $\boldsymbol{LL}$ equation that once the magnetization is taken out of the equilibrium state, the $\boldsymbol{M}$ rotation around the magnetic field will last for an infinitely long time, which is not in accordance with actual experimental results. In the realistic scenario, the magnetic moment does relax to the new equilibrium direction via precession as a result of the energy minimization. Thus, a dissipative term is needed, by introducing an additional damping term that allows the precession process to cease after a certain time is necessary, so that the magnetization $\boldsymbol{M}$ can finally aligned with the magnetic field $\boldsymbol{H}$. The first person who attempt to add the dissipative term into the

LL equation is T. L. Gilbert [66], by using a thermodynamical approach, a dissipative term in ***LL*** equation is written as:

$$\frac{\alpha}{M_S}\left(\boldsymbol{M}\times\frac{d\boldsymbol{M}}{dt}\right) \tag{2.41}$$

Here α is the dimensionless Gilbert damping constant, M_s is the saturation magnetization, thus, the equation to phenomenologically describe the motion of the magnetization is given by the Landau-Lifshitz-Gilbert (LLG) equation:

$$\frac{d\boldsymbol{M}}{dt} = -\gamma(\boldsymbol{M}\times\boldsymbol{H}) + \frac{\alpha}{M_S}\left(\boldsymbol{M}\times\frac{d\boldsymbol{M}}{dt}\right) \tag{2.42}$$

The first term of the right-hand side describes the torque that leads to a precession, the second term describes dissipation energy and a convergence of the magnetic moment to align with the external field. With the damping term, the magnetization precession will eventually damp to the new equilibrium, therefore, the switching speed of magnetic materials is highly depended on the damping constant. Here, as mentioned earlier, γ is the gyromagnetic ratio, the minus sign used here is because $\gamma > 0$. The sign convention is important physically as it defines the direction of the torque applied to the magnetization and the precession direction. There is a sign convention, currently less used in the magnetization dynamics literature, but pervasive in history [67], where Equation 2.40 is used without the minus (-) sign, so we have to take $\gamma < 0$ to correctly describe the effect of the torque on the magnetization.

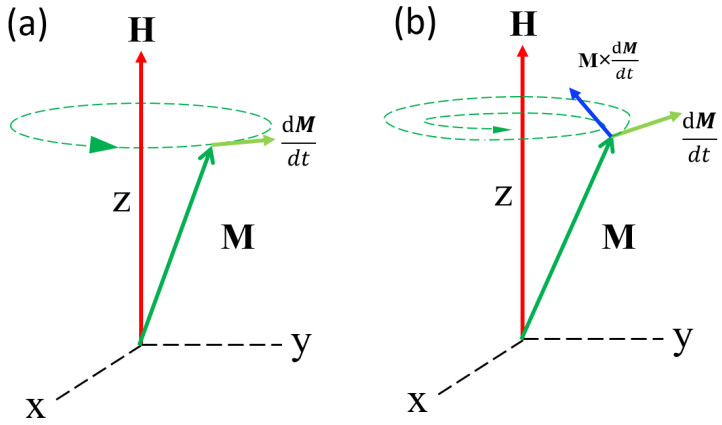

Figure 22. Schematic illustration of precessional motion. (a) is without damping term and (b) is with the Gilbert damping term.

2.5.3 Precession Frequency

As I discussed above, the magnetization precessional frequency cannot simply treated as the Larmor frequency, this case without a magnetic damping is only considered for simplicity. Firstly, there are various contributions of free magnetic energy. Secondly, besides the uniform precession mode (Kittel mode), the other non-uniform precession modes such as the standing spin waves, the moments precess coherently with a phase shift between neighbouring spin can also be observed in the experiments. However, the Kittel mode (wavenumber k=0) is the fundamental mode, especially when the homogeneous magnetization excitation is within the entire sample in presence of an applied field. The frequency dispersion relationship can be derived from the Landau-Lifshitz-Gilbert (LLG) equation in the spherical coordinate system.

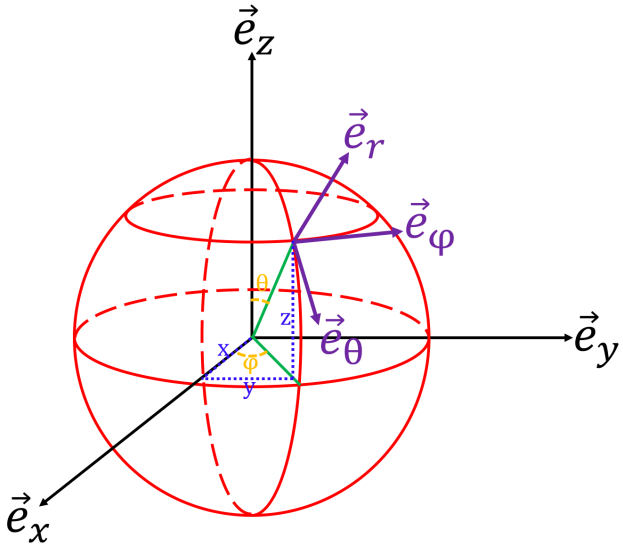

Figure 23. Schematic diagram of the spherical coordinate system, the magnetization vector is **M**.

Since the uniform precession frequency is not influenced by the damping term of the LLG equation (second term of the right-hand side of Equation 2.42), in order to derive the general expression of the frequency dependence on the applied field, we derive the ***LL*** equation from an applicable form firstly. The ***LL*** equation is given by:

$$\frac{d\boldsymbol{M}}{dt} = -\gamma\mu_0 \boldsymbol{M}\times\boldsymbol{H}_{eff} \tag{2.43}$$

In this case, the crystalline anisotropy energy, demagnetization energy and the Zeeman energy should be considered as the main contribution to the free magnetic energy *E*. In the single spin system, the effective field is attributed to the external field. However, here the effective field $\boldsymbol{H}_{eff}$ can be expressed by the partial derivative of the free magnetic energy *E* with respect to the magnetization m, which can be written as:

$$\boldsymbol{H}_{eff} = -\frac{1}{\mu_0 M_S}\frac{\partial E}{\partial m} \tag{2.44}$$

in the spherical coordinate system,

$$\boldsymbol{H}_{eff} = -\frac{1}{\mu_0}\left(\frac{\partial E}{\partial r}e_r + \frac{1}{M_s}\frac{\partial E}{\partial \theta}e_\theta + \frac{1}{M_s sin\theta}\frac{\partial E}{\partial \varphi}\right) \tag{2.45}$$

the left-hand side and right-hand side in the ***LL*** equation can be expressed as:

$$M_s\frac{d\theta}{dt}e_\theta + M_s sin\theta\frac{d\varphi}{dt}e_\varphi$$

$$\frac{1}{\mu_0 sin\theta}\frac{\partial E}{\partial \varphi}e_\theta - \frac{1}{\mu_0}\frac{\partial E}{\partial \theta}e_\varphi \tag{2.46}$$

The ***LL*** equation can be rewritten in the form of the azimuthal and polar angle of the magnetization as:

$$\frac{d\theta}{dt} = -\frac{\gamma}{M_s sin\theta}\frac{\partial E}{\partial \varphi}$$

$$\frac{d\varphi}{dt} = \frac{\gamma}{M_s sin\theta}\frac{\partial E}{\partial \theta} \tag{2.47}$$

The free magnetic energy *E* can be converted to a Taylor series for the small variations around the equilibrium position:

$$E = E_0 + \frac{1}{2}\left(E_{\theta\theta}\theta^2 + 2E_{\theta\varphi}\theta\varphi + E_{\varphi\varphi}\varphi^2\right) \tag{2.48}$$

Thus:

$$\frac{d\theta}{dt} = -\frac{\gamma}{M_s sin\theta}\left(E_{\theta\varphi}\theta + E_{\varphi\varphi}\varphi\right)$$

$$\frac{d\varphi}{dt} = \frac{\gamma}{M_s sin\theta}\left(E_{\theta\theta}\theta + E_{\theta\varphi}\varphi\right) \tag{2.49}$$

Considering the small harmonic oscillations around the equilibrium values, θ_0 and φ_0, the θ and φ follow the harmonic oscillations with the same angular frequency:

$$\theta - \theta_0 = \theta_A \mathbf{exp}\,(-i\omega t)$$

$$\varphi - \varphi_0 = \varphi_A \mathbf{exp}(-i\omega t) \tag{2.50}$$

Here, θ_A and φ_A are the amplitude of the precessions. Incorporate the above equations with Equation 2.49, a set of differential equation can be derived:

$$\left(\frac{\gamma E_{\theta\varphi}}{M_s sin\theta} - i\omega\right) + \frac{\gamma E_{\varphi\varphi}}{M_s sin\theta}\varphi = 0$$

$$\left(\frac{\gamma E_{\theta\varphi}}{M_s sin\theta} + i\omega\right) + \frac{\gamma E_{\theta\theta}}{M_s sin\theta}\theta = 0 \tag{2.51}$$

The non-trivial solution to a homogeneous system given by the above set of the differential equation only exists when ω is satisfied with:

$$\omega = \frac{\gamma}{M_s sin\theta}\sqrt{\frac{\partial^2 E}{\partial\theta^2}\cdot\frac{\partial^2 E}{\partial\varphi^2} - \left(\frac{\partial^2 E}{\partial\theta\partial\varphi}\right)^2} \tag{2.52}$$

The uniform precession frequency ω is derived in terms of the partial derivatives of the free magnetic energy E in the spherical coordinate system. According to the above equation, when given the free magnetic energy, the precession frequency thus can be determined in a specific geometry. As mentioned earlier, in the spherical coordinate system, with respect to the magnetization vector **M**, considering the simplest case, the free magnetic energy E can be expressed by the summation of the Zeeman energy, and the demagnetization energy:

$$\mathrm{E} = \frac{1}{2}\mu_0 M_s^2 cos^2\theta - \mu_0 M_s\left(\boldsymbol{H}_x sin\theta cos\varphi + \boldsymbol{H}_y sin\theta cos\varphi + \boldsymbol{H}_z cos\theta\right) \tag{2.53}$$

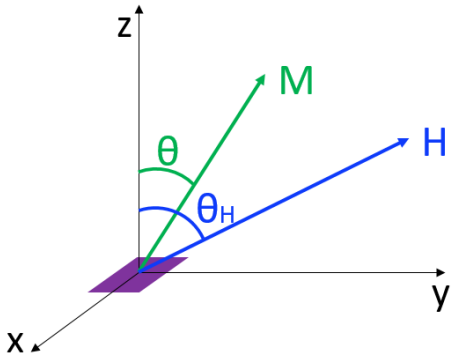

Figure 24. Illustration of the external field and the equilibrium orientation of the magnetization.

When an external field is applied along the angle θ_H with respect to normal of the surface, and the equilibrium orientation of the magnetization is along angle θ, considering the simplest case, the free magnetic energy E can be expressed as:

$$E = 2\pi M_S^2 cos^2\theta - M_S H[sin\theta_H sin\theta + cos(\theta_H - \theta)] \tag{2.54}$$

The equilibrium orientation of the magnetization can be treated at when the system is at its minimum energy state:

$$\frac{\partial E}{\partial \theta} = 0 \tag{2.55}$$

Combining with Equation 2.43, θ is then determined by solving the following equation numerically:

$$sin\,(2\theta) = \left(\frac{2H}{4\pi M_S}\right) sin(\theta - \theta_M) \tag{2.56}$$

By deducing the partial derivatives of the free magnetic energy in terms of a spherical coordinates of Equation 2.52 [68],

The uniform precession frequency is obtained:

$$\omega = \gamma\sqrt{H_1 \cdot H_2}$$
$$H_1 = Hcos(\theta_H - \theta) - 4\pi M_S cos^2\theta \tag{2.57}$$
$$H_2 = Hcos(\theta_H - \theta) - 4\pi M_S cos2\theta$$

Where γ is the gyromagnetic ratio, H_1 is the effective field along sample normal, and H_2 is the z-component of the magnetic flux density, M_S is the magnetization saturation. This results in what has come to be known as the Kittel formula for ferromagnetic resonance (FMR). However, it describes the frequency dispersion relationship in a uniform precession scenario, and the frequency is related to the material properties. This frequency dispersion relationship is an important theoretical foundation for the magnetic precessional dynamics in FMR or TR-MOKE measurements.

2.5.4 Damping Mechanism

The damping of magnetization precession in ferromagnetic materials is due to the energy transformation and dissipation from magnetic excitations to microscopic thermal motion and occurred between the lattice of the material system. As mentioned earlier, in a magnetic material system, there are lots of energy terms relating to the magnetization dynamics that define the magnetic free energy, including exchange energy, magnetostatic energy, Zeeman energy and anisotropy energy. These energy terms will finally determine the magnetization state and the effective field which control the magnetization dynamics [67]. The transformation and dissipation of those energy terms may be described as either direct or indirect, which is strongly depended on the pathway to the final state. The direct and indirect routes have also been referred to as fast and slow processes, respectively [69, 70]. There are several routes for the dissipation of energy in bulk or thin film ferromagnetic systems, all the routes including spin wave interactions, where the final stage is the magnon-phonon lattice interaction, in another word, the magnetization couples to lattice phonons, and this leads to damping of the magnetization precession motion. There are two types of broadly defined mechanisms, namely, intrinsic and extrinsic damping. The intrinsic damping is related to the fundamental properties of the magnetic material and is originated from the spin–orbit coupling (SOC). Kittel *et al* studied the relaxation processes in ferromagnetic substances and were the first to consider the spin-orbit-exchange-lattice interaction in the damping process as an intrinsic mechanism [71], the resulting coupling between the spin and the orbital angular momentum links the precession electronic magnetic moment to the lattice. As introduced in the previous

section, LLG equation can be used to describe the damping through the spin–orbit interaction and then scattering to the lattice, the intrinsic damping is represented as the damping term α in the LLG equation [72]. Another important intrinsic mechanism comes from the exchange interaction between electrons and magnetization; this is so called the breathing Femi surface model. Due to this process concerns valence electrons, so mechanism is only valid in metallic magnets. In ferromagnetic metals, the shape of a Fermi surface changes when the magnetization direction is changed, therefore, the Fermi surface becomes periodically varied due to the magnetization precession. Thus, a variation of the Fermi surface due to SOC is introduced by uniform precession, which is also known as a breathing Fermi surface [73]. With the precession of the magnetization, the spin orbit interaction becomes time dependent which changes the energy of the electronic state. Some occupied electron states jump above the Fermi level while some unoccupied states stay below the Fermi level. These electron-hole pairs exist for finite lifetime before relaxing through lattice scattering. In this mechanism, the amount of energy and angular momentum dissipated into lattice system depends on the new equilibrium of the system. The damping increases linearly with the electron lifetime [74].

On the other hand, the extrinsic damping is the non-Gilbert type relaxation. It is often attributed to two-magnon scattering (the interaction between the uniform mode and non-uniform modes), it includes the influence caused by inhomogeneities such as in the crystal structure, doping, interfacial defects and from spin wave propagation that excites additional magnon modes [75]. Ideally, in a perfect lattice without any defects or surface roughness, these contributions would not exist. The spin wave can be represented by a plane wave of $\boldsymbol{exp}\ (-i(\omega t - \boldsymbol{k}\cdot\boldsymbol{r}))$ at position $\boldsymbol{r}$ with the wavenumber k. When the wavenumber $\boldsymbol{k} = 0$, the plane wave will be time dependent only, and this corresponds to the uniform precession mode. Different combinations of the directions of the wavenumber and the magnetization determine the different types of spin waves, thus the dissipation of energy from the uniform mode magnon (k=0) and the non-uniform magnon modes (k≠0) combine to increase the overall damping. Figure 25 gives observation of uniform and non-uniform precession mode measured by the pump-probe TRMOKE, when the non-uniform mode exists (in this case, it is a perpendicular standing spin wave), the observed transient Kerr signal may look chaotic

at first. These can be separately recognised by fitting a combination of two damped sinusoid functions.

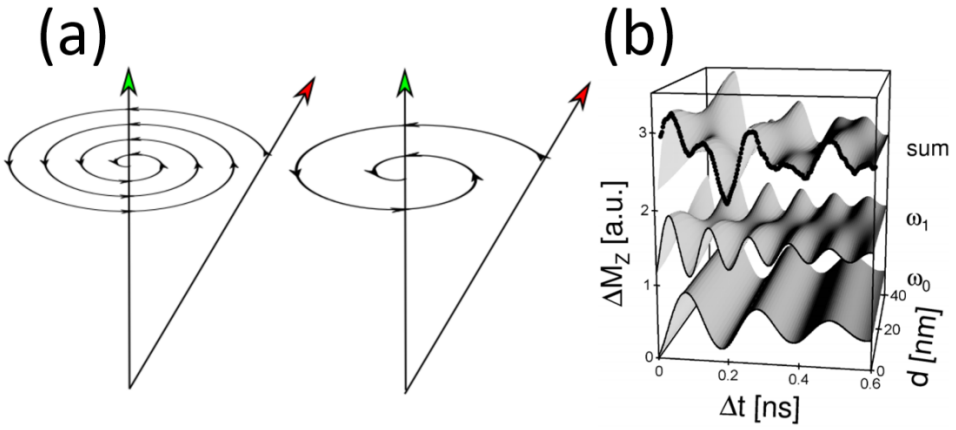

Figure 25. (a) Schematic of precessional damping with different rates of damping [67]. (b) Observation of coexistence of uniform and non-uniform precession mode [42].

2.6 Interaction Between Photons and Spins

Michael Faraday was the person who discovered that the polarization of light was rotated after being transmitted through glass in a direction parallel to an applied magnetic field. This is the first observation of a coupling between light and magnetism. In the succeeding years, the magneto-optical effect has been developed; it has been widely used to measure the magnetic properties. Moreover, since from the ultrafast demagnetization discovered in 1996 [28], to the all optical switching observed in GdFeCo [44], the reverse mechanism, namely how light affects magnetism, has brought a lot of attention in the recent research activities. The following sections will give a general review of the interaction between photons and spins, including Faraday effect, Kerr effect and inverse Faraday effect etc., which are highly related to my work.

2.6.1 Magneto-optical Faraday Effect

The magneto-optical Faraday effect was discovered in 1854 by Michael Faraday, it is a phenomenon of circular magnetic birefringence, where different refractive indices exist. A linearly polarized incident beam can be considered as composed by a left-handed circularly polarized (LCP) component and a right-handed circularly polarized (RCP) component, the LCP and RCP components have different phase velocities when passing through a magnetic material, resulting in phase differences between these two components that lead to a rotation of the polarization plane. Another case is if a magnetic material has magnetic circular dichroism (MCD), which refers to the different absorptions of LCP and RCP components, then the transmitted light will become an elliptical polarization.

The rotation of the polarization plane in the Faraday effect is proportional to the magnetic flux density and path length of light d in the material. Thus, the Faraday rotation of transmitted light can be described by:

$$\beta = \nu B d \tag{2.58}$$

Here, β is the rotation of the polarization plane, B is the magnetic flux density in the direction of propagation of the light, d is the path length of the light in the magnetic

medium, and ν is the Verdet constant of the material. The magneto-optical Faraday effect is widely used in dynamics or static magnetization measurements. However, as the Faraday effect measures the polarization change in transmitted light, therefore, the sample has to be transparent, which limits its application. In my projects, our samples are not transparent at all, so that Magneto-optical Kerr effect was used during all the measurements.

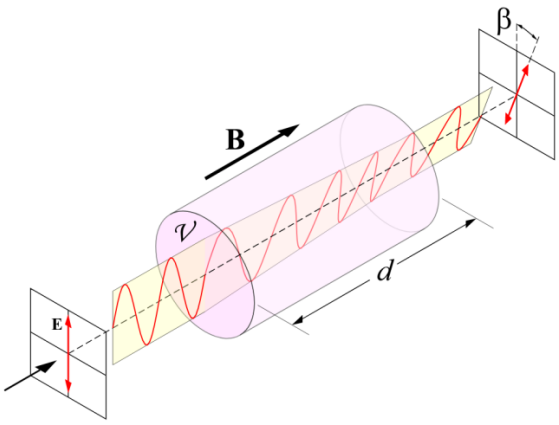

Figure 26. Schematic of magneto-optical Faraday effect [76].

2.6.2 Magneto-optical Kerr Effect

John Kerr found when linearly polarized light reflects from the magnetic sample surface, it will become elliptically polarized and its polarization axis is also rotated. This is known as the Kerr effect. When discussing the Kerr effect, the thickness that the light can penetrate in terms of interacting with magnetic materials must be considered, which is determined by the frequency of incident light and the electric properties of the material itself. The expression for skin depth δ is:

$$\delta = \sqrt{\frac{2\rho}{\omega\mu_r\mu_0}} \tag{2.59}$$

Here ρ is the resistivity of the material, ω is the angular frequency of the incident light, and μ_r and μ_0 are the relative magnetic permeability of the material and the permeability of free space, respectively. In the case of reflection from bulk material it is only the skin depth region, typically 10 nm to 20 nm in most thin films [77].

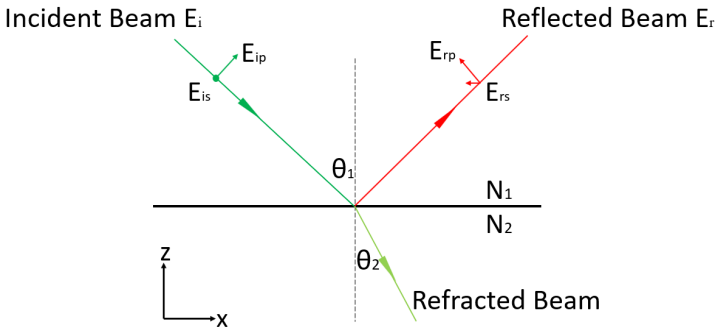

Figure 27. The geometry of the magneto-optical Kerr effect.

Figure 27 gives the schematic diagram of the geometry of the Kerr effect. When a beam of light, E_i, incident on the surface of a magnetic sample, it can be treated as a superposition of a p-polarized light and an s-polarized light. The p-polarized light has an electric field vector E_{ip}, which is parallel to the plane of incidence, while the s-polarized light has its electric field vector E_{is} perpendicular to the plane of incidence. E_{rp} and E_{rs} correspond to the p-polarized and s-polarized components of the reflected light, respectively. Thus, the reflection at the sample surface can be expressed by using the Fresnel reflection matrix R:

$$E_r = RE_i \tag{2.60}$$

$$\begin{pmatrix} E_{rs} \\ E_{rp} \end{pmatrix} = \begin{pmatrix} r_{ss} & r_{sp} \\ r_{ps} & r_{pp} \end{pmatrix} \begin{pmatrix} E_{is} \\ E_{ip} \end{pmatrix} \tag{2.61}$$

Here, r_{ss}, r_{sp}, r_{ps} and r_{pp} are the magneto-optical Kerr Effect reflection coefficients and the subscripts denote the scattering plane dependence of each element such that r_{ps} represents the ratio between the complex electric field amplitude of p-polarized reflected light and that of s-polarized incident light. Expression of the Fresnel reflection coefficients can be calculated by applying the reflection boundary condition [78]:

$$r_{ss} = \frac{\mu_2 N_1 \cos\theta_1 - \mu_1 N_2 \cos\theta_2}{\mu_2 N_1 \cos\theta_1 + \mu_1 N_2 \cos\theta_2} \tag{2.62}$$

$$r_{sp} = \frac{i\mu_1\mu_2 N_1 N_2 \cos\theta_1 \, Q(m_x \sin\theta_2 + m_z \cos\theta_2)}{(\mu_1 N_2 \cos\theta_1 + \mu_2 N_1 \cos\theta_2)(\mu_2 N_1 \cos\theta_1 + \mu_1 N_2 \cos\theta_2)\cos\theta_2} \tag{2.63}$$

$$r_{ps} = \frac{-i\mu_1\mu_2 N_1 N_2 \cos\theta_1 \, Q(m_x \sin\theta_2 - m_z \cos\theta_2)}{(\mu_1 N_2 \cos\theta_1 + \mu_2 N_1 \cos\theta_2)(\mu_2 N_1 \cos\theta_1 + \mu_1 N_2 \cos\theta_2)\cos\theta_2} \tag{2.64}$$

$$r_{pp} = \frac{\mu_2 N_1 \cos\theta_1 - \mu_2 N_1 \cos\theta_2}{\mu_1 N_2 \cos\theta_1 + \mu_2 N_1 \cos\theta_2} + \frac{2i\mu_1\mu_2 N_1 N_2 \cos\theta_1 \, Q m_y \sin\theta_2}{\mu_1 N_2 \cos\theta_1 + \mu_2 N_1 \cos\theta_2} \tag{2.65}$$

Here, μ_1 μ_2 are the permeabilities of media N_1 and N_2. N_1, N_2 are the complex indices of refraction. θ_1 is the incident angle and θ_2 is the refracted angle. Q is the complex magneto-optic constant, which is introduced in the permittivity tensor:

$$\varepsilon = \varepsilon_q \begin{bmatrix} 1 & -iQm_z & iQm_y \\ iQm_z & 1 & -iQm_x \\ -iQm_y & iQm_x & 1 \end{bmatrix} \tag{2.66}$$

Here, m_x, m_y and m_z are the magnetization components along the x, y, and z axis. While the total Kerr rotation θ_k and ellipticity η_k are superpositions of the two components the Kerr rotation and ellipticity for individual s-polarized and p-polarized components are the defined as:

$$\theta_{ks} = \mathrm{Re}\left(r_{ps}/r_{ss}\right) \tag{2.67}$$

$$\theta_{kp} = \mathrm{Re}\left(r_{sp}/r_{pp}\right) \tag{2.68}$$

$$\eta_{ks} = \mathrm{Im}(r_{ps}/r_{ss})\mathrm{Re}(r_{ps}/r_{ss}) \tag{2.69}$$

$$\eta_{kp} = \mathrm{Im}(r_{sp}/r_{pp})\mathrm{Re}(r_{sp}/r_{pp}) \tag{2.70}$$

As we can see from Equation 2.64 to 2.67 given a certain reflection boundary with a fixed incident angle, the Fresnel reflection coefficients are determined by the x-, y-, and z-components of the magnetization. This means that the Kerr effect is not only affected by the magnitude of the magnetization but also determined by its orientation.

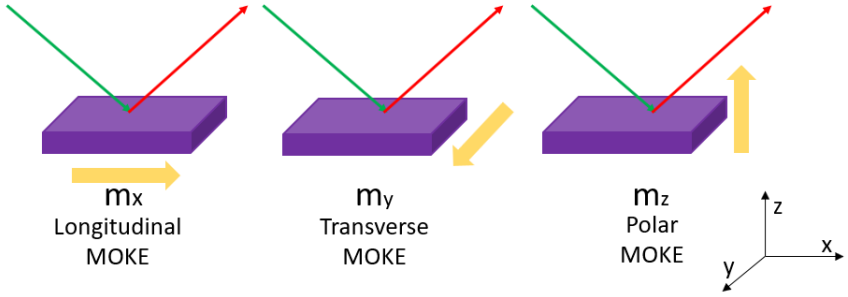

Figure 28. Different MOKE geometries, yellow arrows are the direction of magnetic field.

Figure 28 shows the schematic diagram of the three different MOKE geometries with respect to the different magnetization components. The contribution from z or perpendicular component of the magnetization is defined as the polar MOKE, in this configuration, both p and s polarized incident beams are sensitive to the z-component, thus resulting an m_z dependent elliptical polarization. Since the sensitivity decreases with an increasing incident angle θ_1, so that the normal incident will achieve the maximum polar MOKE signal. Similarly, the longitudinal MOKE is defined as the contribution of the x-component of magnetization; the longitudinal MOKE influences both p- and s-polarized incident lights. However, comparing to the polar MOKE, the longitudinal MOKE sensitivity is proportional to the incident angle θ_1. Finally, for the transverse MOKE geometry, only the y-component of magnetization contributes to the Kerr rotation, unlike polar and longitudinal MOKE, in the transverse geometry only the p-polarized incident light can sense the y-component of magnetization and give rise to Kerr signal.

The magneto-optic Kerr effect is a very useful and flexible tool to study magnetic properties. In order to apply it to measure magnetization dynamics, pump-probe time-

resolved techniques are combined with the magneto-optic Kerr effect, known as TRMOKE, both static MOKE and TRMOKE are involved in my research work.

2.6.3 Inverse Faraday Effect

The non-thermal approach via all optical switching within a sub-picosecond timescale is considered a potential alternative to the traditional precessional switching, which is hopefully enabling large data storage technologies with fast data transfer rates. The first demonstration of femtosecond opto-magnetic excitation of the magnetization dynamics was the laser induced antiferromagnetic resonance modes in $DyFeO_3$ by A. V. Kimel *et al* [79], they showed that circularly polarized laser pulses can be used to non-thermally excite and coherently control the spin dynamics in a $DyFeO_3$ sample by the way of name as inverse Faraday effect (IFE), two different processes of the Faraday rotation start on the scale of 60 ps after excitation after excitation with a pump pulse. The helicity of the light controls the photo-induced magnetization. In the following years, the IFE has drawn much attention.

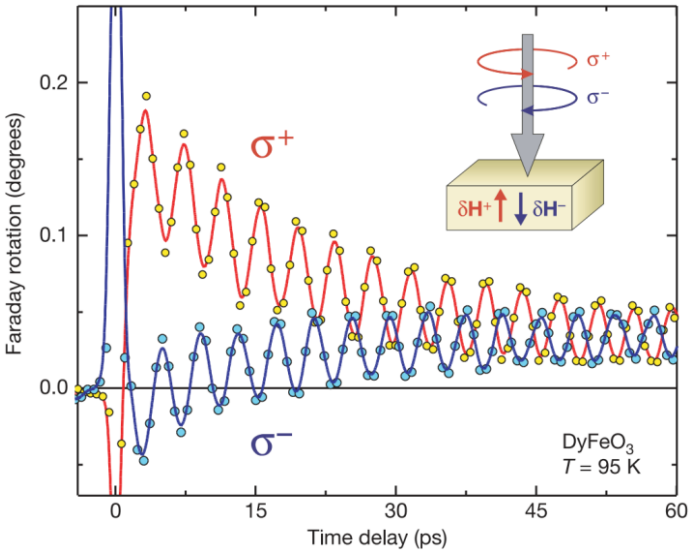

Figure 29. Magnetic excitations in DyFeO3. The circularly polarized pumps of two opposite laser helicities excite oscillations of opposite phase. Vectors δH^+ and δH^- represent the effective magnetic fields induced by right-handed and left-handed circularly polarized pumps, respectively [79].

The direct interaction between spins and photos can be derived from the energy point of view. In an non-absorbing, magnetically ordered medium with static magnetization **M**(0), and thermodynamic potential Φ, in a monochromatic electric field **E**(ω) of light wave includes the term [80]:

$$\Phi = \alpha_{ijk} E_i(\omega) E_j(\omega)^* M_k(0) \tag{2.71}$$

Here, α_{ijk} is the magneto-optic susceptibility, in the electric dipole approximation, the linear optical response of a medium to an electric light field **E**(ω) is defined by the optical polarization:

$$\boldsymbol{P}(\omega) = \frac{\partial \Phi}{\partial \boldsymbol{E}(\omega)^*} \tag{2.72}$$

From Equation 2.71, we can easily see that the optical polarization **P**(ω) should have a contribution $\mathbf{P}^{(m)}$ proportional to the magnetization:

$$\boldsymbol{P}_i^{(m)}(\omega) = \alpha_{ijk} E_j(\omega) M_k(0) \tag{2.73}$$

From the above equations, we can tell that when a linearly polarized light is transmitted through a magnetized medium, the polarization plane of the light gradually rotates over an angle $\theta_{Faraday}$ given by:

$$\theta_{Faraday} = \frac{\alpha_{ijk} M_k(0) \cdot \omega d}{cN} \tag{2.74}$$

Here, c is the speed of light in vacuum, N the refraction coefficient of the medium and d the propagation distance of the light in the medium. This is the magneto-optical Faraday effect we mentioned in section 2.6.1.

From Equation 2.71, one can find that an electric field of light at frequency ω will act on the magnetization as an effective magnetic field $\boldsymbol{H}_{eff}$ directed along the wave vector of the light **k**, thus:

$$H_k = -\frac{\partial \Phi}{\partial M_k} = \alpha_{ijk} E_i(\omega) E_j(\omega)^* \tag{2.75}$$

For an isotropic media, the magneto-optic susceptibility α_{ijk} is a fully antisymmetric tensor with a single independent element α, then Equation 2.75 can be rewritten as:

$$\boldsymbol{H}_{IFE} = \alpha[\boldsymbol{E}(\omega)\times\boldsymbol{E}(\omega)^{*}] \tag{2.76}$$

Here, $\mathbf{E}(\omega)^{*}$ is the complex conjugate of the light electric field $\mathbf{E}(\omega)$. As we can see from the above equation, the right- and left-handed circularly polarized (RCP and LCP) light should act as magnetic fields of opposite sign [81]. In addition to the magneto-optical Faraday effect mentioned earlier, where the polarization of light is affected by the magnetization **M**, the same susceptibility α also will determines the inverse opto-magnetic phenomenon. However, the inverse Faraday Effect (IFE) is only a phenomenological description, the origin of this opto-magnetic effect is still related to the spin-orbit interaction [29] [82].

2.6.4 Magnetic Circular Dichroism in AOS

Since the first demonstration of the AOS in GdFeCo alloy films [44], lots of mechanism have been proposed to explain the physics behind the observation. To the present, the AOS in GdFeCo thin film has been concluded due to a purely thermal effect [45], the AOS happens only due to the amount of energy absorbed by the magnetic system, which is independent of the wavelength or helicity of the laser pulses. However, there is strong dependence on helicity for laser pulses applied to the GdFeCo film for a narrow window of laser fluence, and this was quantitatively explained as a results of magnetic circular dichroism (MCD) [83].

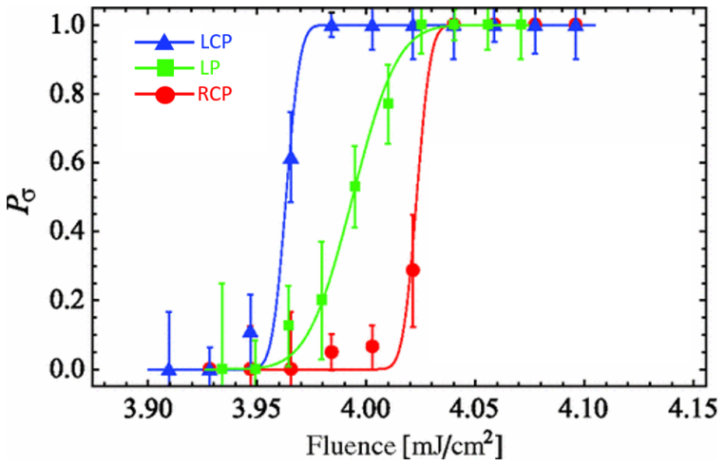

Figure 30. Switching probability Pσ as a function of the fluence at λ = 700 nm for three different polarizations [83].

In general, the MCD is the different absorption ratio of LCP, RCP laser pulses. As shown in Figure 30, the helicity dependent switching takes place only for laser fluence $F_{LCP} < F < F_{RCP}$, F_{LCP} and F_{RCP} denote for the switching threshold for left-handed (LCP σ-) and right-handed (RCP σ+) circularly polarized laser, respectively. The window of the helicity dependent all-optical switching (HDAOS) is thus defined as:

$$\Delta W = \frac{F_{RCP} - F_{LCP}}{\frac{1}{2}F_{RCP} + F_{LCP}} \tag{2.77}$$

In order to determine the microscopic origin of such window, the relative absorption of σ+ and σ- was calculated by:

$$\Delta\text{MCD} = \frac{A_{LCP} - A_{RCP}}{A_{LP}} \tag{2.78}$$

where A_{LCP}, A_{RCP} and A_{LP} denote the total absorption of light with σ-, σ+ and linearly polarization, respectively. Hence, it was shown that the window ΔW corresponds to MCD for wavelengths λ ranging from 500 nm to 800 nm. These findings show that magnetic circular dichroism (MCD) plays major role in the helicity-dependent reversal in GdFeCo.

2.6.5 Angular Momentum Transfer

It is well known that a circularly polarised laser pulse contains photons with angular momentum. On the other hand, the origin of magnetism is related to angular momentum. This similarity suggests that a circularly polarized laser pulse may interact with the spins of electrons via angular momentum (AM) transfer thus changing the magnetization.

In 1936, R. Beth made the first observation of the AM of light [84], a half-wave (λ/2) plate was suspended by a fine quartz fibre. A beam light is circularly polarized by a fixed quarter-wave (λ/4) plate. The beam light passed then through the λ/2 plate which transformed RCP into LCP and transferred $2\hbar$ of angular momentum for each photon to the birefringent plate. This measured torque is an agreement in sign and

magnitude with that predicted by both wave and quantum theories of light. Therefore, the ratio of the angular momentum of n photons in the beam is $J = \pm n\hbar$.

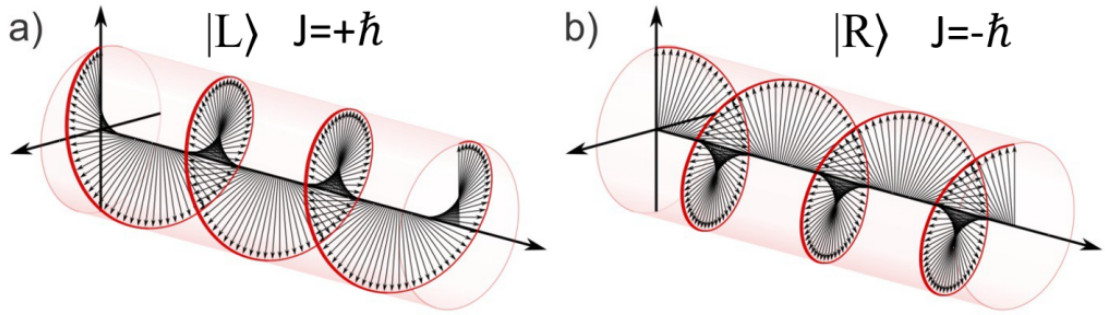

Figure 31. An illustration of LCP (a) and RCP (b), and the associated angular momentum [85].

2.7 Spin-Orbit Interaction

In quantum mechanical relation, the magnetic moment is described due to a circling electron, it is also called the orbital magnetic moment $\langle l_z \rangle$. By use of the Bohr magneton, one can write in general as:

$$\langle m_0^z \rangle = -\frac{\mu_B}{\hbar} \langle l_z \rangle \tag{2.79}$$

The orbital angular momentum is given by the expectation value of the angular momentum operator $\langle l_z \rangle$, the unit is ħ. In solids, the expectation value $\langle l_z \rangle$ is calculated with the appropriate band or ligand field wavefunctions. The electron itself has an intrinsic spin angular momentum with half-integer spin quantum number s= ħ/2 and an observable projection s_z=±ħ/2. The particles with half-integer angular momentum are called Fermions, while those particles with integer intrinsic spin are called Bosons. It is very important that the electron spin generates a full Bohr magneton with a spin of only ħ/2. The spin magnetic moment $\langle m_s \rangle$ can be written in a similar general expression as for the orbital moment:

$$\langle m_s^z \rangle = -2\frac{\mu_B}{\hbar} \langle s_z \rangle \tag{2.80}$$

The measured value of $\langle m_s \rangle$ is determined by the expectation value $\langle s_z \rangle$ along the quantization axis. Similar with the value of $\langle l_z \rangle$, the value of $\langle s_z \rangle$ is again calculated with the appropriate wavefunctions. In the real scenario, the spin generates a slightly larger moment, by a fraction of 10^{-3} μ_B. The small increase of the magnetic moment is called the anomalous magnetic moment, which is because of the fields of the moving electron on itself. The total magnetic moment is given by the sum of the spin and the orbital moments, and when neglecting the anomalous correction to the g-factor, the total magnetic moment is given by [86]:

$$\langle m_{total}^z \rangle = -\frac{\mu_B}{\hbar} (2\langle s_z \rangle + \langle l_z \rangle) \tag{2.81}$$

2.7.1 Orbital Angular Momentum Quenching

The spin orbit coupling (SOC) describes the interaction of the spin **S** with the orbital angular momentum **L** to a new total angular momentum **J**. It is about a factor of 10-100 smaller than the exchange interaction, the exchange interaction is the largest magnetic interaction and is the origin of the alignment of the spin system. In the 3d ions, the orbital angular momentum is broken up (quenched) by the crystal field, while the 4f shell is more like an inner than a valence shell. The compact radius and the relatively large atomic number of the rare-earth elements causes the spin-orbit coupling constant to be quite large.

The magnetic properties of the rare-earth metals can be understood in terms of the standard model, according to which the magnetic 4f electrons in the metal have the same angular-momentum quantum numbers as in the free ion. Those electrons are interacting with each other, however, with the surrounding electric field of the crystal, and with each other through an indirect exchange mediated by the conduction electrons. Most elements carry spin and orbital magnetic moments, the values are typically a few Bohr magnetons (μ_B). In the bulk materials, only a few elements like iron, cobalt, and nickel are ferromagnetically coupled. In these 3-d ferromagnets the orbital magnetic moment is quenched by the symmetry of the crystal lattice, which mixes wave functions with equal contributions of the magnetic quantum number to yield an orbital angular momentum of zero. In the materials with 3-d elements, spin orbital coupling (SOC) is usually much weaker than the electrostatic potential, so that the orbital moment quenching remains dominant. There is literature reported that the total magnetic moment is almost all contributed by the spin moment in these systems and amounts of the orbital magnetic moment decrease to only 5%–10% of its atomic value [87]. Conversely, in the rare earth (RE) elements, the SOC is much stronger than in the 3d transition metals (TM), moreover, they experience much less of the electrostatic potential around them, because the 4-f electrons the crystal field is much lower than the SOC. But in this case the total angular momentum J is a good quantum number, and the 4-f electrons are more shielded of their potentials without spherical symmetry, therefore, J is not conserved. This needs a group theory to be involved for making a quenching approach properly, so that the orbital moment quenching is somehow insignificant.

Although a quantitative treatment of the orbital magnetic moment is still under debate in theory, but it is accessible in experiments [88, 89] where spin and orbital magnetic moments can be determined by x-ray magnetic circular dichroism (XMCD), by applying the sum rule, we can study the quenching of the orbital momentum and its relation to the localized or itinerant nature of the total magnetic moment [90]. Lots of experiments shown that the orbital magnetic moments can be strongly enhanced over the bulk value by environments of reduced symmetry, but the relative enhancement of the spin moment is less observed [91-93]. Generally, the effects of orbital angular momentum quenching are when a lack of symmetry or other conditions, allows to consider that the orbital angular momentum fully quenched (L=0) or partially quenched. In such case the total angular momentum J=S, which is equal to the one of the electron spins. This simplifies the calculations when the electronic configuration enables to do it with respect to the crystal field. The angular momentum quenching only works when the crystal field is high, thus, the total angular momentum J has magnetic moment with eigenvalues $m_\ell+2m_s$, we label the states as $|\ell, s, m_\ell, m_s\rangle$ and allow us to calculate a Landé g-factor using only the total angular momentum J=S. Taking Fe with bcc as an example, one can take J=1 for obtaining one exchange energy around $8x10^{-3}$ eV [94].

2.8 Energy Band Theory for the Transition (TM) and the Rare-Earth (RE) Metals

The stoner mode relies on a simply density of states, it is assumed to have the shape of semicircle but with no structure. In the real scenario, the density of state (DOS) calculated for transition metals, Fe, Co, Ni, and nonmagnetic Cu with the same band structure code is shown in Figure 32. As we can see from Figure 32, the shapes of the DOS in Fe, Co and Ni are very similar, while Cu shows no exchange splitting. The exchange splitting defines as the relative shift of spin-up and spin-down bands is of the order of 1eV from Figure 32, if one uses the relative shift of the largest peak in the DOS we can get about 2.2 eV in Fe, 1.7 eV in Co and 0.6 eV in Ni, which are also in good agreement with the trend in the d shell spin moments calculated, which are about 2.2 μ_B, 1.7 μ_B and 0.7 μ_B for Fe, Co, Ni, respectively. The most important difference in the DOS graphs is the different positions of the Fermi Energy (dash line- E_F), it separates the occupied from the unoccupied states, accounting for the increasing number of d-electrons on going from Fe to Cu. Moreover, we can see from the DOS, the majority spin bands of Fe are not fully occupied, thus, Fe is called a weak ferromagnet. The majority spin bands of Co and Ni are fully occupied, which makes Co and Ni strong ferromagnets.

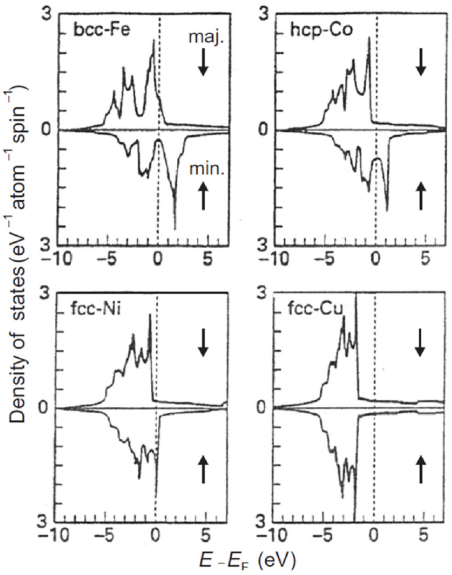

Figure 32. DOS of Fe, Co, Ni and Cu for the majority (arrow up) and minority spins (arrow down), respectively. The Fermi Energy (E_F) is set to zero [86].

The rare-earth (RE) is used to describe one of a set of seventeen elements in the periodic table, specifically the fifteen lanthanides, as well as scandium and yttrium. Sometimes a broader definition that includes actinides may be used, since the actinides share some mineralogical, chemical, and physical characteristics, especially the electron shell configuration. For the neutral atoms, their electronics structure consists of a Xe ($4f^N5d^16s^2$) atom core with a partially filled 4f shell and outer valence electrons in the 5d and 6 shells. The 4f shell is increasingly filled across the series from N=0 to 14, while the 5d and 6s shells remains relative similar. The light RE corresponds to a 4f shell which is less than half filled (e.g. Sm, Pr, Nd and Eu), which can lead to a ferromagnetic coupling with the TM sublattice. On the other hand, the heavy RE is above the half filling threshold (e.g. Gd, Tb, Dy, Ho and Tm), thus can lead to an antiferromagnetic coupling with the TM sublattice [95]. The RE element Gd (Z=64) is also one of the elementary ferromagnetic metal in the nature, the curie temperature is 289 K, which is just below the room temperature. The element Gd has the special property due to a half filled 4f shell with a configuration of [Xe] $4f^75d^16s6p$. The 4f shell contains the largest number of unpaired electrons, therefore, the magnetic moment of the RE metals dominated by the 4f electrons. However, the 4f electrons have strong localization and does not participate significantly in bonding [96]. Its ligand field splitting is small, which does not influence the orbital moment in the 4f shell, the total moment is contributed by spin and orbital moment. The curie temperature is below room temperature indicates a relative week exchange coupling between atoms. The coupling has two main contributions, one is indirect RKKY interaction between the 4f atomic moments, another is the direct overlap of the 4f and 5d electrons on a given atom. The overlap yields a strong direct exchange and polarizes the 5d electrons which assume generating a magnetic splitting and a magnetic moment. The total moment for Gd consists of $7\mu_B$ 4f and $0.6\mu_B$ 5d contribution [97].

2.9 Derivation of Gilbert Damping Constant α

The dimensionless Gilbert damping constant α is the key to compare the magnetic damping from different materials and experimental configurations in regard of strength and orientation of the external field. In time-resolved measurements, the signature of the Gilbert damping is directly linked with the exponential decay time τ. The relationship between the Gilbert damping parameter α and the exponential decay time τ can be derived from the LLG equation, the equation is linearized for a corresponding effective magnetic field H_{eff} for each of the precession modes. The coupled differential equations derived from linearization of the LLG equation can be simplified by considering only those magnetization components that contribute to the precession. Because the thin films the magnetization is mainly in-plane, so $M_{\mathrm{z}} \ll \sqrt{M_x^2 + M_y^2}$, the external magnetic field H is in the xz-plane. We assume that the magnetization is aligned along the x-direction and a very small amount is applied to trigger the magnetization precession, during the precession $M_{\mathrm{y}}, M_{\mathrm{z}} \ll M_{\mathrm{x}} \cong 1$. In this case, the LLG equation (Equation 2.42) can be re-written as three components [68]:

$$\dot{M}_{\mathrm{x}} = 0$$

$$\dot{M}_{\mathrm{y}} = -\gamma_0\left(M_{\mathrm{z}}H_{\mathrm{eff,x}} - M_{\mathrm{s}}H_{\mathrm{eff,z}}\right) - \alpha\dot{M}_{\mathrm{z}} \tag{2.82}$$

$$\dot{M}_{\mathrm{z}} = -\gamma_0\left(M_{\mathrm{s}}H_{\mathrm{eff,y}} - M_{\mathrm{y}}H_{\mathrm{eff,x}}\right) + \alpha\dot{M}_{\mathrm{y}}$$

where $H_{eff,i}$ is the i-component of the effective magnetic field H_{eff}, and the x-component of the magnetization, M_{x}, is treated as a constant of the saturation magnetization M_{s}.

As mentioned in section 2.5.3, the free magnetic energy of the ferromagnet in an applied external field is consists of the Zeeman energy, the demagnetization field energy and the crystalline, anisotropy term. The effective field can be derived from the free magnetic energy by means of the equation (section 2.5.3, Equation 2.44):

$$H_{\mathrm{eff}} = -\frac{1}{\mu_0 M_{\mathrm{s}}}\frac{\partial F}{\partial m} \tag{2.83}$$

where $m = (m_x,\ m_y,\ m_z)$, the magnetization unit vector, and the magnetization is equal to $M_x m_x + M_y m_y + M_s m_z$. Therefore, the expression for the free magnetic energy in Cartesian coordinates gives:

$$E = -\mu_0\left(H_x M_x + H_y M_y + H_z M_z\right) + \frac{1}{2}\mu_0 M_z^2 \tag{2.84}$$

Combining Equation 2.83 and Equation 2.84, the effective field can be derived:

$$H_{\text{eff}} = H_x m_x + H_y m_y + (H_z - M_z) m_z \tag{2.85}$$

Substituting the effective field into Equation 2.82, the motion for M_y and M_z can be derived as:

$$\dot{M}_y = \gamma_0 M_s H_z - \gamma_0 (H_x + M_s) M_z - \alpha \dot{M}_z \tag{2.86}$$

$$\dot{M}_z = \gamma_0 H_x M_y + \alpha \dot{M}_y \tag{2.87}$$

The coupled linear differential equations must be solved for continuous functions, derivatives of higher orders, and a solution for one of the variables. Due to the continuity of the precessing magnetization vector, the time derivative of the higher order derivatives of Equations 2.86 and 2.87 are calculated as

$$\ddot{M}_y = -\gamma_0 (H_x + M_s) \dot{M}_z - \alpha \ddot{M}_z \tag{2.88}$$

$$\ddot{M}_z = \gamma_0 H_x \dot{M}_y + \alpha \ddot{M}_y \tag{2.89}$$

Due to the end of the magnetization vector lies on a circle in the yz-plane, combining Equations 2.86 to 2.89, with only the equation of motion for the y-component considered, gives

$$(1 + \alpha^2)\ddot{M}_y + \alpha\gamma_0 (2H_x + M_s)\dot{M}_y + \gamma_0^2 (H_x + M_s) H_x M_y = 0 \tag{2.90}$$

The assumed solution is given by:

$$M_y = M_y^0 \exp(-i\omega t) e^{-t/\tau} \tag{2.91}$$

where ω is the angular frequency of the magnetization precession and τ is the exponential decay time. The imaginary part of the left-hand side of Equation 2.91 must to be zero, thus:

$$(\alpha^2 + 1)\frac{2i\omega}{\tau} - i\omega\alpha\gamma_0(2H_x + M_s) = 0 \tag{2.92}$$

From the quadratic Equation 2.92, the solution for the damping constant can thus be derived:

$$\alpha = \frac{1}{2}\left(\frac{\tau\gamma_0(2H_x + M_s)}{2} \pm \sqrt{\left(\frac{\tau\gamma_0(2H_x + M_s)}{2}\right)^2 - 4}\right) \tag{2.93}$$

As α would be much larger than 1 with solution with a plus sign, indicating an overdamped precession, which is not the observed case in most magnetic materials as well as in our experiments. Thus, the only solution is the one with the minus sign, the damping parameter can be determined by:

$$\alpha = \frac{1}{\tau\gamma_0(H_x + M_s/2)} \tag{2.94}$$

At the limit of high external fields, $H_x \gg M_s/2$, the precession frequency will be treated as the Larmor frequency $\omega = \gamma H$, in the limit of high external fields, the anisotropy contribution to the frequency dispersion can be neglected, therefore Gilbert damping parament α can be given by:

$$\alpha = \frac{1}{\tau\omega} \tag{2.95}$$

We can see from Equation 2.95 that the damping parameter is simply inversely dependent on the product of the exponential decay time and the precession frequency. Equation 2.95 is always applicable in high external conditions, although the derivation of the damping parameter must include the contribution of the anisotropy energy to the free magnetic energy. Thus, a higher enough external field is essential for the accuracy of the measurement of Gilbert damping constant.

Chapter 3 Experimental Techniques

Advances in the study and development of magnetic materials, as well as in recording technology, means that there are many methods available for measuring the magnetic properties of the samples, both statically and dynamically. For static measurements, the magnetic response of a sample to an applied external field can be measured through a number of techniques. These include using the Superconducting Quantum Interference Device (SQUID), Vibrating Sample Magnetometer (VSM) and Magneto-Optic Kerr Microscope (MOKE). For dynamic measurements, one of the most important techniques is the Time Resolved magneto-optical Kerr microscope (TR-MOKE). This is widely used to probe the ultrafast behaviour of magnetic properties within a very short time domain. During this Ph.D project, a wide range of the techniques listed above have been used to fabricate and characterise the magnetic properties of the samples. This chapter will present a detailed description of the various experimental techniques which are heavily related to this work, as well as some other techniques used in the pursuit of this Ph.D.

3.1 Wide-field MOKE Imaging

The creation of wide-field MOKE imaging was based on the commercial reflected light wide-field microscope [98]. The optics used are all strain free as this is mandatory for polarization microscopy. As can be seen from Figure 33, a royal-blue LED with peak wavelength around 455 nm is used as the illumination source, then a collector lens is placed in front of the LED lamp, focusing the light beam onto the iris aperture diaphragm. The aperture diaphragm can be adjusted to constrain the amount of incident light coming through. The main function of this setup is to control the angle of the incidence beam. The focus lens, located after the aperture diaphragm, aims to create a parallel light beam. This is because the back focal plane of this focus lens is on the aperture diaphragm. It should be emphasised that a good alignment of the optics involved will lead to a uniform illumination, which is extremely important if one is to observe the subtle contrast variation that occurs during domain changes. Afterwards,

the parallel light beam will pass through the field diaphragm and polarizer, becoming a linearly polarized light beam.

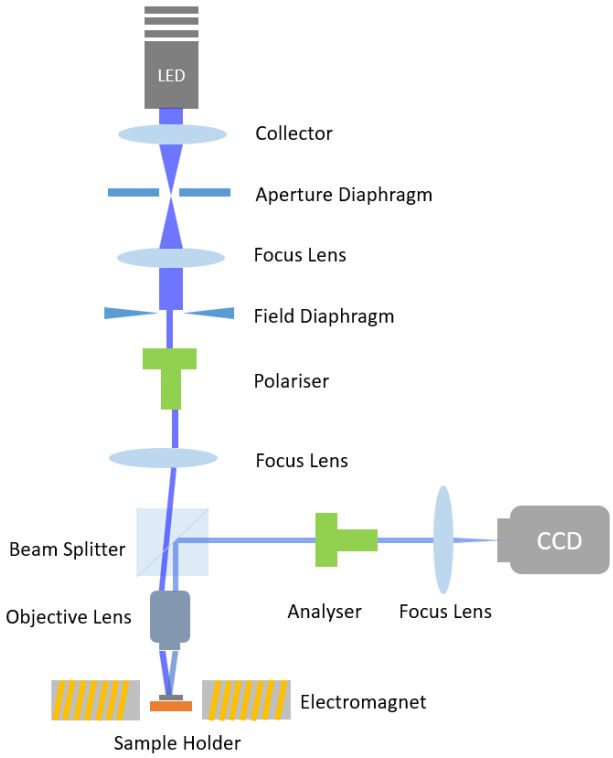

Figure 33. Wide-field Kerr Microscopy. The setup uses off-centred aperture sensitivity for Longitudinal Kerr effect.

Whether or not the beam is parallel can be confirmed by moving a target further away from the lens, then adjusting the position of the lens upon its translation stage and making sure the illuminated area of the target remains unchanged. An objective lens is placed into position and adjusted so that the incident light passes through it between the two poles of the electromagnet. In our experimental setup, an objective lens with the higher numerical aperture (NA=0.55), magnification (50×) and long working distance (more than 1.3 cm) was needed. After reflecting from the sample surface, the light beam intensity changes, along with the polarization. This is the result of the magneto-optical Kerr effect as it passes through the objective lens. It is then diverted by a polarising beam splitter away from the original incident light beam. This polarising beam splitter has a transmission percentage of 90% of p-polarized light and a reflectance percentage of 99.5% of s-polarized light. The plane of the incident light is a p-polarized and as such, the plane of the polarizer needs to be aligned along the p-polarized light as required for Kerr microscopy. The analyser, which is another

polarizer, is set nearly perpendicular to the first polarizer. This is to achieve maximum extinction in one of the domains to provide an optimum magnetic domain contrast. When the light beam, together with the polarization changes, passes through the analyser, the analyser interprets the polarization information as intensity variation. Finally, the intensity variation is captured by the Hamamatsu ORCA-ER CCD camera. This particular setup utilises a Glan-Taylor prism as both the polarizer and analyser. This polarizer has an extinction ratio of greater than 105 :1, which is sufficient to observe the weak Kerr rotation. As we can see from Figure 34, there are two potential practical modes that can be easily modified with respect to the MOKE geometries we mentioned earlier (Chapter 2 -2.6.2).

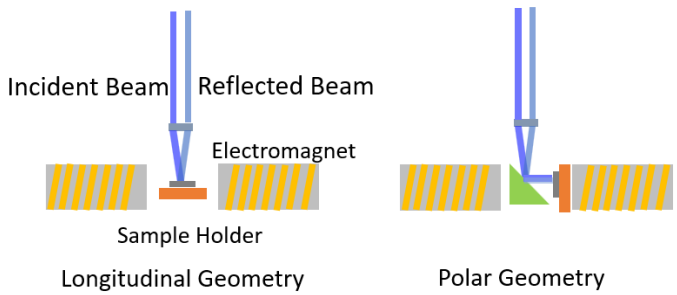

Figure 34. Schematic Diagram of the Kerr imaging system with two different working geometries.

3.1.1 Aperture Diaphragm

The aperture diaphragm is one of the most important parts of the Kerr microscope. Closing and opening the aperture diaphragm will vary the angle of incidence, while moving the aperture diaphragm off-centre will determine the MOKE geometries that the microscope will observe. Therefore, the aperture determines the angle of incidence, with the largest angle of incidence being limited by the numerical aperture of the objective lens. Placing a Bertrand lens in front of the camera can help correct the focus, as this lens has the right focal length to focus the back focal plane of the objective lens to the camera. The cross-shaped image (see Figure 35) describes the extinction zone when the polarizer and the analyser are crossed (cross polarized) to achieve maximum extinction in the sample image. If the aperture iris is set to the centre, the entire alignment will be straight, and the angle of incidence will be zero

degrees. Thus, the Kerr rotation resulting from the in-plane magnetization (longitudinal and transverse MOKE components) cancel each other and so the net Kerr rotation will be zero. Consequently, in this setup, the sensitivity is with the out-of-plane magnetization.

On the other hand, an off-centred aperture iris, resulting in an oblique incident, is required for longitudinal and transverse Kerr rotation. The aperture iris positions for the longitudinal and transverse Kerr effects are shown in Figure 35. Because the longitudinal Kerr effect can only be detected in oblique incidence, the square aperture is positioned off-centre, at one arm of the extinction cross. This gives an incident light with its plane parallel to the magnetization direction of the sample. The longitudinal effect gives a stronger magnetic domain contrast than transverse effect, since the transverse effect has higher noise. This is because the Kerr signal comes from the light intensity variation, where much of the light source noise feeds in with the result. Conversely, the polarizer and analyser are cross-polarized near to extinction in longitudinal sensitivity, which results in most of the unwanted signal being removed. Figure 36 gives a demonstration of different aperture iris stop positions and their corresponding Kerr images.

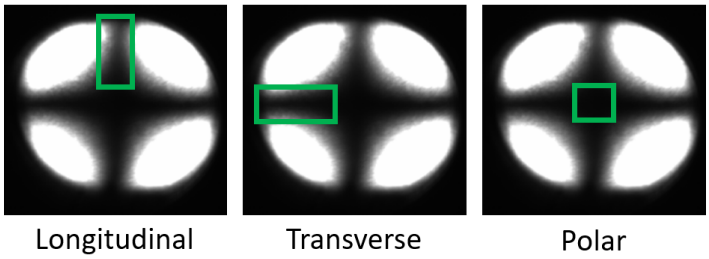

Figure 35. Cross shape extinction cross, aperture iris positions and their corresponding MOKE geometries.

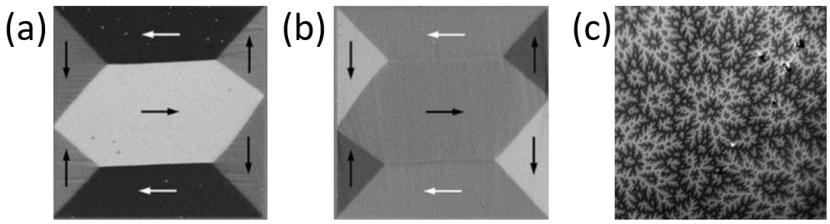

Figure 36. Magnetic domains in a $Ni_{81}Fe_{19}$ patterned film, imaged in MOKE with different sensitivities, (a) is longitudinal extinction cross type, (b) is transverse extinction cross type and (c) is polar extinction cross type [99].

3.1.2 Electromagnet

The electromagnet used in our setup has a limit of 2.8k Oe with magnetic poles separation of 27 mm. The magnetic field strength is controlled by a computer running a LabVIEW programme. A 1000W amplifier is used as the power supply for the electromagnet. The voltage output signal from the LabVIEW is connected to the amplifier, which then converts this signal into the power required by the electromagnet while the electromagnet produces the required magnetic field. The amplifier has bi-polar ability and can therefore produce positive and negative field depending on the sign of the output voltage signal from the computer. The magnet has a magnetic field of around 1700 Oe and -1700 Oe. The value of amplifier input voltage and magnetic field are directly proportional to each other. Therefore, between these values, any change in the amplifier input value will cause a directly proportional change in the magnetic field strength [100]. As the Permalloy used in the following experiments has a relatively low saturation and coercivity field at its easy axis, a magnetic field with ± 350 Oe was applied. As the Co/Pt has a higher coercivity, a magnetic field with ±1700 Oe was applied.

3.2 Focus MOKE

The Focus MOKE is based on the standard MOKE microscope design [98]. The key difference is that the Focus MOKE has an objective lens, which is applied to focus both the laser beam (for detection) and LED (for sample illumination) on to the sample surface. After initiating the magnetization, the measurement is repeated many times (or a single time) with the field gradually increasing and then decreasing, to plot the hysteresis loop, which can show the magnetization reversal occurring in the sample.

A schematic diagram of the polar MOKE system is shown in Figure 37. A continuous wave (CW) He-Ne laser with a wavelength of 633 nm and a maximum output of 2 mW was used as the light source here. A polarizer was placed immediately beyond the CW laser, making the laser beam which passes through the polarizer become p-polarized, and then focused on the sample surface with an objective lens. The reflected laser beam, together with the Kerr rotation, will be collected and directed

to the optical bridge detector. An electromagnet is set parallel with the sample for longitudinal MOKE geometry. The illumination path is required for imaging the sample surface, so that we can make sure that the laser is focused on the tiny structure we want to measure. The optical spot size is critical in the Focus MOKE. The minimum spot size is determined by the objective lens' numerical aperture (NA=sin(D/2f)), where D is the diameter of the lens and f is the focal length. The diameter of the focus spot passing through the objective lens is d=(2λ/πNA). As a result, the focus spot in our Focus MOKE is around 733 nm.

The addition of the objective lens in the Focus MOKE, as compared with the traditional MOKE setup, further extends the function of the traditional MOKE, so that the MOKE measurements can be applied to tiny structures such as nanowires. Similarly, the advantage of the Focus MOKE, compared with the wide-field Kerr imaging system mentioned earlier, is that the Focus MOKE requires fewer optics than the Kerr imaging system, and it doesn't require a very strict alignment of all the optical components. The disadvantage is that, unlike the Kerr imaging system, it cannot give the domain or domain walls motion.

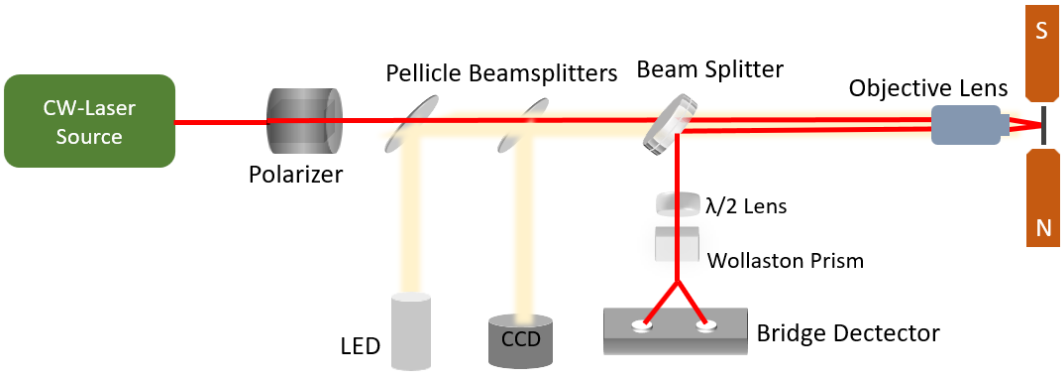

Figure 37. Typical setup for Focus MOKE.

3.2.1 Bridge Detector

As mentioned in Chapter 2, a linearly polarized light, once reflected from a magnetic surface, will become elliptically polarized light and its polarization axis will be rotated. The most common way to detect the rotation of the polarization is to use the so called crossed-polarizer configuration. In this configuration, the first polarizer P, is placed to initialise the polarization of the incident light. The analyser A is placed after reflection, with its polarization axis nearly orthogonal to P. Any variation in polarization of the reflected beam will be converted to intensity change in the transmitted beam after analyser A [101]. The light intensity detected is given by:

$$I = R(\alpha_A^2 + 2\alpha_A\theta + \theta^2 + \varepsilon^2) \tag{3.1}$$

Here, R is the reflectivity, α_A is the polarization orientation of the analyser, θ is the rotation change, and ε is the change in ellipticity. Due to the Kerr rotation being relatively small, only around 10^{-3} rad, the terms θ^2 and ε^2 are negligible. Thus, in the dynamic case, and taking the partial derivative of Equation 3.1, the detected intensity variation will be given as:

$$\Delta I = 2R_0\alpha_A\Delta\theta(t) + \alpha_A^2\Delta R(t) \tag{3.2}$$

Here, Δθ(t) is the transient Kerr rotation representing the magnetization dynamics and ΔR(t) is the transient reflectivity change. This is nonmagnetic and caused by electron and lattice temperature variation. The above equation suggests that the increase of α_A will enhance the signal sensitivity. However, this will also enhance the nonmagnetic background scaling α_A^2 at the same time. Ideally, the smaller α_A the better. Unfortunately, when α_A becomes close to 0, the terms θ^2 and ε^2 are no longer negligible, and this will highly impact the signal to noise ratio (SNR).

Using a crossed-polarizer configuration, to improve sensitivity to small rotations in the polarization of the reflected light and reduce the influence of any laser intensity drift, has its limitations. A balanced-diodes optical bridge detector is therefore used. The optical bridge detector has a Wollaston prism instead of the Glan-Taylor prism used in the traditional cross-polarizer configuration. A Wollaston prism can split the incoming laser beam into two linearly-polarized components in orthogonal directions. The light intensity of each component is then measured by a pair of photodiode

detectors. These detectors are very sensitive to small rotations in the polarization of an incoming beam, and so any change in polarization caused by the magneto-optical Kerr effect can be measured by taking the difference between I_x and I_y. The intensity is given by the square of the amplitude:

$$I_x = A_x^2 = \left(A\cos\left(\frac{\pi}{4}+\theta_k\right)\right)^2 = A^2 cos^2\left(\frac{\pi}{4}+\theta_k\right) \tag{3.3}$$

$$I_y = A_y^2 = \left(A\sin\left(\frac{\pi}{4}+\theta_k\right)\right)^2 = A^2 sin^2\left(\frac{\pi}{4}+\theta_k\right) \tag{3.4}$$

Let us assume the probe laser beam entering the detector has an amplitude A ($I_0=A^2$, where I_0 is the intensity of the probe beam). At the beginning, when there is no external magnetic field applied to the sample, the polarization plane of the probe lies at an angle of φ=45° with respect to the polarization axis of the Wollaston prism, so that the intensity of I_x and I_y are balanced. Since the initial difference between these two photodiodes is zero, a variation of the Kerr rotation θ_k can be easily detected as:

$$I_x - I_y = A^2\left(cos^2\left(\frac{\pi}{4}+\theta_k\right) - sin^2\left(\frac{\pi}{4}+\theta_k\right)\right) \tag{3.5}$$

$$= A^2\left[cos\left(\frac{\pi}{4}+\theta_k\right) + sin\left(\frac{\pi}{4}+\theta_k\right)\right] * \left[cos\left(\frac{\pi}{4}+\theta_k\right) - sin\left(\frac{\pi}{4}+\theta_k\right)\right]$$

Since:

$$sin\left(\frac{\pi}{4}+\theta_k\right) = cos\left(\frac{\pi}{2}-\frac{\pi}{4}-\theta_k\right) = cos\left(\frac{\pi}{4}-\theta_k\right) \tag{3.6}$$

So that the difference between I_x and I_y is given as:

$$I_x - I_y = -A^2 sin2\theta_k \approx -2A^2\theta_k = -2I_0\theta_k \tag{3.7}$$

From Equation 3.7, it can be seen that the signal obtained is proportional to the Kerr rotation angle θ_k. Thus, an important improvement on the traditional cross-polarizer configuration is achieved.

Overall, the optical bridge detector has many advantages when measuring changes in magnetization. Because it uses a two-photodiode scheme we can measure the difference between the two photodiodes. As a result. we can compensate the instabilities in laser intensity. Meanwhile, the SNR can be significantly improved, which is extremely helpful for ultrafast magnetization dynamics experiments.

3.3 TR-MOKE

The time-resolved magneto-optical Kerr effect (TR-MOKE) technique is widely used in magnetization dynamics measurements. This experimental setup was based on the optical pump-probe technique. As such the magnetization of the sample is optically stimulated by a pump laser pulse. Then, after a certain time delay, a probe laser pulse will arrive at the sample to probe the changes in the magnetization. This process is repeated many times in order to obtain good SNR, and the repetitive measurements are attained as a result of the frequency of the laser repetition rate. An external field is normally applied to reset the magnetization after each pump excitation. As long as the delay time between the pump and the probe remains unchanged, the temporal magnetization information sensed by the probe will be constant. The temporal resolution is determined by the pulse width of the probe pulse. As the TR-MOKE technique will be applied to the laser induced precession motion in the Co/Pt multilayers, the detailed schematic diagram of the TR-MOKE setup can be seen in Figure 62, Chapter 5 (page 117) where that subject is addressed. In this section, several key issues that arise during the TR-MOKE setup will be discussed, including laser frequency, delay line, pump-probe beam overlapping and determination of laser spot size.

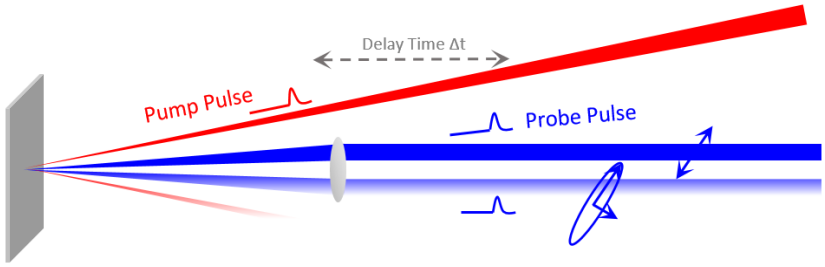

Figure 38. Schematic Diagram of the Pump and Probe Time-Resolved Magneto-optical Kerr Technique.

3.3.1 Laser Frequency

Laser frequency is of great importance to dynamic measurements. Normally, a high repetition rate can achieve the desired SNR, as more the probe pulses during the measuring period, the higher SNR. However, very high repetition rates will result in significant thermal accumulation issues, as the laser induced heat cannot dissipate completely during each pump-probe cycle. The heat accumulation will naturally affect experimental conditions and becomes pronounced with higher pump fluence. Therefore, a laser source with a repetition rate in the 1 kHz range is preferred. The laser induced precession dynamics in the Co/Pt experiment was conducted in Nanjing University, China, where the laser source is a Coherent Libra laser system with a pulse width of 60 fs and a repetition rate of 1kHz.

3.3.2 Delay Line

The time delay is of great importance in pump-probe measurements. This is controlled by a combination of the retroreflector mounted on a motor translation stage. By moving the retroreflector forward or backward, the length of the probe light path is varied, and thus the time delay time can be controlled. The reflected light beam from the retroreflector is parallel to the direction of incidence. In order to maintain the position of the probe spot on the sample surface, the incident beam of the retroreflector must be strictly perpendicular to the retroreflector's base plane. To ensure this, one can extend the reflected beam to a long distance using reflective mirrors, allowing one to check that the laser spot is stable when moving the stage forward or backward. In the current investigations the translation stage used to control the position of the retroreflector is a linear translation stage with integrated stepper motor. The resolution is 2 μm, thus the calculated temporal resolution is around 13.3 fs (2 μm×2/c, c is the speed of light). However, it is preferable to move in steps larger than five times the resolution, to minimise the potential backlash effect. Zero delay refers to the overlap of the pump and probe due to the equal optical path length. By adjusting the optical path of the two beams from the first beam splitter to the sample surface, the approximate position of the zero delay can be defined. The zero delay can be observed in the time-domain reflectivity scan obtained from an GaAs sample, as shown in

Figure 39, the reflectivity data is caused by the interference between the reflected probe and the scattered pump light when they reach on the sample surface at the same time.

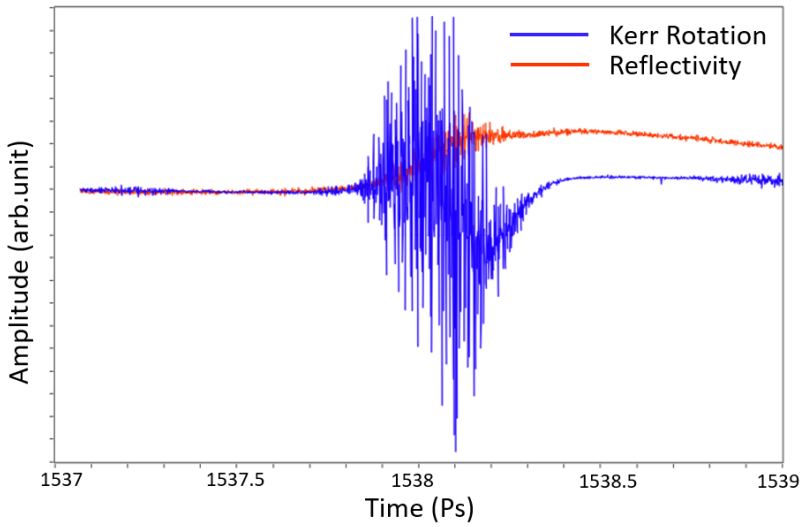

Figure 39. The time-domain scan signal around zero delay, the blue line is the Kerr signal, and the red line is reflectivity change. Image courtesy of Mr. Guanqi Li, another Ph.D student in our group.

3.3.3 Pump Probe Beam Overlapping and Spot Size Determination

An imaging system can be applied to directly observe the spatial overlap condition of the pump and probe beams on the sample surface. There are two methods for taking images of the sample surface using a CCD camera. The simplest way is to take the photo directly by placing the camera close to the sample. To achieve this, one simply has to build up an imaging light path similar to that in the Focus MOKE setup (Figure 37, Section 3.2). However, the intensity could be too bright, due to the image being formed directly by a part of the reflected laser beam. As such, a proper attenuation of the laser beam is necessary. After checking for overlapping, it would be better to remove the beam sampler to avoid reduction in the probe intensity for signal detection.

The beam spot size on the sample surface is also of significant importance for calculating pump fluence. There are several approaches for measuring the beam spot

size. One method is the so called “knife-edge” method. Moving a knife in the lateral direction of the laser beam will block a part of the light. By measuring the total transmitted energy as a function of the position of the knife, one can obtain the radius of the beam at that position. Due to its accuracy and simplicity, the “knife-edge” method is widely used for spot size determination [83]. Another method is to use laser beam with high intensity to burn a spot on a reference sample. As we can see from Figure 40, the pattern TbFeCo is 150 μm in diameter. When compared with the laser burnt region, the rough laser spot size can be determined as around 50 μm.

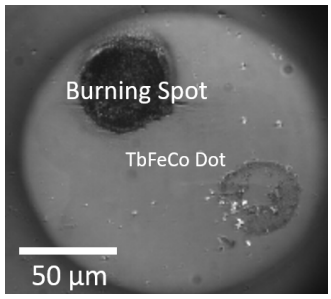

Figure 40. A high intensity laser damages the patterned TbFeCo dot with 150μm diameter. The dark circle is the burnt region.

Moreover, a commercial beam profiler made of a CCD camera can also be used to characterise the beam spot size. After the pump and probe beam spots is adjusted so that they overlap, the beam profiler replaces the sample at the same position. By adjusting the position of the beam profiler to make the two spots overlap again, the diameters of the spots can thus be directly measured. However, one should note that, as each single ultrafast laser pulse contains very high energy, the laser beams must be attenuated significantly down to the working threshold in order to protect the beam profiler from being damaged.

3.4 E-Beam Lithography

Electron Beam Lithography (EBL) is able to fabricate versatile pattern formation, which is always a popular choice for nanoscale fabrication. To fabricate the sample, a cleaned silicon substrate is coated with the resist. After coating, the designed pattern is drawn on the resist-coated substrate by exposing it to the electron beam. The electron beam is focused on the desired area using magnetic lenses and used to engrave the resit (Figure 41(a)). Then the exposed parts are developed in a solvent, resulting in those parts being washed away (38 (b)). Afterwards, the patterned substrate will be deposited by thermal evaporation or sputtering (Figure 41 (c)). The final step is accomplished by soaking the deposited substrate in a substance, usually acetone for PMMA-resist, which completely washes away the remaining resist together with the unwanted material on the top of it. Therefore, the only deposited material now is in direct contact with the substrate (Figure 41 (d)). This entire procedure is called the lift-off. As the quality of the patterned structure is determined by each step of the procedure, it is a very flexible and useful technique for nanoscale pattern fabrication. A summary of this technique is sketched in Figure 41.

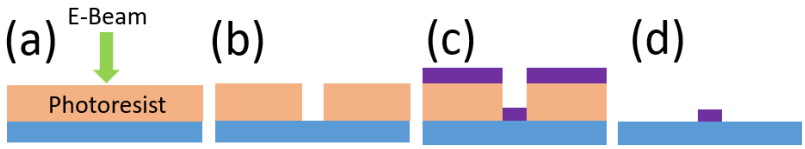

Figure 41. Schematic of the lift-off technique. The light blue is the substrate, purple is the deposited material.

3.5 Thermal Evaporator

Thermal evaporation is one of the fundamental methods for thin film deposition. The evaporation principle is very straight forward. First, the source material is heated to a sufficiently high temperature to release vapour, which is then condensed on top of a clean, cooler substrate to form a thin film. The heating is achieved by applying a large current through a filament boat, which has a certain finite resistivity.

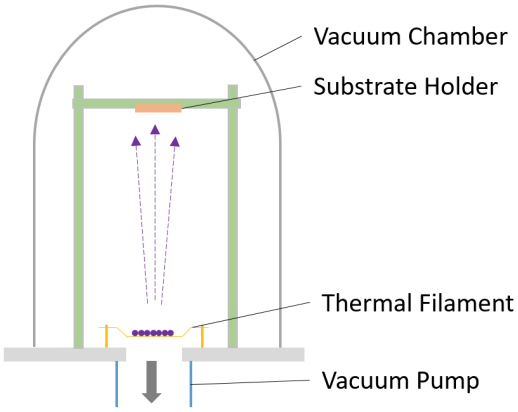

Figure 42. Schematic diagram of the thermal evaporator.

Tungsten is the material most commonly used to create the filament boat, due to its stable chemical properties, the ease with which it can be shaped and the fact that it's melting point is over 3000˚C. The thermal evaporator in the clean room of York University has a distance of over 20cm between source material and samples. This requires a good enough vacuum to form a straight line of vapour deposition. At room temperature (25˚C), the mean free path for air is about 45cm at 10^{-4} Torr. Therefore, the minimum pressure requirement for evaporation to take place is below the level of 10^{-5} Torr. Besides, a good vacuum environment will decrease the likelihood of contamination of the sample. The growth thickness is monitored by a quartz crystal rate meter.

3.6 DC Sputtering

Sputtering is a physical vapor deposition (PVD) method of thin film deposition. This involves ejecting material from a pure element called 'target', and subsequently deposited on the substrate. The bombardment of the target requires the formation of gaseous plasma, which is usually made of inert gas ions such as Argon ions. Enabling to ionize the Ar atoms and to create the plasma in the vacuum environment, a DC voltage is placed between the target and the substrate. These positive ions are accelerated by high electron volts and strike the negative electrode with sufficient force to dislodge and eject atoms from the target. The ejected atoms start to bind to each other at the molecular level, subsequently forming a tightly bound atomic layer. Moreover, the electrons are also accelerated to the substrate during the ionization of Ar atoms which leading to more Ar ions and free electrons.

To enhance the sputtering process, this is so called magnetron sputtering consisting of permanent magnets of opposite polarity located under the target (see Figure 43). These magnets create a strong magnetic field (1000-2000 Oe) parallel to the target surface, thus the magnetic field is orthogonal to the electric field. The field lines generated by the magnetic field trap the electrons released during the ionization process. These electrons follow then helical paths around the magnetic field lines and leading to more collisions with the gaseous neutral atoms near the target surface [102]. With the help of this technique, the efficiency of the sputtering and the quality of coating are improved.

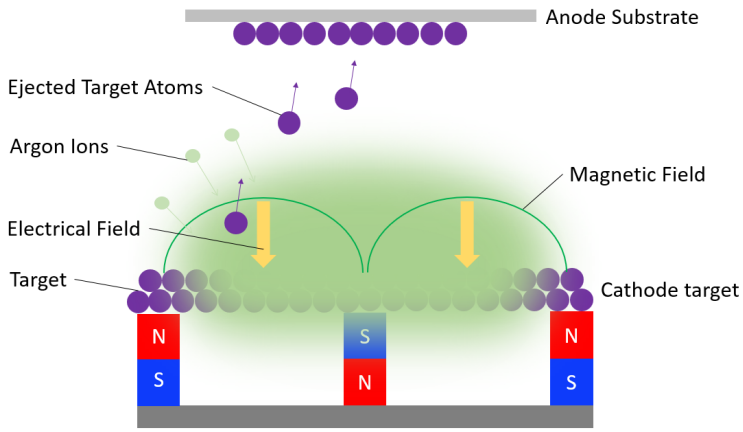

Figure 43. Schematic of the magnetron DC sputtering

3.7 VSM

A vibrating sample magnetometer (VSM) is one of the most commonly used instruments to measure the magnetic hysteresis loops of a magnetic sample. The principle of the VSM is based on Faraday's electromagnetic induction law. The VSM used in York is the MicroSense model-10 VSM, which has high sensitivity (10^{-6} emu) and a high maximum magnetic field of up to around 2 T. It can also measure the temperature dependent hysteresis loops with a temperature variation from 100 to 773 K via a gas-flow system. A basic diagram of a VSM is shown in Figure 43. The sample is mounted on a non-magnetic glass rod and oscillated at the geometrical centre of the air gap between two pairs of fixed electromagnetic poles. An electromagnet is used to magnetize the sample in a certain orientation. It can be rotated on the horizontal plane, and the sample can thus be put in the horizontal or vertical plane by changing the glass rod in order to achieve hysteresis loops along any orientation. The magnetic moment of the vibrating sample produces a changing magnetic flux in the coils. The coil pairs are connected in such a way that the signal due to the moving sample 'adds', and any signal due to fluctuations in the field from the electromagnet 'subtracts', or ideally cancels. Because of the very small value of the signal, a lock-in amplifier is used to detect the signal at the vibrating frequency in order to increase the signal to noise ratio (SNR).

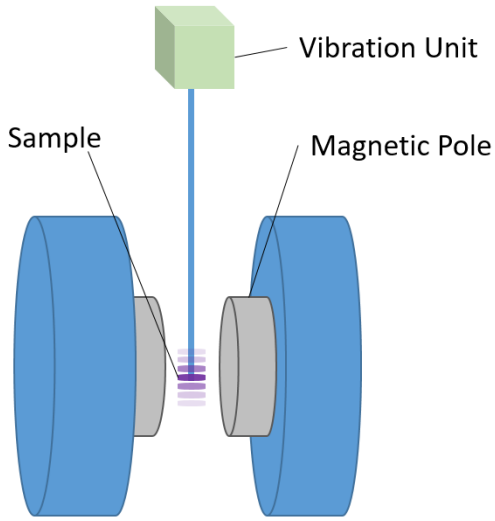

Figure 44. Schematic of the Vibrating Sample Magnetometer.

Chapter 4 Wide-field Magneto-optical Kerr Microscopy study of Ferromagnetic Planar Nanowires

4.1 Introduction

In the recent years, the magnetic domain wall motion in planar nanowire structures have attracted lots of attentions, not only because of their fundamental physics, but also due to the potential applications in sensors and memory devices [31, 32, 103]. Such kind of spintronic devices require a high level of manipulation of domain walls propagation dynamics, which can be achieved by applying an external magnetic field [104-106], a spin-polarized current [107-109], a temperature gradient [25, 110], or an electric field [111, 112]. Polycrystalline Permalloy (usually $Ni_{80}Fe_{20}$) nanowire is one of the candidates among those materials that can be used for memory storage purpose [113], due to their very high magnetic permeability and low coercive field. When artificially varying the geometries of the nanowires [114], the weak magnetocrystalline anisotropy and small magnetostriction also allow the magnetization to be constrained by magnetostatic energy so as to lie along the long axis of the nanowire with spins parallel to the surfaces and edges. The spin orientation tends to follow the local edges of these structures due to the shape anisotropy. This can be utilized to engineer domain wall pinning [115]. For memory applications, the domain walls can be pinned at those notch geometries creating multiple domains, hence two distinct magnetization states can be treated as different memory states allowing the manipulation of stored information [116].

Previous studies have shown that the correlation between the depinning field and the pinning site (notch) geometry is determined by the applied field and the spin-polarized current induced domain wall motion [109, 117-121]. There are two types of domain walls, namely, the vortex and transverse domain walls. While the vortex domain walls (VDW) are energetically favoured in the thicker and wider magnetic nanowires, the transverse domain walls (TDW) are more preferred in thinner and narrower magnetic nanowires [105, 122] as a result of the compromise between the

exchange energy and demagnetizing energy. The nanowire configuration and chiralities of these two types of domain walls will strongly influence on the domain walls propagation dynamics. Recently, D. Atkinson *et al* reported that the different domain wall structures will have different pinning interactions with a single triangular notch structures, since the spin configuration through a structurally asymmetric feature will have different energetic barriers to pin the propagating domain wall. This energetic variation manifests as a difference in the external magnetic field required to push the wall through the pinning point [123]. In a magnetic material with weak magnetocrystalline anisotropy, the magnetostatics energy will be dominant, thus notch geometry engineering will modify the domain wall potential energy. Furthermore, D. Atkinson *et al* investigated controlling the interactions of domain walls with asymmetric pinning structures by selecting the magnetization state of the domain wall using external magnetic field applied transverse to the long axis of the nanowires. This work provided an additional degree of freedom for controlling domain wall position in potential applications. Another recent research reported the domain wall pinning behavior and the potential-energy landscapes created by notches of two different geometries in planar Permalloy nanowires [104], it is found that the depinning field experienced by a domain wall was relatively insensitive to notch geometry, although the pinning behavior was highly sensitive to both the wall type and the wall chirality spin structure. In this work, they also observed that when pinning sites are comparable in size to the domain wall width then the detailed geometry of the notch is of secondary importance to the domain wall depinning field, for a given domain wall structure will experience very similar depinning from two different notch geometries of the same depth and width. W. W. Zhu *et al* investigated the mechanism of depinning process of vortex domain wall in Permalloy nanowire with an asymmetric notch [124], similarly, by using a focused MOKE microscopy and micromagnetic modeling, they observed two distinct depinning fields by the single-shot MOKE measurements, which suggested that different pinning potential landscapes were formed at the same asymmetric notch, the results were strongly associated with different magnetization dynamics of the vortex domain walls with opposite chirality. The asymmetric notch with a slow and gentle entry slope is conducive to keeping the chirality of vortex domain wall and restraining the transformation between the different types of domain walls during the pinning or depinning process. They also combined the experimental

results with the micromagnetic simulation to further understand the depinning process of magnetic domains walls with a well-defined notch, which were in good qualitative agreement with their experimental results. Moreover, D. M. Burn *et al* studied the domain walls pinning by localized focused Ga+ ion irradiation on Permalloy nanowires via focus Magneto-Optical Kerr (MOKE) Microscopy [125, 126], the results show that localized selective pinning of domain wall structure can be achieved through controlling of the geometry of the irradiated region in nanowire. The pinning behavior depends on the magnitude of the magnetization change, and the length of modified region, also the comparative analysis indicates that reduced saturation magnetization (M_s) is not solely responsible for the experimentally observed pinning effect, this work provides an insightful approach to manipulate the pinning energy.

Besides field-induced domain wall propagation mechanism, the current-induced domain walls motion confined to nanostructures is also of great interest for fundamental studies as well as for technological applications in spintronics devices. S. Lepadatu *et al* successfully fabricated single layer Permalloy nanowires with a variable constriction width ranging from 50 nm to 350 nm, the contribution of domain wall scattering was obtained from the resistance versus applied current measurements without applying any external magnetic field and found to increase with deceasing constriction width [107]. A sharp drop in resistance is observed for the nanowires with constriction point contact (center point of a bow-tie structure) width in the range of 50 nm to 250 nm at a critical current J termed the switching current, while for the nanowires with point contact width larger than 250 nm, no decreasing in resistance was observed, this work suggests that there might be a unified model for ballistic magnetoresistance and domain wall magnetoresistance. Another work by X. F. Hu *et al* presented the PEEM images showing the depinning properties of pulse-current-driven domain walls in well-shaped Permalloy nanowires [127]. They observed a current-driven Barkhausen jumps of the domain wall depinning and motion, a similar phenomenon to the classical magnetic field-drive Barkhausen effect. In fact, for application purpose, current-induced domain wall motion is more practical compared with field-induced domain wall motion. However, in order to achieve applications, understanding and fine controlling field-driven dynamics of the domain walls in the nanowire is an important preliminary work before exploring the current driven motion.

As mentioned in the previous content, these two types of domain wall structures only describe the simplified magnetic moment configurations. However, the ultimate goal is to apply domain wall motion in magnetic memory devices. It is important that we have a comprehensive characterization of the pinning site potential landscape to understand the influence of nanowire width and pinning site geometry. Clearly, those previous research results show that domain wall pinning behavior is complicated. According to those literatures, even in the well-defined magnetic nanowires, stochastic domain walls motion still exists during domain wall nucleation, propagation, pinning and depinning process [105], and the detailed mechanism of the stochastic observation in the experiments remains unclear. This severely affects the precise control of the domain wall motion and its related spintronics devices. During this project, I have studied how the different orientations of the same notch geometry (triangular) affect the depinning site potential landscape. This question is still open and of importance to the understanding of the mechanism of the domain wall dynamics in Permalloy nanowires. To explore this issue, a series of nanowires were fabricated via electron beam (E-Beam) lithography, by changing the geometry of the notch to be able to continuously vary the potential barrier generated by the notch. A wide-field magneto-optical Kerr imaging system was built to directly visualize the domain wall motion in those nanowires. Magnetic hysteresis loops were also retrieved from the Kerr images to analyze the depinning energy of the notches. Furthermore, micromagnetic simulation using Mumax package was also performed to simulate the experimental results. Combining with all these techniques, the potential relation between domain wall motions and the notch geometries of the nanowires was systematically investigated.

4.2 Sample Details and Experimental Setup

This chapter mainly focus on the magnetic domain wall motion in the Permalloy planar nanowires with triangular notch feature. The nanowires were designed via AutoCAD package and then fabricated by Electron Beam Lithography (EBL). The prepared silicon substrate after cleaning and PMMA spin-off was exposed by electron beam bombardment in a Scanning Electron Microscope (SEM) with EBL embedded. The spin angular velocity was set at 4500 rpm to achieve PMMA coating with a thickness around 180 to 200 nm, which is an ideal thickness for nanoscale pattern fabrication [128]. Electron beam exposure was carried out at 20 kV with a spot size of 3, and an area dose of 75 $\mu C/cm^2$. The developer used was MIBK and IPA at a ratio of 1:3, and the developed region was removed by rinsing in pure IPA for 30 to 40 seconds [129], then followed by thermal evaporation of Permalloy ($Ni_{80}Fe_{20}$). Finally, the lift-off process was accomplished by immersing the finished sample into the heated acetone.

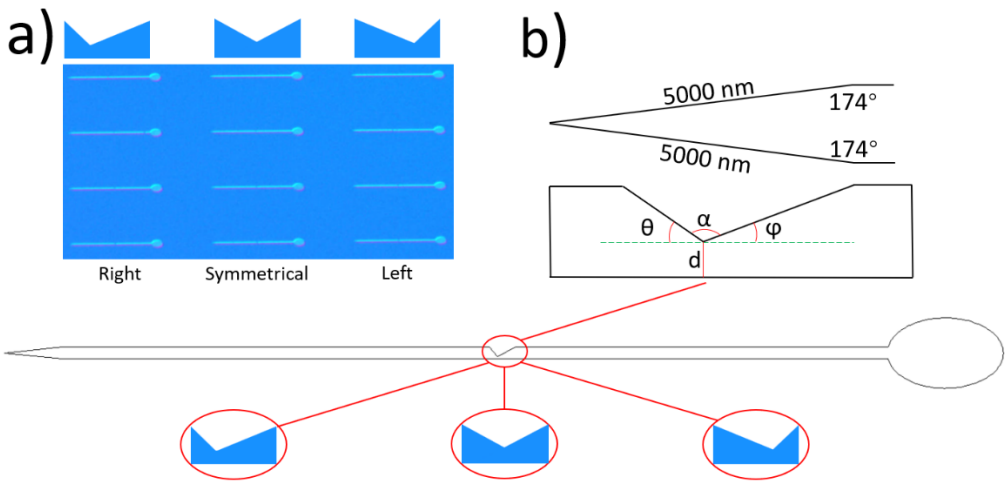

Figure 45. Schematic details of the nanowire and the notch. a) the optical microscope image of the nanowires array with a magnification of 10X. Left, Symmetrical and Right denote three different types of the notch geometry, from the top to the bottom, the notch depth d is getting narrower, from 800 nm to 200 nm. b) the design details of the tail and the notch and the definition of the angles.

As shown in Figure 45, The total length of the nanowires is all around 70 μm (including nucleation pad) terminated at one end with an elliptical nucleation pad, and

a triangular sharp tail point at the other end (see Figure 45). The width of the nanowires is 1 μm and the thickness is around 20 nm. There is a 5 nm Au capping layer deposited to prevent the samples from oxidation. The triangular notches with different tip orientation are positioned deep halfway along the long axis of the nanowires, the notch depth is varying from 800 nm to 200 nm, stepping in 200 nm increments, so that we can carry out the investigation on notch depth dependence of the depinning field at the same time. The specific parameters of the notch can be seen in Table 1.

Notch Geometry	Right	Symmetrical	Left
Value of θ, φ, d, respectively	47°, 28°, 800 nm	36°, 36°, 800 nm	28°, 47°, 800 nm
	47°, 28°, 600 nm	36°, 36°, 600 nm	28°, 47°, 600 nm
	47°, 28°, 400 nm	36°, 36°, 400 nm	28°, 47°, 400 nm
	47°, 28°, 200 nm	36°, 36°, 200 nm	28°, 47°, 200 nm

Table 1. Specific parameters of the angle θ, ϕ, depth of the notch d.

Meanwhile, all the nanowires involved in the following experiments were examined by Scanning Electron Microscope (SEM). Figure 46 shows the example of the notch geometrical details of the SEM images, the notch depth d in those illustrations are all 200 nm.

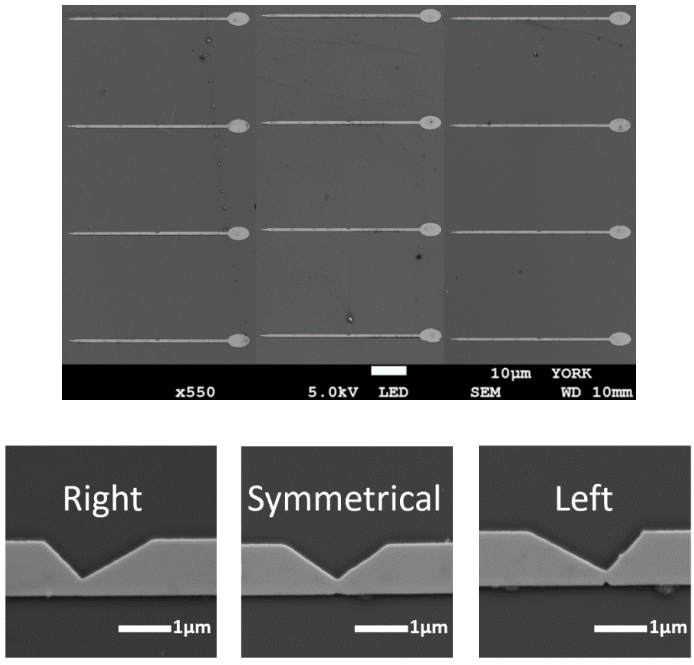

Figure 46. Top SEM show the well-fabricated nanowire arrays with different notch geometries. The bottom are the details of the notches with a magnification of 10,000 times.

Kerr microscopy is the most direct approach to investigate the field driven magnetic domain motion. The wide-field Kerr imaging system setup is sketched in Figure 33 (Experimental Technique, Section 3.1). For the planar Permalloy showing in-plane magnetization anisotropy, to evaluate the spatial distribution of the coercivities at different positions on the nanowires, I select the longitudinal MOKE as our measurement geometry.

For the convenience to depict the experimental results, all the nanowires in the following experiments are labeled as 'notch-geometry+notch-depth', for example, 'L800' denotes the Left type notch geometry with a notch depth d=800 nm, R denotes the Right type notch geometry.

4.3 Results and Discussion

In this section, spatially resolved magnetization analysis was performed using self-built wide-field Magneto-optical Kerr Microscopy with longitudinal configuration. The setup allows the magnetization reversal behavior of individual nanowire with specific notch geometry to be investigated locally. Figure 47 shows that increasing the region of interest selected will increase the value of the detected Kerr signal. A larger area of samples will give higher Kerr signal. Results confirm that our Kerr imaging system is working well, even the region of interest narrowed to an area of 1x1 μm.

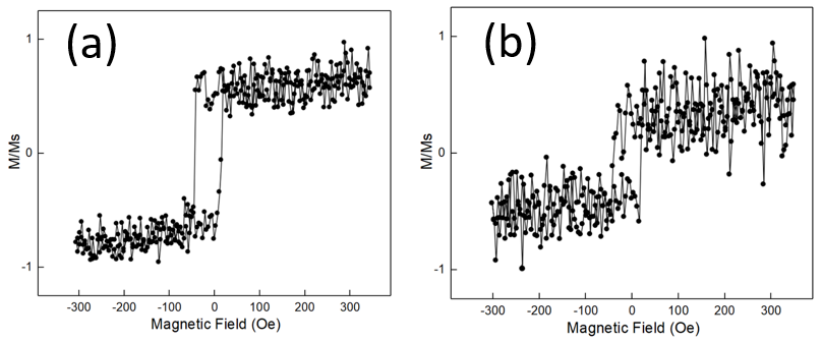

Figure 47. A comparison for MOKE signal from a 5x5 μm region of interest and 1x1μm region of interest.

For the consistency, in the following experiments, the region of interest all set as 1x1 μm. As shown in Figure 48, four different typical positions on the nanowire are selected, nucleation pad (1), the connection between wire and nucleation pad (2), before notch (3) and after notch (4), respectively. The corresponding magnetic hysteresis loops are also retrieved from those four positions so that the domain wall depinning fields can be quantified. During all the experiments, the external field was applied along the long axis of the nanowire from the nucleation pad to the tail, the external field range is ±350 Oe and the field increment is around ±4 Oe according to the current-field calibration. Meanwhile, the important insight into the relationship between domain wall structure and the pinning behavior was achieved by micromagnetic simulations.

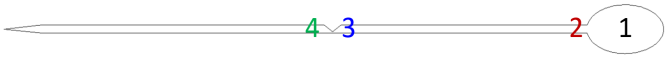

Figure 48. An illustration of the magnetic hysteresis loops extraction positions.

4.3.1 Experimental Results and Analysis

In Figure 49, the Kerr image obtained by the wide-field Kerr imaging system is presented. The images are processed via digital image processing in order to enhance the contrast. From these images, one can see that when the applied field increased to 34±4 Oe, comparing with the applied field at 22±4 Oe, the bottom of the nucleation pad starts to change, and this corresponds to the change of the magnetization state. As the magnetic field keeps increasing to higher field, the contrast becomes more and more distinct, the magnetic domains (black region) nucleated from the pad propagate to the wire parts but get pinned at the notch, until the magnetic field is larger than 107±4 Oe, then the magnetic domains get depinned at the notch, and continue to move to the tail of the nanowires. Reversing this process, from the positive to the negative magnetic field, the hysteresis loops are plotted based on the intensity variation from those Kerr images.

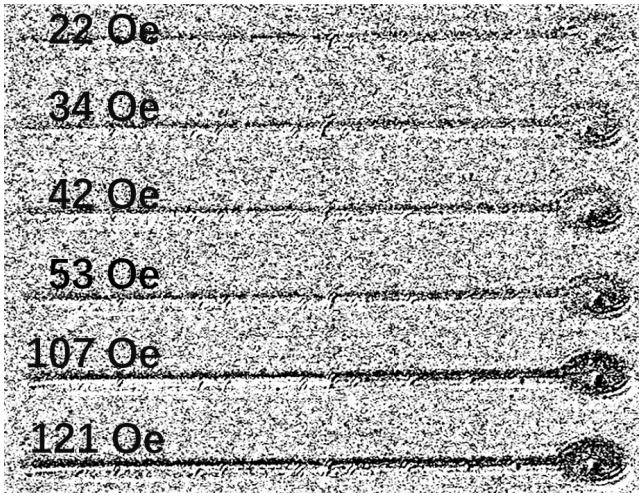

Figure 49. Typical Kerr images obtained by the imaging system. As increasing the applied field. the evolving process of the magnetic domains is revealed.

The three-columns graph in Figure 50 gives the measurements of all the nanowires with different notch geometry and notch depth. From the top to the bottom, d varies from 800nm to 200 nm, respectively. Hysteresis Loops of four selected positions see (Figure 48) were extracted from the nanowires. As we can see from Figure 50, one of the common characteristic is the measured coercivities (H_c) at the junction between the nucleation pad and nanowire (position 2), also the notch depinning field (position 4) increasing as the notch depth d becoming narrower (reduce

from 800 nm to 200 nm). Moreover, when the notch depth keeps increasing, the depinning field will be more sensitive to the notch geometry, even the same triangular feature but opposite orientation (Left and Right) will cause a significant coercivity differences. Especially, when the notch depth downs to 200 nm, the H_c difference of the notch geometry with opposite orientation reaches to 82%, where H_c of L200 is 106±8 Oe and H_c of R200 is 58±8 Oe, the depinning at position 4 (after notch) increased tremendously. We assume the coercivity of the nucleation pad supposed to remain the same, but in the real experimental scenario, the variation is around 8 Oe, thus we estimate the error value is around ±8 Oe, and this applies to all the coercivity measurements. This significant coercivity difference becomes relatively less in the other nanowires with the notch depth boarder than 200 nm. Additionally, the depinning field on the nanowire is also sensitive to the notch depth d, for Left, Right and Symmetrical nanowires with same notch depth d=800 nm, the variation of the coercivities before and after the notch is almost negligible, when the notch depth d=600 nm, the difference of coercivity between before (position 3) and after notch (position 4) gradually unfolded. Finally, when the notch depth goes down to 200 nm, for the same notch geometry, the coercivity at position 4 (after notch) increased considerably. One also can see there is some obvious changes in the column of the Right geometry compares with the column of the Left geometry when the notch depth varies from 800 nm to 200 nm, this indicates the coercivity does sensitive to the notch geometry, but not that much sensitive when compared with the influence of the notch depth. In 2009, L. K. Bogart *et al* reported that the depinning field is insensitive to the notch geometry no matter whether the notch is triangular or rectangular [104], clearly, our results is quite different with theirs. As one can see from Figure 50, when the notch depth d=800 nm or even downs to d=400 nm, the difference of the coercivity on the wire parts (position 3 and 4) is very subtle. But when the notch depth d=200 nm, the coercivity before (position 3) and after notch (position 4) becomes very sensitive to the notch geometry, a more distinct difference in coercivities were observed.

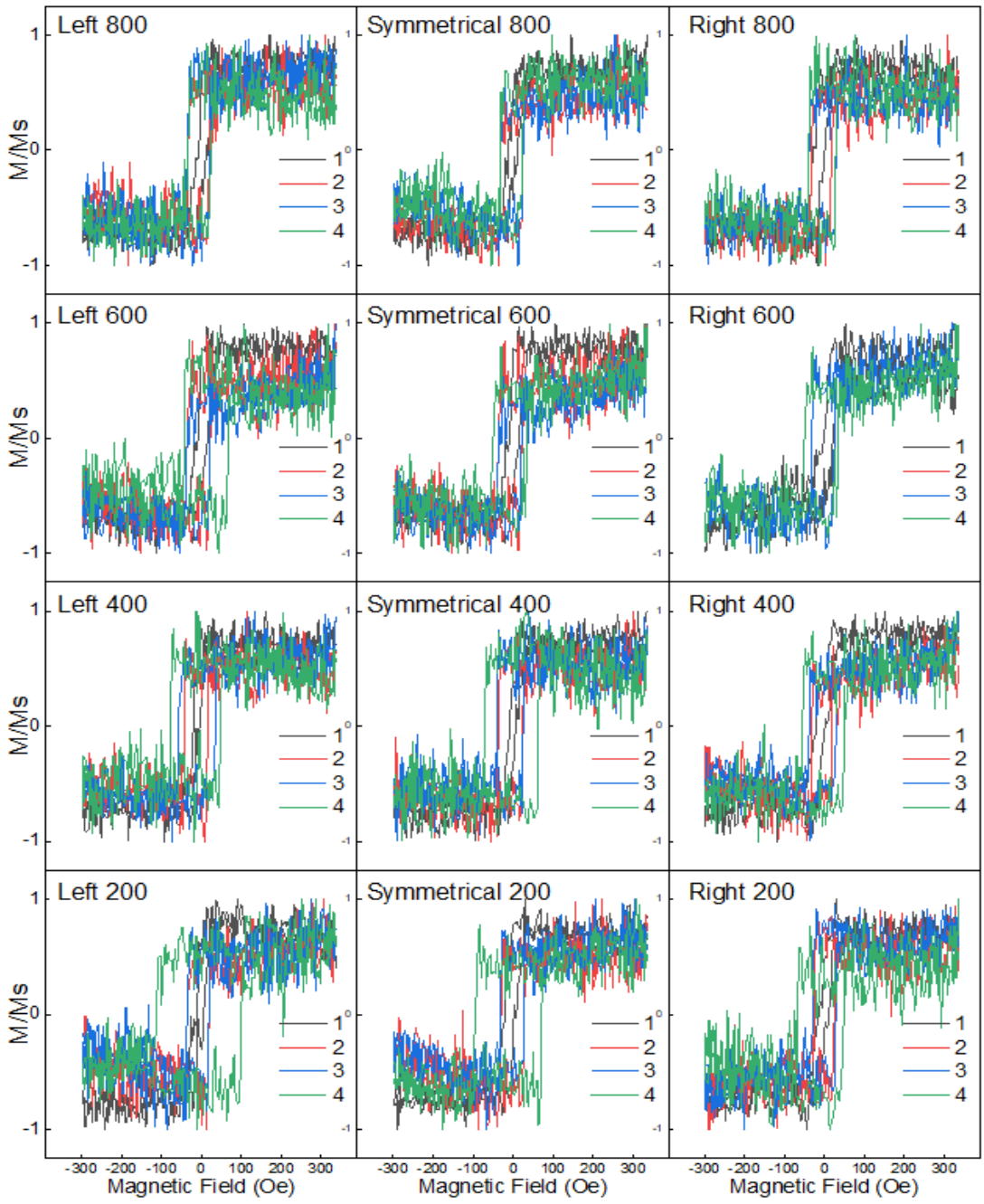

Figure 50. Magnetic hysteresis loops of all the nanowires with different notch geometries. Left, Symmetrical and Right denote three notch geometry types. The digits 1 to 4 represent four positions on the nanowires. All the magnetic hysteresis loops here is single loop.

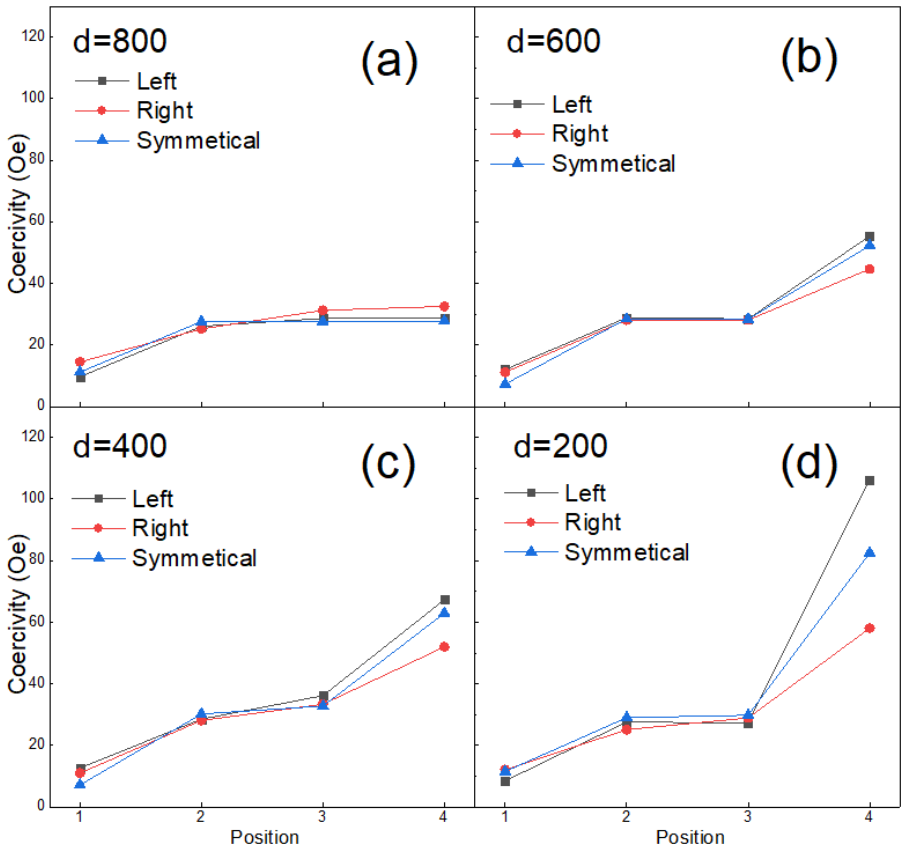

Figure 51. Coercivities variation versus positions of three types of notch geometries with different notch depth value. The lines are guide to the eyes.

The coercivities versus extracted positions are presented in Figure 51. (a), (b), (c) and (d) correspond to four notch depth d from broad to narrow. As we can see from Figure 51, the nucleation field at position 1 doesn't has much difference for all 12 samples, which is around 15±4 Oe. Meanwhile, the coercivities of position 2 (connection between nucleation pad and wire) is always slightly lower than the coercivities of position 3 (before pinning notch), this could be due to the inevitable fabrication defects and surface roughness induced extra pinning energy. However, the coercivities of the samples at position 4 (after notch) are quite different, as the notch depth d goes down to 600 nm, the Left type notch geometry always share a larger depinning field than the Right type notch geometry, and this difference is getting more and more obvious as the notch depth keeps reducing.

Figure 52 shows the comparison between three different types of notch geometries, varying the notch depth from 800 nm to 200 nm and extract the hysteresis loop at position 4, it clearly shows that the Right type nanowires are not that sensitive to the

notch depth as the Left type and Symmetrical type nanowires do. The key different parameter between those types of nanowires is the angle φ. Therefore, an angle dependence of the coercivity variation in the nanowires is demonstrated.

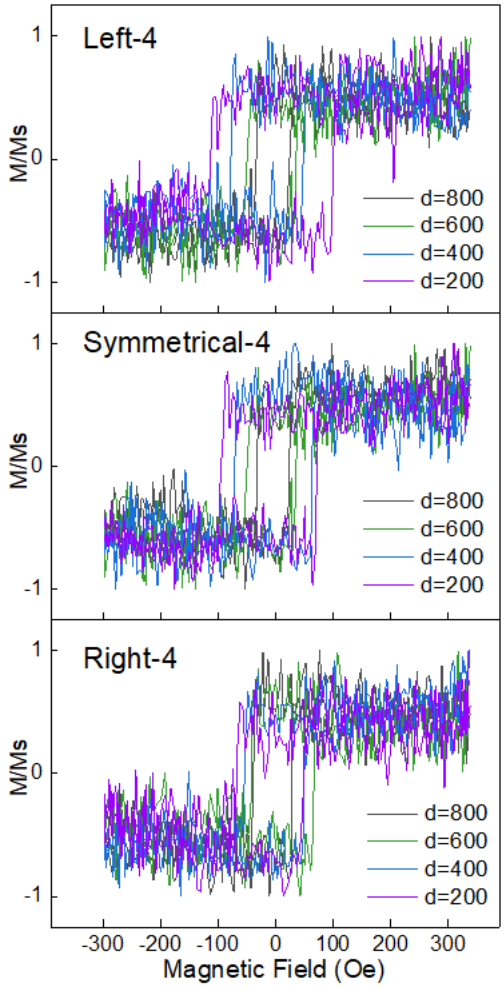

Figure 52. A comparison between three types of notch geometries, when engineering the notch depth d from 800 nm to 200 nm, the variation of coercivities at position 4.

In order to further interpret the interesting finding that when the notch depth down to d=200 nm, the difference of coercivity of the notch feature with opposite orientation becomes significant, we conducted another set of experiments. According to the previous research works [122, 124], there could be more than one depinning field (coercivity at position 4), the depinning field is stochastic due to the different depinning mechanism induced by various types of domain wall, namely, clockwise-vortex wall (CVW), counter-clockwise-vortex wall (CCVW), transverse walls (TW), etc. This will be reflected on the averaged hysteresis loops of multiple measurements.

It should to be emphasized that the magnetic hysteresis loops correspond to the variation of the magnetic moment of the partial select area in the nanowire (position 1 to 4) versus the applied magnetic field, which don't reflect the variation of the total magnetic moment of the nanowires. Figure 53 shows the magnetic hysteresis (M-H) loops also obtained by Wide-field Kerr Microscopy for the three nanowires with different notch geometries (L200 (a), R200 (c), S200 (b)). Those loops here are obtained by averaging over 40 single-shot loops. First of all, we can tell from Figure 53, the nanowires were fully saturated under the external magnetic field, in Figure 53 (a), the Left type notch geometry with θ=28°,φ=47°,d=200 nm, when the external magnetic field decreased to zero and then began to increase in the negative direction, two distinct jumps appear at -104±8 Oe and -116±8 Oe, this correspond to two distinctively different depinning field of the domain wall. For the descending part of the loop (from negative applied field to positive applied field), it also shows two obvious different depinning field, +109±8 Oe and +119±8 Oe, respectively. In Figure 53 (c), the Right type notch geometry with θ=47°,φ=28°,d=200 nm, when the external magnetic field decreased to zero and then began to increase in the negative field direction, two jumps were observed, -62±8 Oe and -68±8 Oe, as for the descending part of the loop, another two abrupt jumps were observed, +89±8 Oe and +98±8 Oe, respectively. However, in Figure 53 (b), the symmetric nanowire with θ=36°, φ=36°,d=200 nm, only the ascending part of the magnetization process shows two distinct jumps, the first jumps at +83±8 Oe, then at +98±8 Oe, the descending part of the magnetization process (from positive saturation to negative saturation), only one jumps is observed at -103±8 Oe. It is clearly that the depinning fields of the three different types of notches are not same, which indicates that the notch geometry dependence also plays an important role in the magnetization properties in the Permalloy nanowire. The reason why the descending part of the symmetrical type notch can only observe one jumps, may due to unavoidable structural defect during the nano-fabrication process, edge and surface roughness and some other artificial effects, those defects get the domain wall pinned at somewhere in the nanowire [130]. However, these artificial effects play less role during the whole process. Another possible reason could be due to the limitation of the instruments, the subtle difference of the domain wall nucleation and pinning processes may not easily be distinguished in the experiments. In Figure 53 (d), I merged the three loops together, one can tell

that, the depinning field of the three different type nanowires is slightly different, but still non-negligible, not matter what kind of domain wall type effects the final depinning results, the depinning field of the Left type notch is always larger than the depinning field of the Right type notch. The innate difference of those three types of nanowire lies within the angle φ [see Figure 46 (b)], the angle between the first hypotenuse close to the nucleation pad and the bottom line of the nanowire. We believe the transverse wall (TW) and the vortex domain wall (VW) have different preferences on the angle φ.

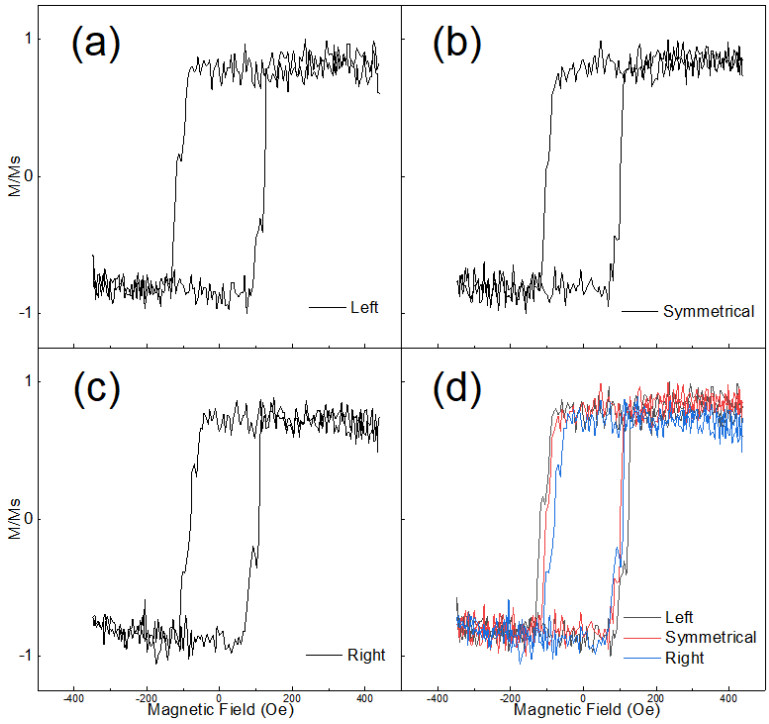

Figure 53. Averaged magnetic hysteresis cycles for three types of nanowires with different notch geometries. (a) is left type with d=200nm, (b) is Symmetrical type with d=200 nm, (c) is Right type with d=200nm and (c) is the comparison of the three different notches.

4.3.2 Micromagnetic Simulations and Discussion

To further understand the experimental results and the detailed processes of domain wall pinning and depinning, micromagnetic simulations were performed using Mumax software package [131]. The standard material parameters of Permalloy are used [108, 132]: Ms=860 emu/cm^3, A=13×10^{-12} J/m, α=0.005, and K=0, where Ms is the saturation magnetization, A is the exchange constant, α is the damping constant, K is the crystalline anisotropy constant. In the modelling, the smooth-edged nanowires with 20 nm thickness, 200 nm width, and 17.2 μm length are considered, and area discretized in cell size of 5×5×20 nm^3. The software uses an iterative process to solve the Landau-Lifshitz-Gilbert equation for each cell of a finite element mesh. To reduce the computation for equilibrium state, a α value of 0.5 was used in the following simulation [133]. There were two groups of micromagnetic simulation carried, in the first group, the dimensions of the notch are same as in the experiments. In the second group, to enlarge the differences of the coercivity, I further increased the notch depth d, and tuned the relative angles of the notches.

4.3.2.1 Micromagnetic Simulations for the Experimental Results

To clarify how the depinning fields take place and gain insight into the dynamic magnetization behaviours, during the first group of simulations, the dimensions of the notch geometries used are designed exactly same as those in the experiments, so that we can restore the entire magnetization processes. The simulations were initiated from the nucleation pad, the applied external field is in 5 Oe steps until the DW structure de-pinned from the notch region and propagated freely along the nanowire till the abrupt end, when the nanowire saturated, a reversing magnetic field was applied from the opposite direction, but still parallel with the nanowire, in another word, with the easy axis of the nanowire.

The hysteresis loops retrieved from the simulations are presented in Figure 54, the overall trend of the variation of the coercivities are in good agreement with the experimental results. From the top row to the bottom row, the notch depth varies from

4/5 width of the nanowire to 1/5 width of the nanowire, respectively. The hysteresis loops of the four identical positions, namely, nucleation pad (1), wire-part after the nucleation pad (2), before the notch (3) and after the notch (4) were retrieved. Generally, the coercivity increases as the notch depth decreases for all the three different types of the notch geometries, which is similar with the phenomenon observed in the experiments. In the position 1, 2 and 3, no matter how the notch depth and geometry changes, the coercivities are most remain unchanged. However, in the position 4, the coercivity value begins to dependent with the notch depth and geometry as well. As the notch depth keeps decreasing, the size of the notch increases, consequently, the larger artificial protrusion increases the energy barrier for magnetization depinning. When comparing the three columns, for the column with left type notch geometry, the coercivity is highly dependent with the notch depth, the hysteresis loop of Left 200 is much boarder than the loop of Left 800 at position 4. Conversely, the Symmetrical and Right columns are not that sensitive to the notch depth variation compares with the Left column. This is also in good accordance with the experimental result. Moreover, a slightly shift of the hysteresis loop can be seen from the single-shot simulation performed for Left 200 nanowire, which indicate two distinct different depinning field of different types of wall chirality [124]. The different types of wall chirality will highly affect the energy needed for the domain wall depinning at the notch [122]. This shift of the hysteresis loop can only be observed from the single-shot simulation or experimental measurement, because the multi-shot measurements will average lots of hysteresis loop, thus reflect the shift of the loop in terms of the step-like loop (see Figure 53 in page 113).

Now Take a close look at the coercivity difference. In Figure 55, the coercivities variation versus positions of the three types of notch geometries with different notch depth is presented. As we can see in Figure 55, for the nucleation pad (position 1), the coercivities don't have much difference for all the nanowires, which is typically around 40±5 Oe. This corresponds to the external field needed to generate the domain wall vortex on the nucleation pad. The coercivities of position 2 and 3 are the same, which is around 180±5 Oe. This is different with the observation in the actual experiments. During the experiments, the coercivities of position 2 are always slightly lower than the coercivities of position 3, as explained earlier, the fabrication defects

and surface roughness may the reasons behind it. Similar with the experiments, the coercivities of the position 4 shows a distinct difference when the notch depth narrows down to 200 nm. For the Left 200, the coercivity at position 4 is 425±5 Oe, while the coercivity at position 4 of Right 200 is 285±5 Oe. One may notice that the coercivity differences of the simulation is smaller than the differences we observed in the experiments. In the experiments, the coercivity difference of the notch geometry with opposite orientation (Left 200 and Right 200) reaches to 82%, but in the simulation, the difference only reaches to 49%. This may also attribute to the influence of edge roughness on the magnetization switching. M. T. Bryan *et al*., measured the rectangular Permalloy nanostructures with different edge roughness but same average width, they found that the coercivity increases linearly with the peak-to-peak edge roughness. Large edge roughness could more than double the coercivity of the nanowire structure. The edge roughness is inevitable during the fabrication of the nanowires, and when the edge roughness is very large, the surface roughness may also increase. However, we didn't take the edge roughness into consideration during the simulation. The masks for the simulation show very smooth edge. Thus, the increased coercivity contributed by the edge roughness cannot be explained from the simulation results very well. Nonetheless, the micromagnetic simulations are informative, in the following section, a further analysis will give insight into the interactions taking place between the DW spin structure and the notch regions.

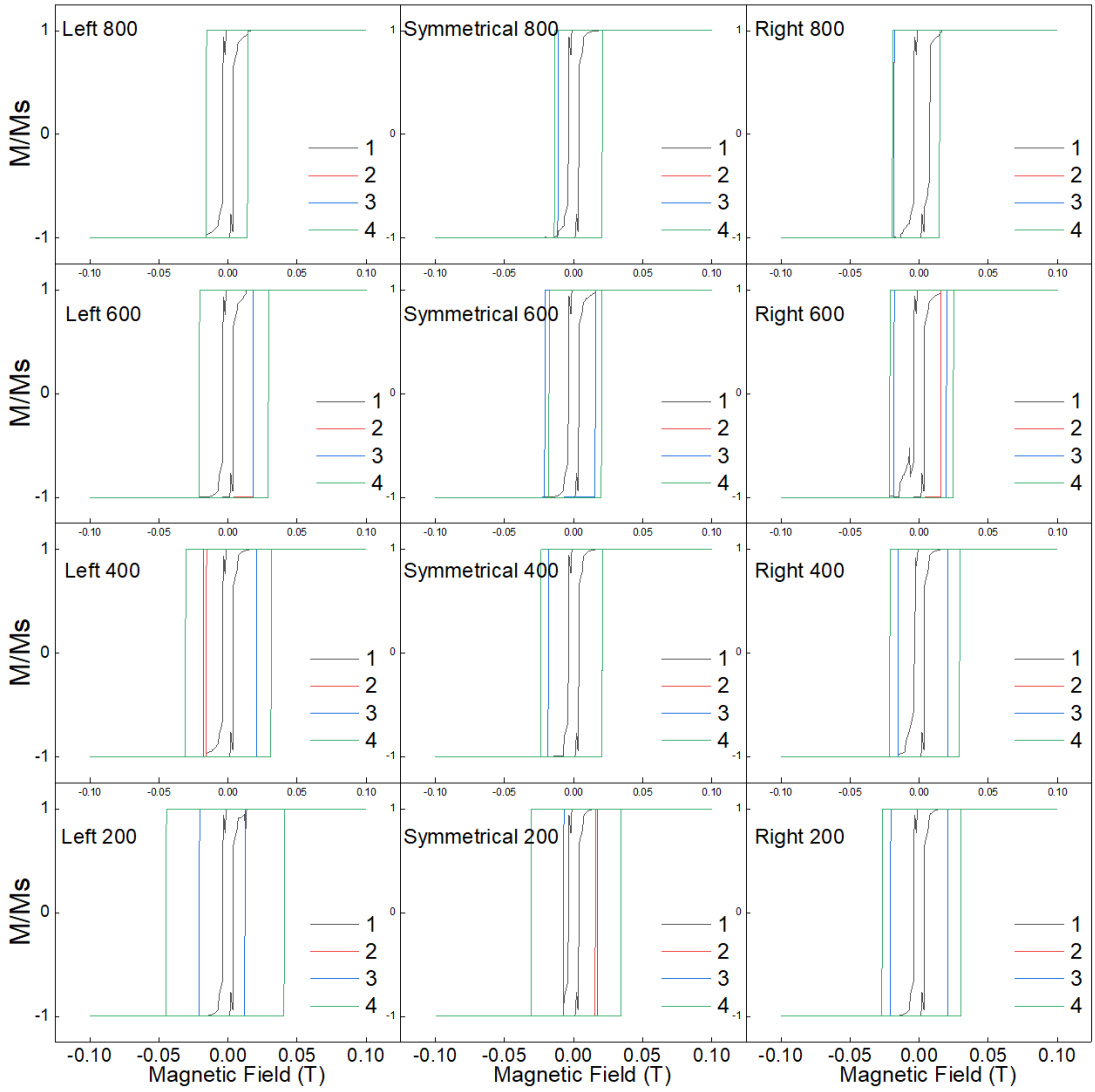

Figure 54. Magnetic hysteresis loops of all the nanowires retrieved from the micromagnetic simulations. Left, Symmetrical and Right denote three notch geometry types. The digits 1 to 4 represent four positions on the nanowires. All the magnetic hysteresis loops here is single loop.

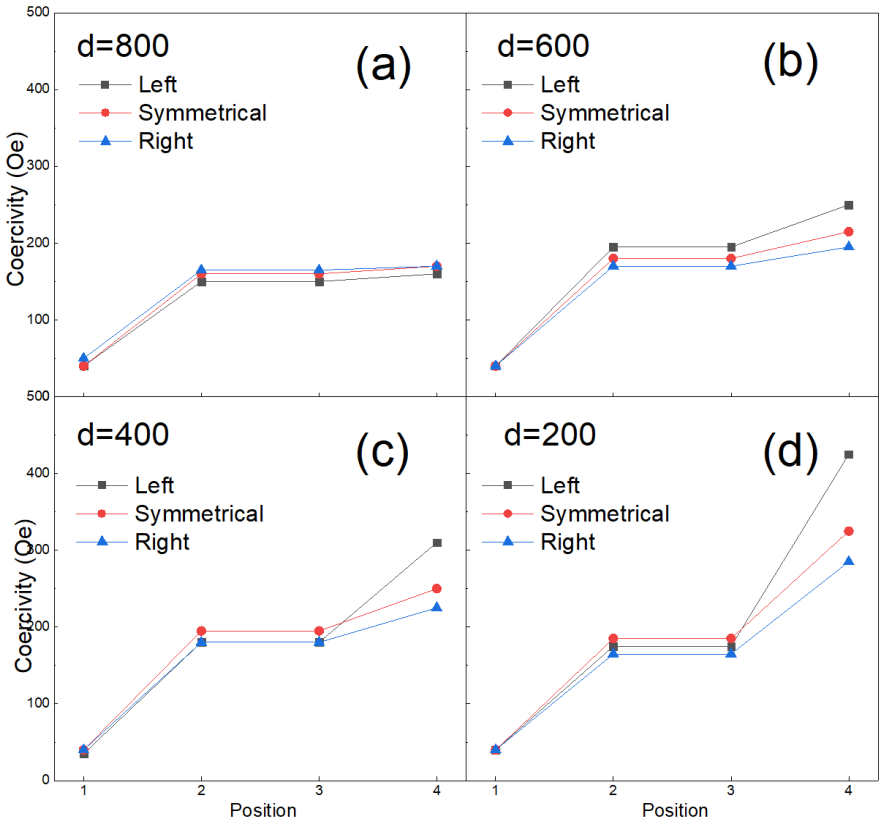

Figure 55. Coercivities variation versus positions of three types of notch geometries with different notch depth value. The lines are guide to the eyes.

4.3.2.2 Simulation for Further Increasing the Notch Depth

To enlarge the difference of the coercivity, another group of simulations was performed. Now the notch depths are around 1/10 the width of the nanowire (in the experiments, the notch depth is about 1/5 the width of the nanowire). Similarly, in order to reduce the computation for equilibrium state, a α value of 0.5 was used in the following simulation. During the simulation, because we no longer vary the notch depth d, for the convenience to depict the results, the nanowires are labeled as 'notch-geometry+α', for example, R120 denotes the Right notch geometry with, α=120°. The specific details of the notch geometries of the nanowires are shown in Table 2. As we can see from Table 2, for the Left type notch geometry, we vary the angle φ and remain the angle θ unchanged, while for the Right type notch geometry, we vary the angle θ but keep the angle φ unchanged.

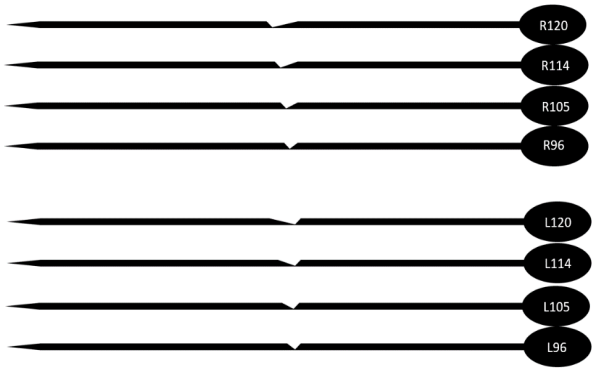

Figure 56. masks used for the simulations.

Label	α	φ	θ
L120	120°	47°	13°
L114	114°	47°	19°
L105	105°	47°	27°
L96	96°	47°	37°
R120	120°	13°	47°
R114	114°	19°	47°
R105	105°	27°	47°
R96	96°	37°	47°

Table 2. Specific parameters used during the design of the nanowires for the simulation work.

we can see from the hysteresis loops retrieved from the results shown in Figure 57, the simulations are in good accordance with the experimental protocol. The left column is the four Left type notch geometries, as we mentioned above, the Left type notches keep the angle φ (the definition of φ see the beginning of this chapter Figure 45(b)) unchanged. The simulated hysteresis loops show the coercivities at position 4 are nearly same when we only vary the other angle θ. For example, comparing the two extreme cases, the coercivity at position 4 of L120 is 513±5 Oe, while the coercivity at position 4 of L96 is 491±5 Oe, which are very close. In another word, even the geometry of the notches has change, as long as we maintain the angle φ unchanged, the coercivities will not be varied distinctly. When comes to the right column in, the Right type of the notch geometry, which is completely an opposite scenario. For the Right type geometry, the angle φ is varied from a very small angle (13°) to a relative larger one (37°) but fix the angle θ at 47°. From the simulated results, we can see that

the coercivity at position 4 is varied greatly as the angle φ changed from 13° to 37°. When comparing the coercivity of R120 (280±5 Oe) and R96 (450±5 Oe), which increased about 60%. The detailed comparison of the coercivities of different nanowires is presented in Figure 58.

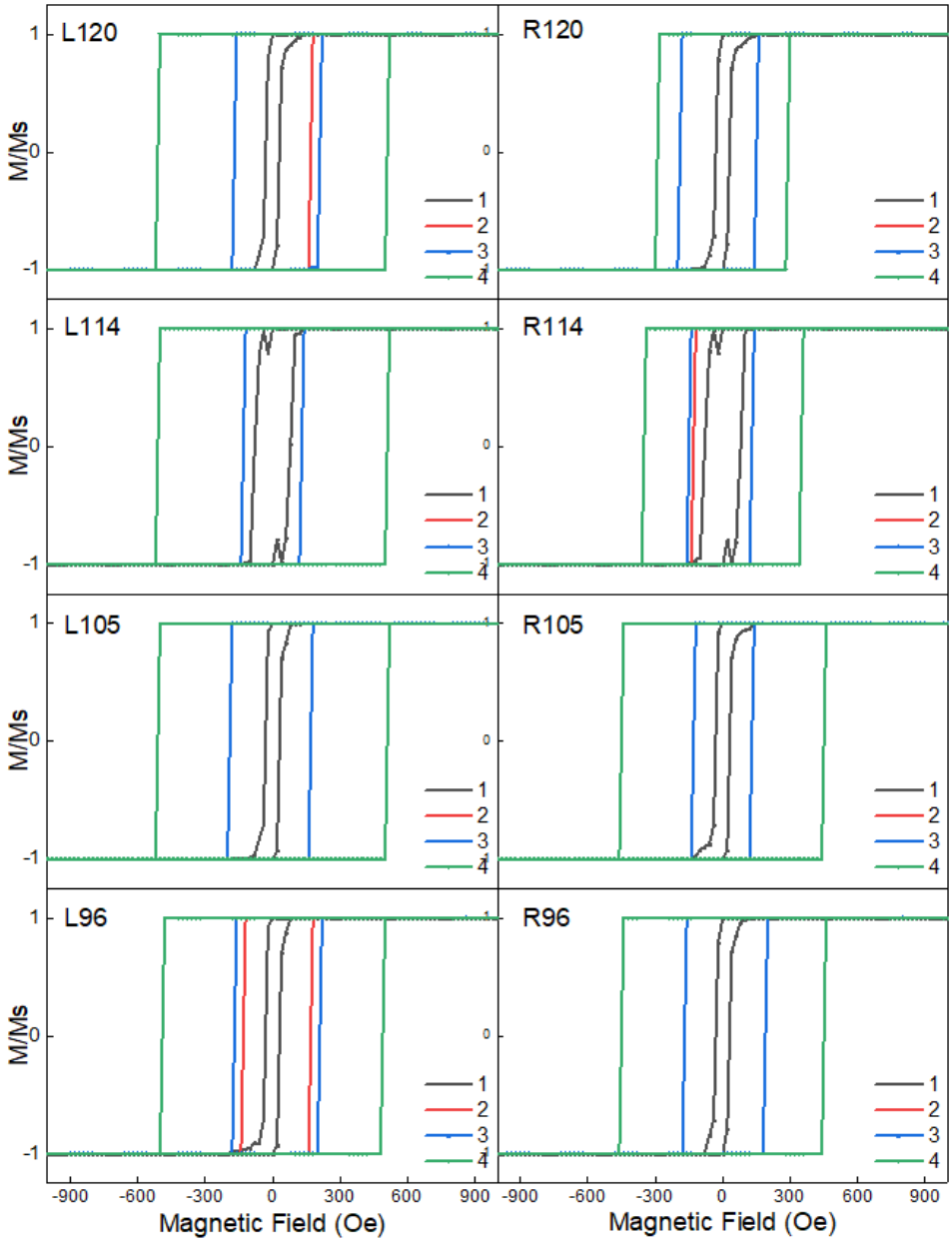

Figure 57. Magnetic Hysteresis Loops retrieved from simulation results of nanowires with different notch geometries.

Figure 58(a) gives the simulated coercivities variation versus the positions on the nanowire, the results share the same tendency as the experimental results (Figure 51).

At position 1, the same H_c values for all the nanowires, which indicate the minimum applied field needed for the nucleation of the domain wall structure, then the domain wall propagated and pinned at position 2, after the external field reaches to the critically value for depinning, the domain wall will continue propagate to position 3, which is before the notch structure, for an ideal circumstance, the values of the coercivities will not change in any points between position 2 and 3, because in the simulation, we didn't take the fabrication defects and sort of unavoidable scenario into consideration, which is slightly different with the experiments. After the domain wall gets pinned before the notch, a much higher depinning field is required to push the domain wall structure passes through the notch, completing the magnetization reversal process. The drastic difference of the depinning field at position 4 is clearly present in Figure 58 (a), the depinning fields of the Right type notch geometries vary a lot, while depinning fields of the Left type almost remain the same. Figure 58 (b) is another form of data comparison, the x-axis turns to the notch geometries. Figure 59 is the enlarged view of the notch geometry dependent coercivity of different positions at the nanowires.

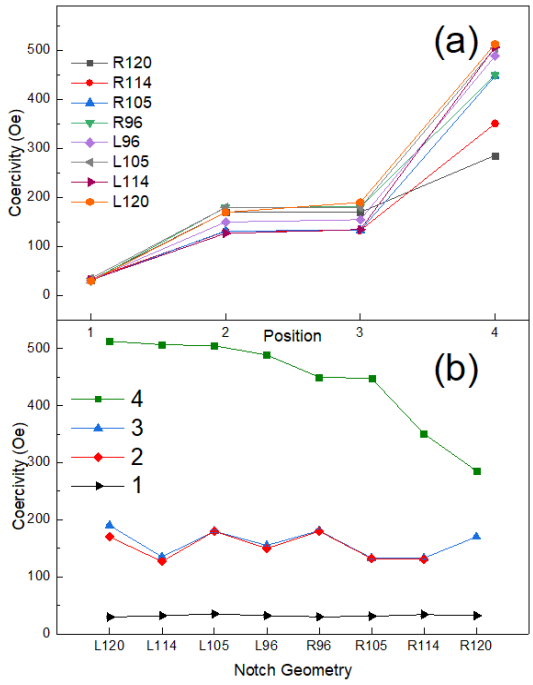

Figure 58. Simulated coercivity values of all the eight nanowires. (a) is H_c versus extraction positions, (b) is H_c versus different notch geometries.

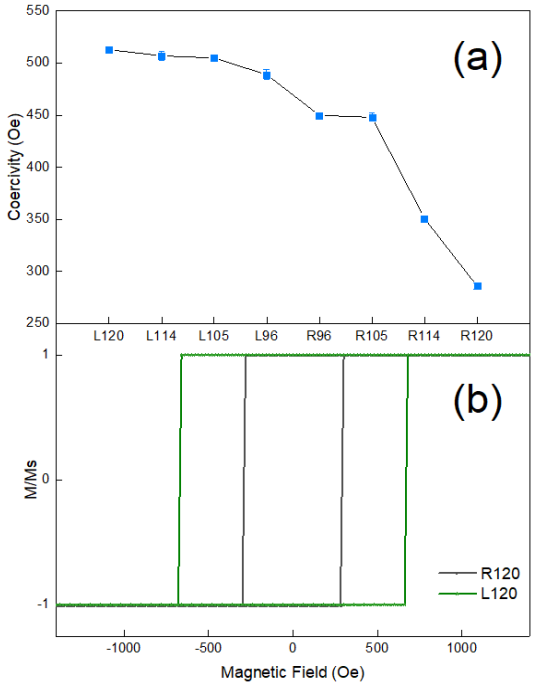

Figure 59. (a) position 4 coercivity (depinning field) variation versus notch geometries. (b) Comparison of the magnetic hysteresis loops of R120 and L120.

Here, Figure 60 gives the typical snapshots of the magnetization spin configuration, in which the left and right panels are for the different notch geometries, the left is R96 and the right is R120, respectively. Clearly, the dynamic depinning process strongly depends on the vortex chirality. During the simulation, both clockwise-vortex wall (CVW), counter-clockwise-vortex wall (CCVW) are generated equally from the nucleation pad. Considering the CCVW first, when a vortex domain wall with counter-clockwise chirality approaches to the right-side edge of the notch (see left panel), the leading edge of the vortex is seen to anchor itself to the apex of the notch, the front side of domain wall is first repelled from the right-top of the notch, because the spins of vortex at the upper side intend to align with those around the slope edge, when we keep increasing the applied field, the width of the CCVW becomes narrower and finally compressed and transformed to tail-to-tail transverse wall points downwards, allowing the wall to move further into the notch. On contrary, the CVW (see right panel), the front (left) side of the vortex wall always leans to the right-side edge of the notch, if the right-side edge of the notch is relative flat (lower angle φ), with the increasing of the applied field, the width of CVW will be compressed to the bottom edge and the right side of the notch, the front side of the wall then slightly penetrates

into the left side of the notch but still remains pinning, until the applied field is large enough, CVW will transformed to tail-to-tail transverse wall (TT-TW)points upwards. Another case, if the right-side edge of the notch is relative steep (larger angle φ), take φ=37° as an example, the angle between the front side of the CVW and the right-side edge of the notch is almost perpendicular, then the changing or vortex flipping can be expected because the wall structure is disturbed severely, the CVW cannot survive before it reaches to the notch, in this case, the TT-TW points downwards formed and pinned at the notch. The final configuration (upwards or downwards) of the TT-TW will determine the depinning field required during the magnetization reversal process [116, 118, 123], but the origin is still the interaction between the notch edge and the VW with different chiralities.

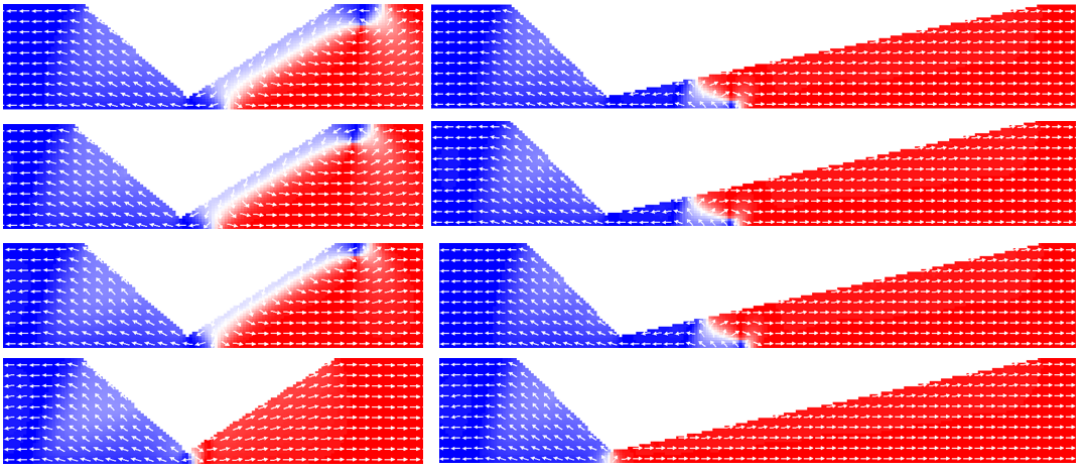

Figure 60. Snapshots of the magnetization spin configurations. The left corresponds to R96, the right corresponds to R120.

4.4 Conclusion

The understanding of interaction of the magnetic domain wall with the notch is essential for the design of reliable geometries for controlling the domain wall motion. This chapter mainly focus on the domain wall pinning and depinning behavior in Permalloy nanowires both experimentally via spatial-resolved Kerr microscopy and micromagnetic simulations. The nanowires with different notch depth and geometries were fabricated by electron beam lithography then followed by thin-film deposition via thermal evaporator. We measured hysteresis loops at four different positions at the nanowires included the before and after notch. All the hysteresis loops show a decent signal to noise ratio, which allow us to probe clearly the dependence of the chirality on the magnetization reversal process. We have demonstrated that the domain wall pinning field increases as the wire width becoming narrower. At the same time, with the increasing of the notch depth, the depinning field is more sensitive to the notch geometry. We found that when the notch depth decreases down to 200 nm, the coercive field difference of the same notch geometry but opposite orientation nanowire reaches to 82%. This phenomenon is relative weaker in the other nanowires with the notch depth greater than 200 nm. The micromagnetic simulations based on Landau-Lifshitz-Gilbert equation were induced in order to further interpret the huge coercivity difference observed in the nanowires with opposite geometry. The coercivities trend retrieved from the simulation are in good agreements with the experiments. However, the coercivity difference in the simulation is not that large as those observed in the experiments, the edge roughness could be the main reason behind the difference between the simulation and experiments. The simulated spin configuration shows the nucleation of domain wall in the nucleation pad is highly stochastic. The vortex walls with different chiralities are formed then propagated to the notch and the notch geometry, especially the slope of the edge close to the nucleation pad affects the final chirality propagation. We found that the CVW prefers the flat slope while the CCVW prefers the steep one. The study reveals an insightful approach to substantially improve our control over the domain wall motion and the pinning processes, which are important to optimize the future memory and logic devices.

Chapter 5 Damping in Perpendicularly Magnetized Co/Pt Multilayers

5.1 Introduction

In the recent decades, lots of research activities have been attracted on the spin waves and damping in magnetic structures due to the demands for increasing speed of storage of information in magnetic media and their potential applications of the next generation spintronic devices [132-135]. Spin transfer torque based magnetic random access memory (STT-MRAM) is one of the promising candidates for next generation non-volatile random access memory [136]. Currently, lots of works focuses on developing STT-MRAM in particular, the STT-MRAM utilizing magnetic tunnel junction (MTJ) with perpendicularly magnetized electrode, because they exhibit a large thermal stability factor and a very low critical current density J_c required for current-induced magnetization switching [136, 137]. Here, J_c is proportional to $\alpha M_s H_k^{eff}$ in current-induced magnetization switching, where α, M_s, H_k^{eff} are the Gilbert damping constant, saturation magnetization, and effective perpendicular magnetic anisotropy field, respectively. To achieve the application of the spintronic devices, the intrinsic magnetic damping constant of the materials is obvious one of the essential parameters. As one can see from the correlation between J_c and α mentioned above, if we want to reduce the critical current density J_c of the writing process in the STT-MRAM, a relative low value of α is required. On the other hand, high damping constants are favorable to minimize the spin switching time, and thus increase the operating speed. Therefore, besides enhancing the anisotropy constant and magneto-resistance ratio, it is also great importance to investigate the mechanism affecting the damping constant.

With the developments in spintronics and thin film magnetism from the early 1990s, there have been considerable volume of experimental work also accompany with significant new theoretical insights in order to further understand the underlying physics for the damping constant [138-141]. Those previous works include the investigation of the effects of ferromagnetic film thickness, the influences of composition on damping constant in thin-film alloys, the effects of nonmagnetic

dopants in ferromagnetic films, the combining ferromagnetic film with various nonmagnetic layers in multilayered configurations. All those works show the influence of damping constant on the applications of magnetic materials. The damped precession controls magnetization rotation and dynamical propagation of magnetic domain walls, which represent the main modes of magnetization change in ferromagnetic materials [67, 135, 138, 142-144]. The magnetic precession time is considered to govern the limiting time scale for magnetization reversal [80].

In 1996, Gaurisco *et al* firstly used an optical pump beam to excite the magnetization directly in the presence of a bias field to study the thermomagnetic writing process [145]. Later, B. Koopmans *et al* suggested all-optical real-time FMR, after observing precession in time-resolved magneto-optical Kerr effect (TR-MOKE) measurements of epitaxial Cu/Ni/Cu films following by direct optical pump induced sub-picosecond heating and demagnetization of the magnetic materials [41, 42]. Femtosecond laser becomes an intriguing possibility of probing a magnetic system on a time scale that is equivalent to the exchange interaction, which is responsible for the existence of magnetic order, and this time scale is much faster than the time scale of spin-orbit interaction (1-10 Picosecond) and magnetic precession (100-1000 Picosecond) [29]. Compared to the ferromagnetic resonance (FMR), this photo-induced processional spin dynamics is more sensitive to multi-mode spin waves since FMR selection rules allow only the excitations with a net magnetic moment [42, 146]. More importantly, all-optical pump probe measurements can determine Gilbert damping constant α from the phenomenological fitting curve [144, 147, 148].

Since damping constant α is proportional to ζ^2/W, where ζ^2 is the spin-orbit interaction energy and W is the d-band width [149], and Gilbert damping originates intrinsically from quantum mechanical electron transition mediated by spin-orbit interaction [150, 151]. At the same time, the perpendicular magnetization anisotropy (PMA) also originates from the spin-orbit interaction and broken symmetry. Theoretically, PMA is roughly proportional to ζ^2/W [152]. These theories imply that Gilbert damping trends to be stronger in materials with high PMA and there might be a linear correlation between them. Recently, Gilbert damping in [Co/Pt] films with high PMA was studied by TR-MOKE [153, 154], they found that the value of α increased with increasing stacking number while in contrast PMA decreased. In

addition, the value of α deduced from domain wall motion in Pt/Co/Pt films were found to be independent of Co layer thickness although PMA increased with decreasing thickness. Overall, the relationship between Gilbert damping and PMA remains unresolved. To further understand the Gilbert damping mechanism in magnetic materials with large PMA, a more systematic study is required to reveal the nature of this correlation. This chapter emphasizes on a systematic investigation of both intrinsic and extrinsic Gilbert damping in [Co/Pt] multilayers, by applying an all-optical approach to induce precession in [Co/Pt] multilayers and the variation of precession frequency. The damping constant as a function of applied external field and the number of [Co/Pt] stack repeats has been explored.

5.2 Sample Growth and Experimental Setup

The [Co/Pt] multilayer structures were supplied by our collaborators from the Chinese Academy of Science. The samples were grown by dc magnetron sputtering and deposited on naturally oxidized Silicon substrate at room temperature. The entire processes were performed in the clean room to prevent the sample from contaminations. The base pressure of the sputtering system was 4×10^{-5} Pa and the Argon pressure was controlled as 0.5 Pa during the sputtering. The sputtering rates for Co and Pt were 0.43 Å/s and 0.55 Å/s respectively, a Ta layer with 5 nm was used as a buffering layer between the substrate and the Pt layer, the sputtering rate for Ta was 0.98 Å/s, the purity is 99.9% for all targets. Each [Co/Pt] layer will be repeated for a certain time during the fabrication of the samples, this is for the investigation of the layer dependence of the Gilbert damping constant α. The structure of the samples is Si/Ta (5)/Pt (2)/ [Co (0.4)/Pt (0.7)]x/Pt (2.3), where x denotes the layer repeats number, and x varies from 4 to 6. Figure 61 shows a schematic diagram of the samples. The values in parentheses represent the layer thicknesses in nanometer. The exact composition of the alloys was confirmed by Prof. Jiangwang Cai from the Institute of Physics, Chinese Academy of Science.

Our Co/Pt multilayers show PMA. The Pt layer is magnetically polarized by Co. The Kerr rotation of Co/Pt is very large due to the polarization of Pt [155]. Figure 63 shows that varying the Co thickness in Co/Pt multilayers engineers the Curie Temperature of the samples drastically. Clearly, decreasing the thickness of Co leads to a reduction of T_c, which is attributed to the intermixing of Co and Pt that form a solid solution Tc [156, 157]. In our experiments, the Co/Pt multilayers studied for the AOS are much thinner, only few repetitions of the Co/Pt layer. Therefore, the Curie temperature of our samples are expected to be much lower than the data presented in Figure 63.

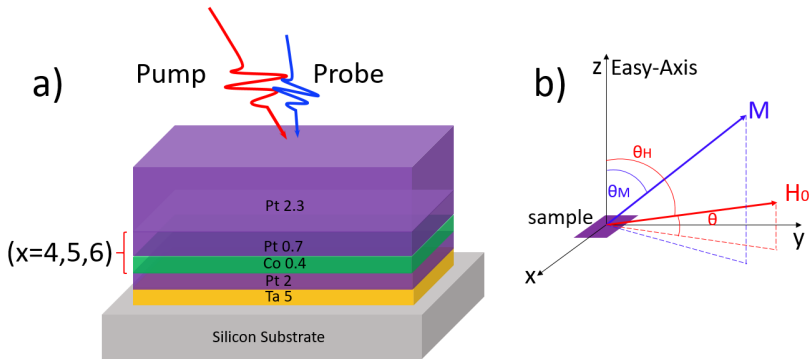

Figure 61. (a) schematic diagram of the [Co/Pt] multilayer system, the [Pt 0.7 nm/Co 0.4 nm]x layer (red braces part) was repeated from 4 to 6 times. The digits are the thickness of each layer, the unit is nanometre. (b) an illustration of the angles θ, θ_H, θ_M. Vector M and H_0 denote the magnetization and external magnetic field, respectively.

The experimental setup diagram of our TR-MOKE measurements is shown in Figure 62.

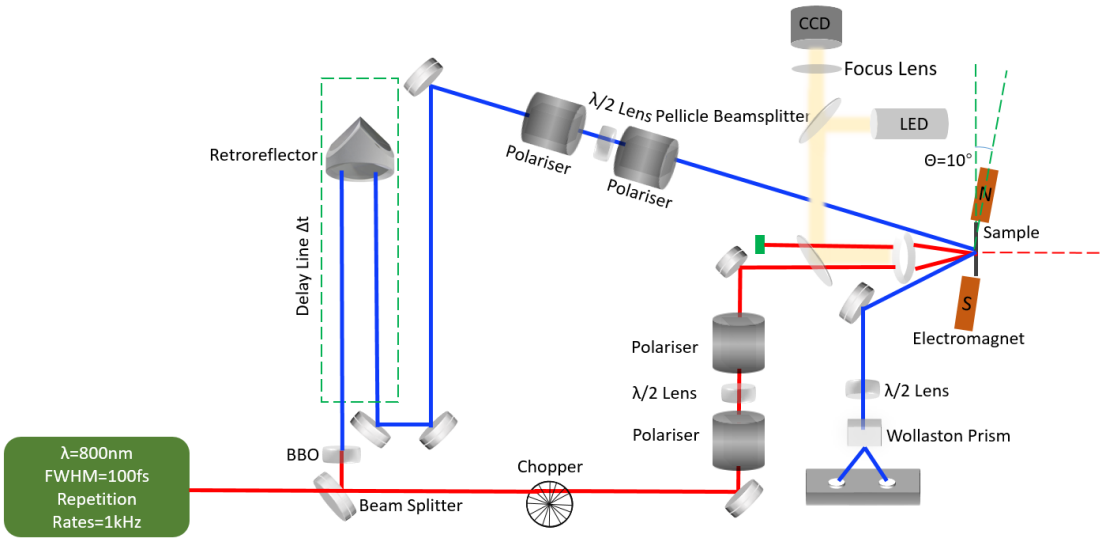

Figure 62. Experimental setup for the time resolved all-optical pump and probe measurement technique. The red solid line indicates the pump laser beam and the blue soli line indicates the probe laser beam. The red dash line indicates the easy axis of the sample. An imaging light path is used to observe the sample surface directly to check the overlap of the pump and probe beam. The laser power is 15 mW during all the experiments (7.63 mJ/cm^2).

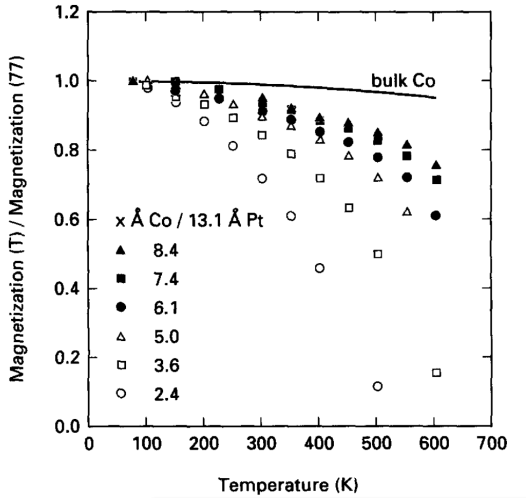

Figure 63. Temperature dependence of the magnetization of Co/Pt multilayers (60 bilayers) with varying Co thicknesses [156].

The experiments were conducted in York-Nanjing Joint Center, Nanjing University, China via Coherent Libra laser system. The laser source used in our setup is a mode-locked amplified Ti: Sapphire laser to emit pulses (800 nm) with a duration of ~60 fs at repetition frequency of 1000 Hz. The p-polarized pump beam (red line), which is modulated by an optical chopper at a frequency of 333 Hz as reference for a lock-in amplifier, is obliquely incident onto the sample surface. The spot size of the pump beam is around 500 μm in diameter. The s-polarized probe beam (blue line) with 400 nm wavelength is generated through a beta Barium Borate (BBO) crystal so that the probe beam can be distinct from the pump beam frequency to avoid the signal interference. Prior to reaching the sample, the probe beam traversed through the optical delay line, which enabled mapping the time axis and in particular the out of plane (m_z) component of the magnetization. The probe beam is incident onto the excited spot at an angle of around 6° with respect to the sample normal and the beam spot size is around 200 μm. An optical bridge detector is used to measure the Kerr signal. During the measurements, a varying external magnetic field up to about 13 kOe is applied at an angle of θ= 10° away from the sample plane (Therefore, 80° from the magnetic easy-axis of the [Co/Pt] samples). The LED light path is for the illumination of the sample surface, the reflected LED light are focused onto the CCD camera and form an image of the sample surface. Therefore, by blocking and unblocking the probe beam line, the overlap of the pump and probe beam spots can be checked directly. All measurements were performed at room temperature.

5.3 TR-MOKE Results

The TR-MOKE measurements for all the three [Co/Pt] multilayer samples with different stack repeats number are performed under a fixed pump fluence of 7.63 mJ/cm^2. Generally, the pump fluence is chosen to be high enough to trigger photon-induced magnetization precession motion, but at the same time avoid fully demagnetizing the sample magnetization. It is still under debate that how does the ultrafast pulse laser modulates the damping of magnetization dynamics [140]. Several groups have reported the effect of the pump fluence on the damping constants and other dynamic parameters such as the processional frequency and the relaxation time. Both increase [158-160] and decrease [161] of damping constants as the increasing of pump fluence have been reported in the previous works. This is an interesting topic, which is directly related to the all-optical magnetization switching. An external field is applied to saturate the sample magnetization close to its magnetic hard axis in order to trigger the magnetization precession under laser excitation. Studies have been performed on the dependence of the angle of the applied external field (θ) on the photon-induced precession motion. For example, S. P. Parkin *et al* found that if the magnetization is not dragged away from its magnetic easy axis far enough, the resultant torque generated by the optical pump pulse will be insufficient to initiate reasonable precessions [138]. The amplitude of the external field need to be sufficient to saturated the sample magnetization otherwise coherent magnetization precession may not be triggered due to a breakdown in to magnetic domains [162]. In the following experiments, the external magnetic field orientation, θ, is set to 10°.

The time-resolve Kerr rotation signals are measured as a function of the applied external field, all the three samples with different [Co/Pt] layer repeats number are plotted from Figure 65 to Figure 70. [Co/Pt] with 4 repetition is presented in Figure 65 and Figure 66. [Co/Pt] with 5 repetition in Figure 67 and Figure 68, and [Co/Pt] with 6 repetition in Figure 69and Figure 70. The magnetization precessions are excited and detected as the oscillatory Kerr signals. The damping of the magnetization dynamics is indicated by the decaying precession amplitude with the time delay increasing. The solid red curves show the fitting results according to the phenomenological formula, which will be discussed later.

As one can see from Figure 65 to Figure 70, before the zero time delay when the pump laser pulse hasn't arrived, the magnetization points in an equilibrium direction determined by the combination of the magnetic anisotropy field and the applied external bias field. The initial rapid decrease in magnitude of the Kerr rotation (magnetization) within 10 ps after the pump pulse excitation is associated with the ultrafast demagnetization triggered by the pump laser pulse via a photon-electron-spin interaction [28]. After the initial loss, the MOKE signals gradually recover and subsequently exhibit damped oscillatory behavior is a common feature observed in all-optical induced precessional measurements [143, 146, 161, 163]. Meanwhile, the local magnetic anisotropy is reduced due to the thermally induced magnetization fluctuations. Between 10 ps to 40 ps, the heat-induced sudden reduction in the local magnetization and anisotropy together with the external field leads to a temporal effective field along a new direction which is different from the original equilibrium. This subsequently provides a torque to the magnetization and forces it to precess around the newly established equilibrium direction. After 40 ps, when the original values of saturation magnetization and anisotropy are almost recovered, the original equilibrium direction restored and the magnetization precesses back towards its original equilibrium directions. This process takes hundreds of picoseconds and during this phase it is possible to determine both the precession frequency and the damping constant. In the Figure 65 and Figure 66, from (a) to (l) where the external field is varied from 13414±50 Oe to 2358±50 Oe, the oscillation frequency, in general, decrease as the applied external field decreasing. These confirm that the oscillations in the Kerr signals originate from spin precession in the films because the precession frequency is dependent on the total effective field. The amplitude of the precession increases as the applied external field decreases. This is because that the angle θ_H (see angle definition in Figure 61 (b)) between M and the film normal decreases and the out of plane component of magnetization becomes larger with decreasing external field. The amplitude of the detected polar Kerr rotation is proportional to the out-of-plane magnetization component. See an illustration is given in Figure 64. These field dependence in the Kerr signal are also observed in the other two samples as shown in Figure 67, Figure 68 for $[Co/Pt]_5$ and Figure 69, Figure 70 for $[Co/Pt]_6$.

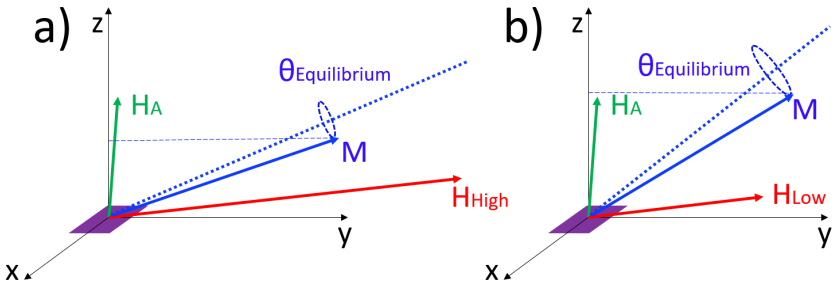

Figure 64. An illustration of the reason that amplitude is increasing as the applied external field is decreasing, (a) is high applied field case and (b) is low applied field case.

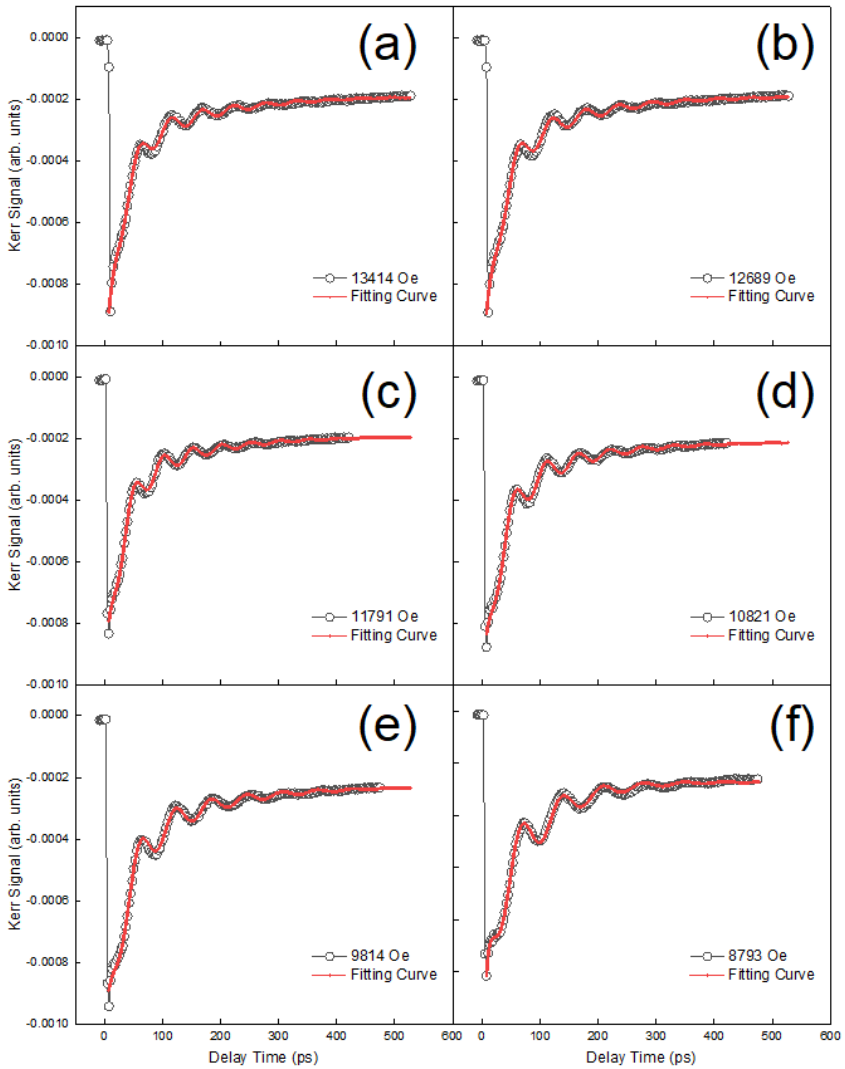

Figure 65. Time-resolved Kerr rotation signal for *[Co/Pt]$_4$* multilayer as a function of delay time after laser pulse excitation under various external bias magnetic fields. From (a) to (f) are the external bias field varies from 13414±50 Oe to 8793±50 Oe, respectively. The open circles are experimental data and the solid red curves show the fitting results according to the phenomenological function.

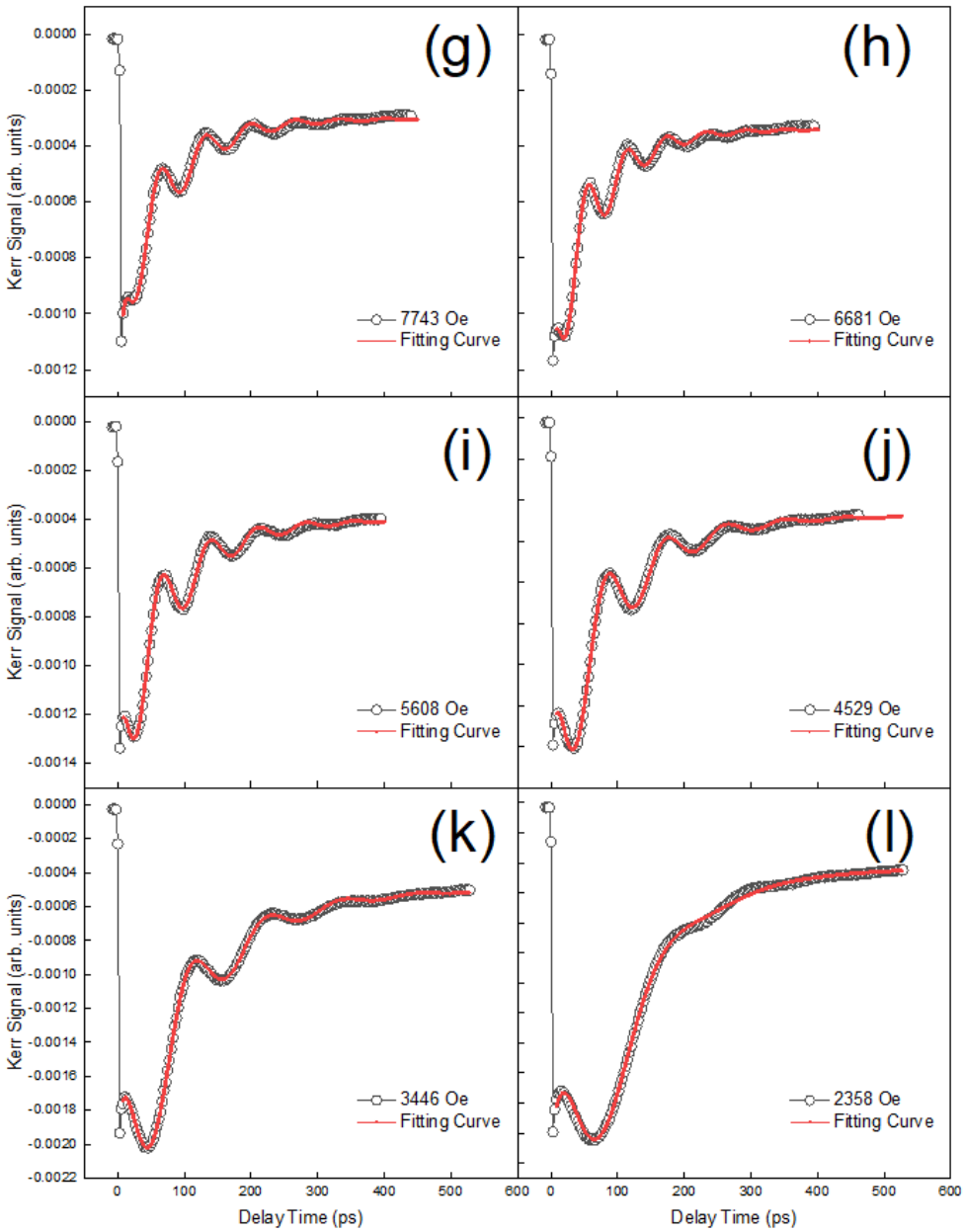

Figure 66. Time-resolved Kerr rotation signal for *[Co/Pt]$_4$* multilayer as a function of delay time after laser pulse excitation under various external bias magnetic fields. From (g) to (l) are the external bias field varies from 7743±50 Oe to 2358±50 Oe, respectively. The open circles are experimental data and the solid red curves show the fitting results according to the phenomenological function.

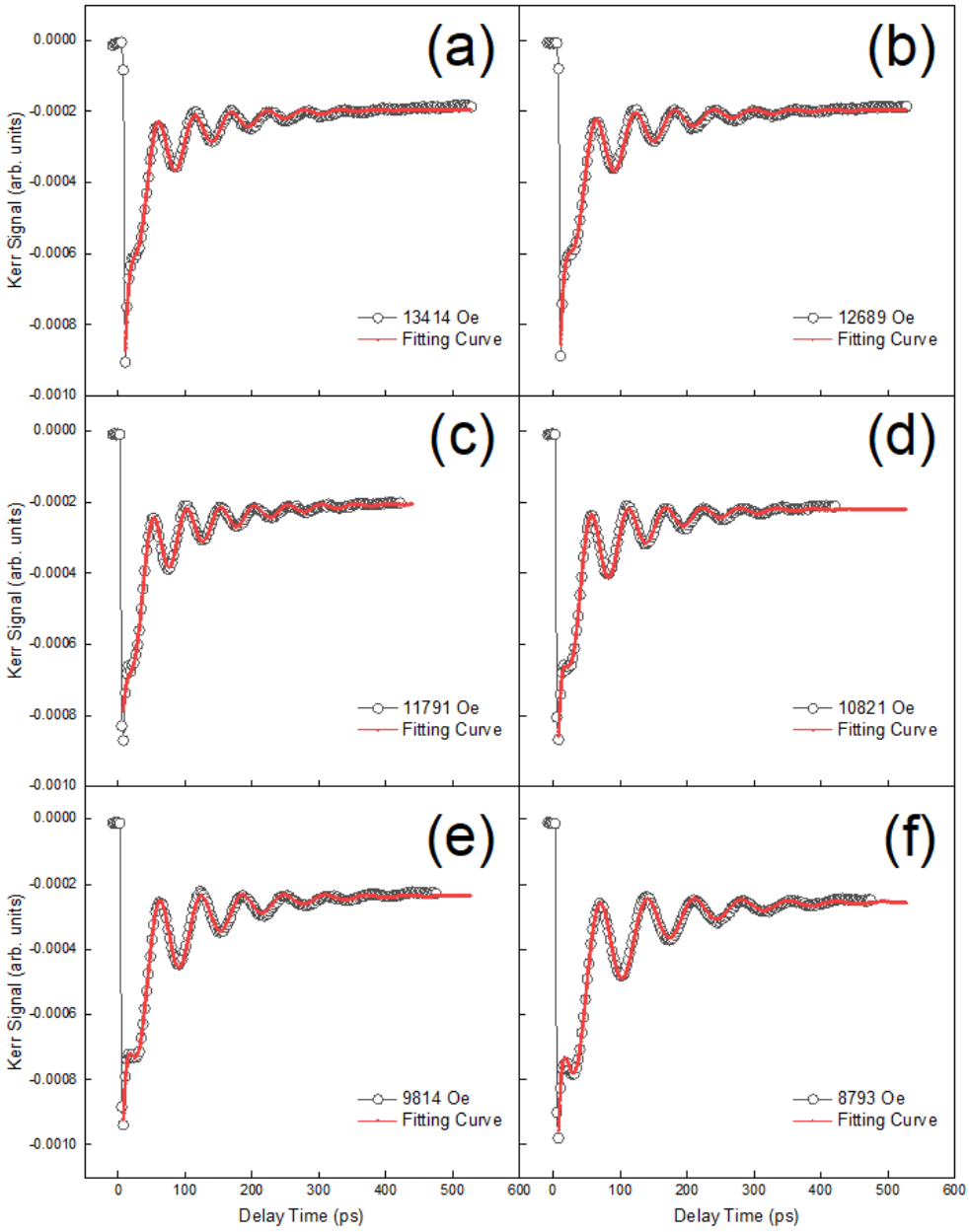

Figure 67. Time-resolved Kerr rotation signal for *[Co/Pt]$_5$* multilayer as a function of delay time after laser pulse excitation under various external bias magnetic fields. From (a) to (f) are the external bias field varies from 13414±50 Oe to 8793±50 Oe, respectively. The open circles are experimental data and the solid red curves show the fitting results according to the phenomenological function.

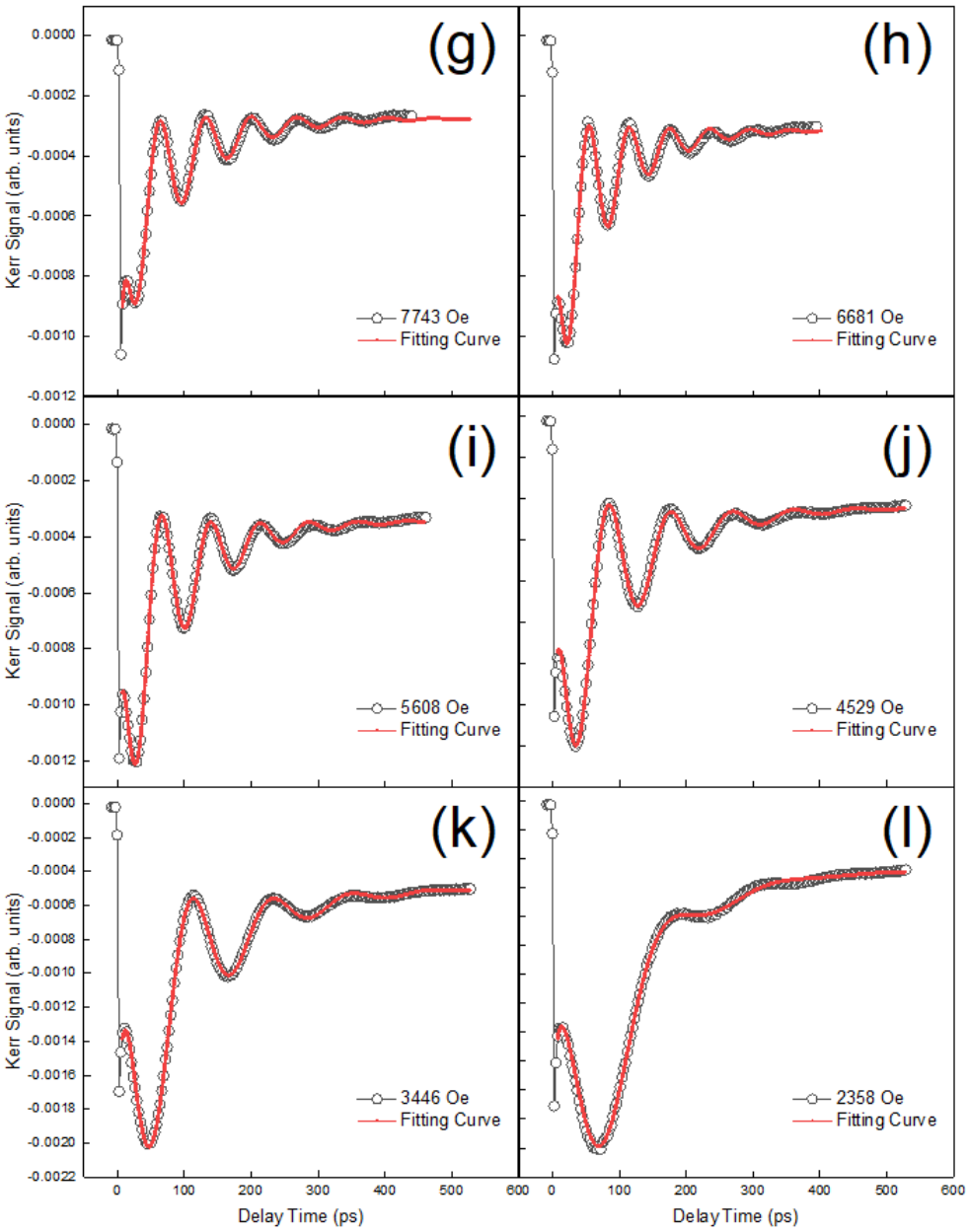

Figure 68. Time-resolved Kerr rotation signal for *[Co/Pt]$_5$* multilayer as a function of delay time after laser pulse excitation under various external bias magnetic fields. From (g) to (l) are the external bias field varies from 7743±50 Oe to 2358±50 Oe, respectively. The open circles are experimental data and the solid red curves show the fitting results according to the phenomenological function.

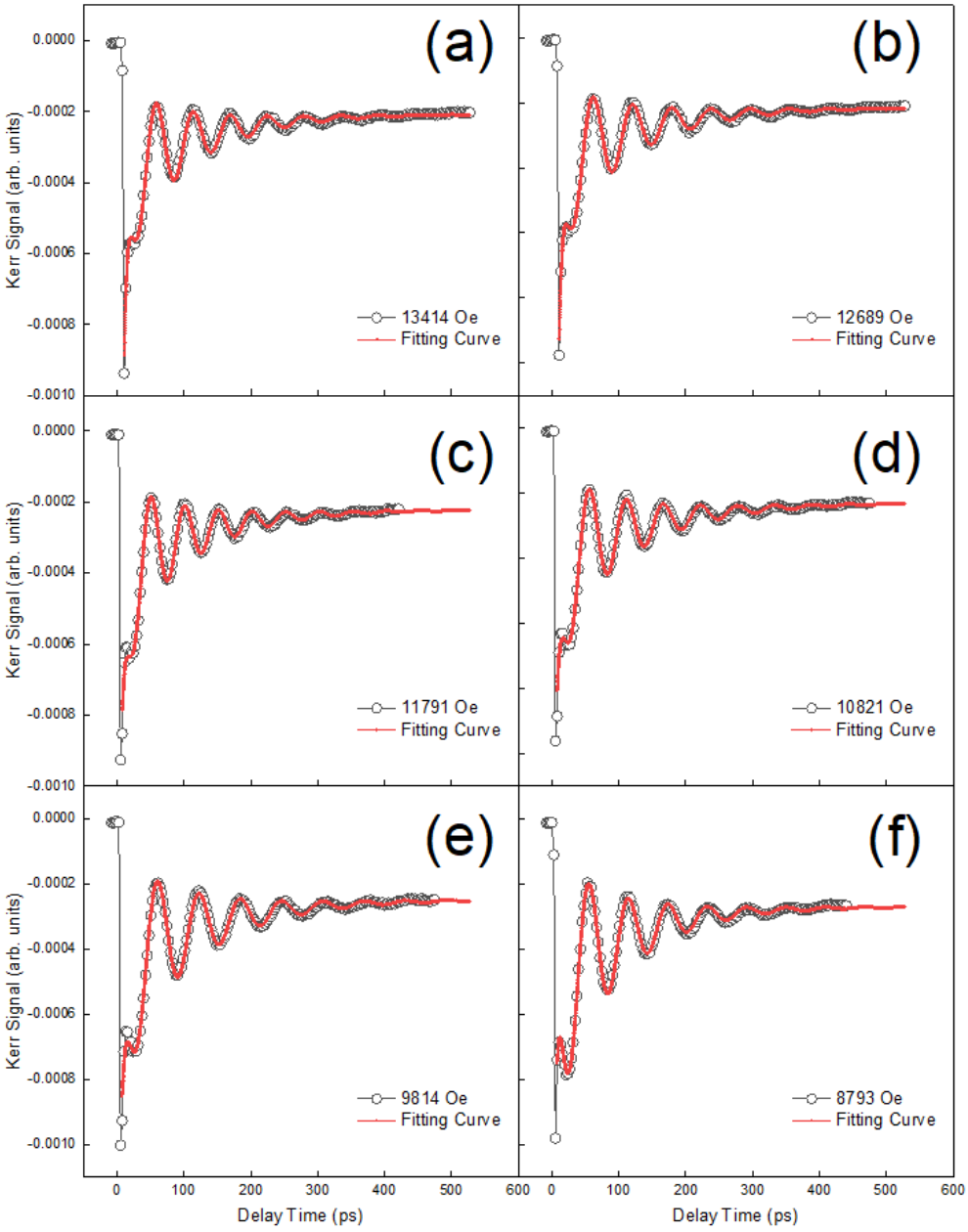

Figure 69. Time-resolved Kerr rotation signal for *[Co/Pt]$_6$* multilayer as a function of delay time after laser pulse excitation under various external bias magnetic fields. From (a) to (f) are the external bias field varies from 13414±50 Oe to 8793±50 Oe, respectively. The open circles are experimental data and the solid red curves show the fitting results according to the phenomenological function.

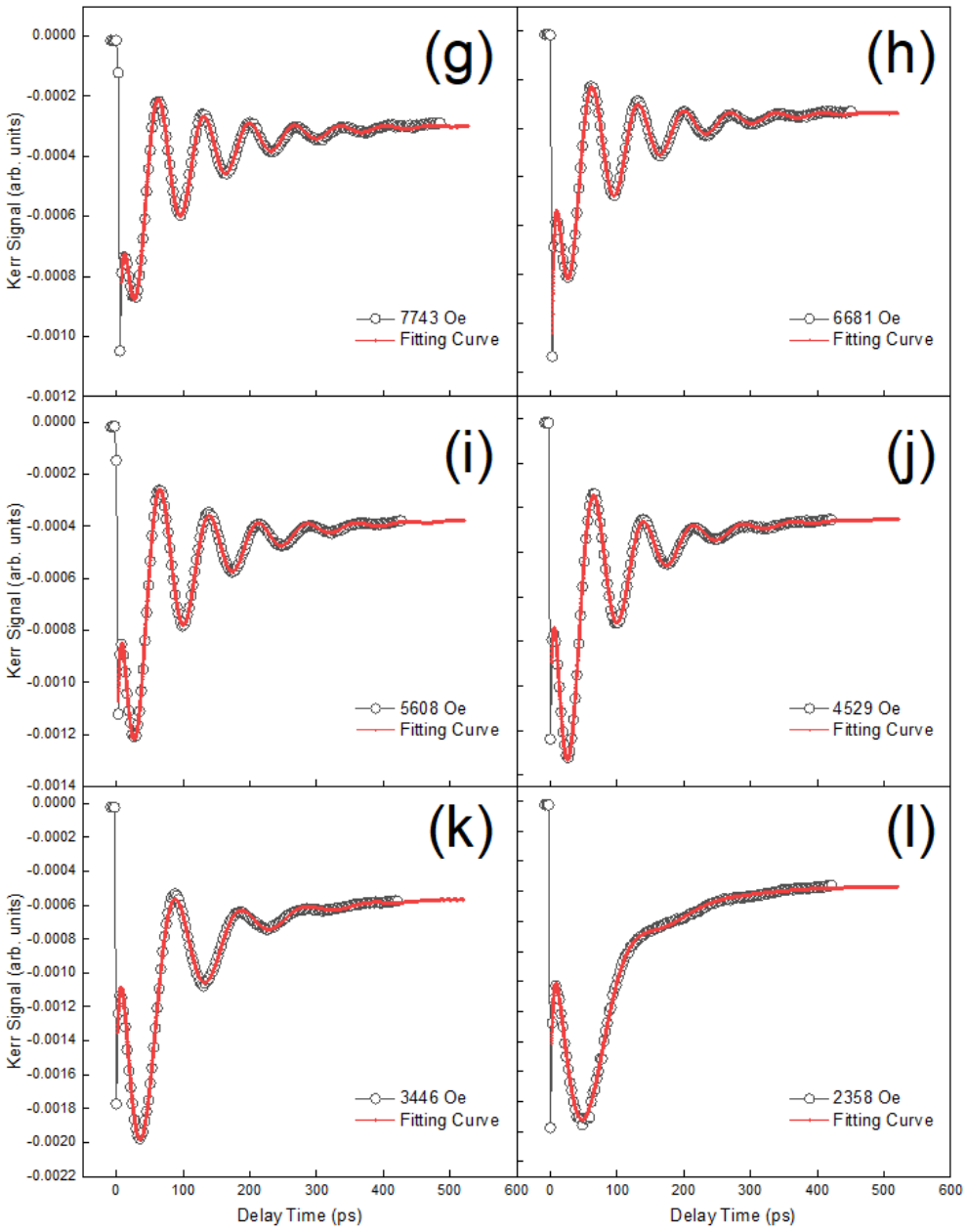

Figure 70. Time-resolved Kerr rotation signal for *[Co/Pt]$_6$* multilayer as a function of delay time after laser pulse excitation under various external bias magnetic fields. From (g) to (l) are the external bias field varies from 7743±50 Oe to 2358±50 Oe, respectively. The open circles are experimental data and the solid red curves show the fitting results according to the phenomenological function.

In order to directly compare the precession dynamics between three Co/Pt multilayer with repeat number 4, 5 and 6, their Kerr signals presented from Figure 65 to Figure 70 are plotted again in the (a), (b), and (c) panels, respectively, of a y-axis offset graph, Figure 71. By comparing the scans under the same external field between three samples, a general trend of increasing amplitude of Kerr signal as layer repeat number increases is shown, which is due to the increased thickness of magnetic layer Apart from the amplitude, the frequency and damping of the Kerr signal under the same external field is also increased as the layer repeat number increases. These trends are obvious to see when the Kerr signal under the external field of 13,414±50 Oe from the three samples are plotted together in Figure 72.

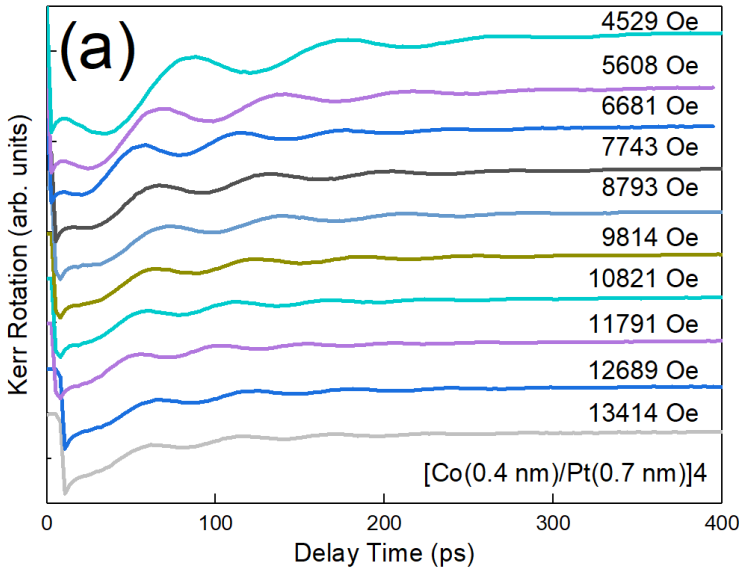

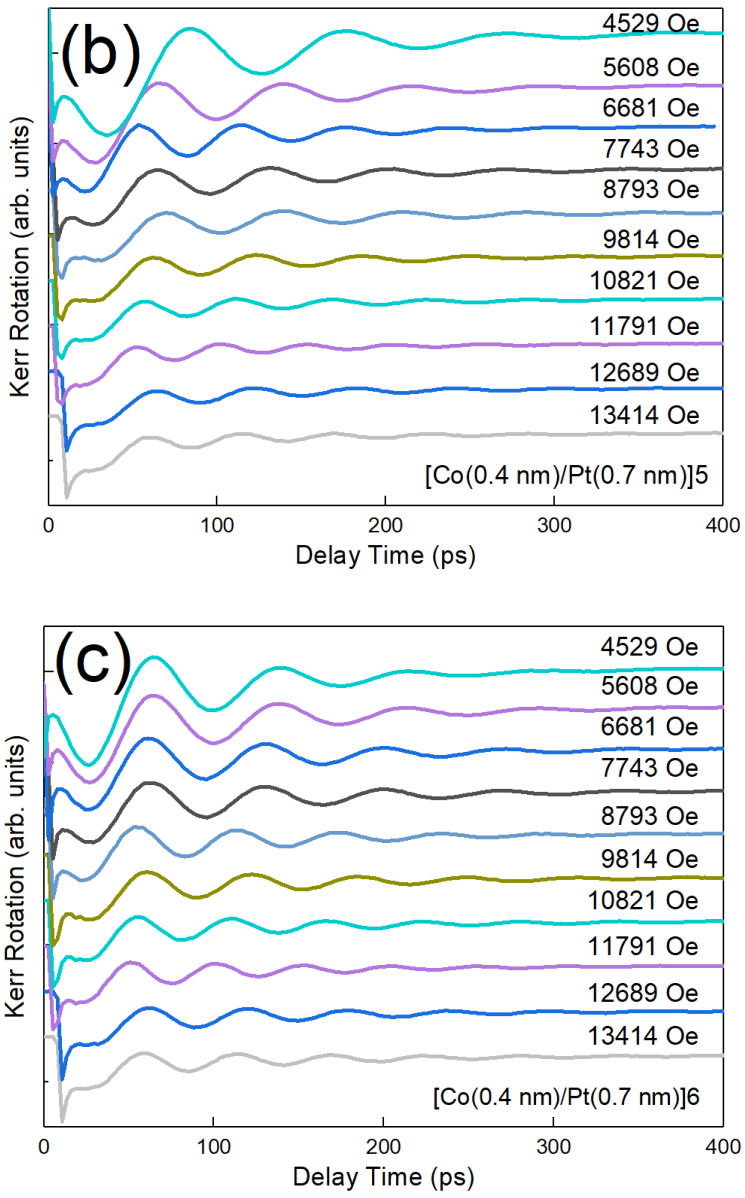

Figure 71. Time-resolved Kerr rotation signal of the three samples under 10 different external fields with θ=10°, the fluence of pump laser is 7.63 mJ/cm^2, traces are shifted for clarity. (a), (b), (c) are the three [Co/Pt]x samples with different x value, from (a) to (c) are x=4, 5, 6, respectively.

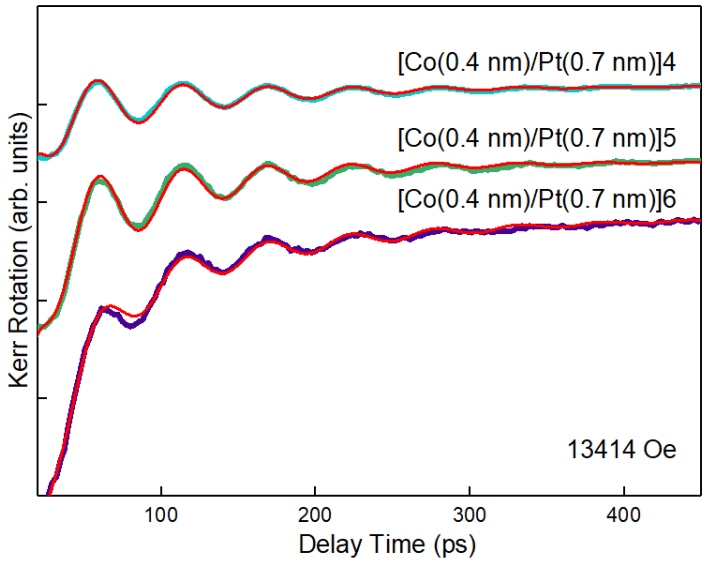

Figure 72. Kerr signals of three [Co/Pt]x samples, x=4,5,6 at the same applied external field of 13414±50 Oe. The red curves are the fitting curves.

To analyze the experimental data quantitatively, all obtained Kerr signals are fitted with the phenomenological fitting formula with double exponential decay [147, 150],

$$\Delta\theta_K \propto A(t) + Bexp\left(-\frac{t}{\tau_2}\right) sin(2\pi ft + \varphi) \qquad (5.1)$$

where B, τ, f, and φ are the initial amplitude of the magnetization precession, the relaxation time, the precession frequency, and the initial phase, respectively. The background term A(t) accounts for the demagnetization recovery [161, 164], which is generally a summation of one or two exponential decay functions. The fitted results are presented as solid red curves from Figure 65 to Figure 70. The fitting results show a good reproduction of the experimental results. Thus, the precession frequency (f) and the relaxation time (τ) of the uniform precession mode (Kittel mode) are obtained for all the three samples as a function of different applied external fields. The precession frequency obtained from the fitting phenomenological formula is presented in Figure 74. As one can see from Figure 74, the precession frequency increases as the applied external field increases. When the external field H_{ext} sits between 1266±50 Oe to 4529±50 Oe, the $[Co/Pt]_6$ shows a precession frequency always slightly higher (2±0.06 GHz) compared to the $[Co/Pt]_5$ and $[Co/Pt]_4$. The error bar of the first data point is quite large due to the weak Kerr oscillations of the results at a relative lower H_{ext}. This

tendency shows a clear layer repetition dependence. But if the H_{ext} sits higher than 5000 Oe, this tendency disappeared, and the precession frequency of the three samples with different layer repetition almost merged in the graph, which present a distinct difference. This means that the effective field for $[Co/Pt]_6$ is a bit higher than that of $[Co/Pt]_5$ and $[Co/Pt]_4$ under lower external fields. Also, comparing with $[Co/Pt]_5$ and $[Co/Pt]_4$, $[Co/Pt]_6$ show a less squared VSM loop along the sample normal indicating its anisotropy axis not quite perpendicular to the sample plane as seen in Figure 73.

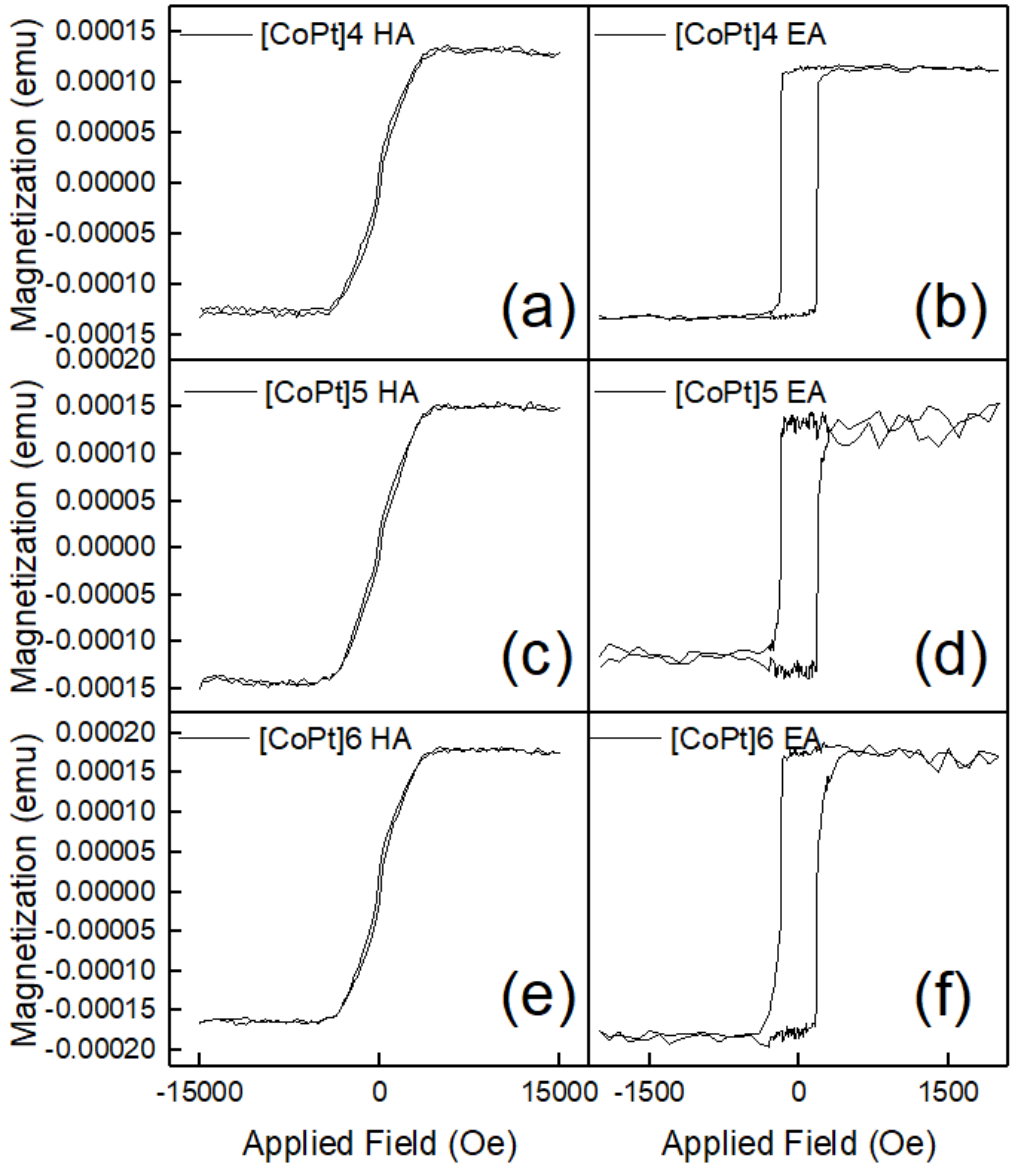

Figure 73. VSM measurements of the three samples with different layer repeats number. HA and EA denote for Hard-Axis and Easy-Axis, respectively.

Sample Information	Hard Axis Saturation Field (Oe)	Easy Axis Saturation Field (Oe)	Anisotropy Field (Oe)	Magnetization Saturation (emu/cc)
[Co (0.4 nm)/Pt (0.7 nm)]4	4915±60	343±32	4572	1830
[Co (0.4 nm)/Pt (0.7 nm)]5	5122±110	360±28	4762	2070
[Co (0.4 nm)/Pt (0.7 nm)]6	5046±180	462±20	4584	2260

Table 3. Summary of the magnetization saturation and calculated uniaxial magnetization anisotropy constant based on the VSM measurements.

The corresponded magnetization saturation M_s can be retrieved from the VSM measurements, the values are summarized in Table 3. The calculated M_s and K_u values are comparable to the reported results [165-167]. The tilting of anisotropy axis leads to a higher effective field, but this effect becomes less at high external fields. When H_{ext} reaches to 13414±50 Oe, the highest external field our experimental setup can achieve, the precession frequency of the three samples are all around 18.4±0.19 GHz. The specific data values are shown in Table 4. The retrieved values of precession frequency of the samples with different [Co/Pt] repetitions are plotted as a function of external magnetic field in Figure 74. For a quantitative analysis of the processional dynamics, the uniform precession mode (Kittel mode) around the equilibrium direction with a small tilted angle, the precession frequency can be fitted using the expression so called Kittel formula $\omega = \gamma\sqrt{H_1 H_2}$, $\omega = 2\pi f$, derived from the Landau-Lifshitz-Gilbert (LLG) equation when the magnetic damping is much smaller than 1 (see section 2.5.3, Equation 2.57). In the formula, γ is the gyromagnetic ratio, and $\gamma = g\mu_B/\hbar$, where g is the Landé g factor, μ_B is Bohr magneton and $\hbar$ is Plank constant, respectively. According to Equation 2.57, H_1 and H_2 can be written as:

$$H_1 = H_{ext}\cos(\theta_H - \theta_M) - 4\pi M_{eff}\cos 2\theta_M \quad (5.2)$$

$$H_2 = H_{ext}\cos(\theta_H - \theta_M) - 4\pi M_{eff}\cos^2\theta_M \quad (5.3)$$

Here, θ_H is the angle of the applied external field with respect to the sample normal, θ_M is the equilibrium magnetization angle. $4\pi M_{eff}$ corresponded to the effective demagnetization field, which can be evaluated as $4\pi M_{eff} = 4\pi M_s - H_\perp$ in our case, where $H_\perp = 2K_\perp/M_s$ is the perpendicular anisotropy field. The equilibrium angle θ_M

of the magnetization is determined by solving the equation of the minimum free energy [161, 168]:

$$2H_{ext}\sin(\theta_M - \theta_H) = 4\pi M_{eff}\sin 2\theta_M \quad (5.4)$$

The magnetization saturation values can be obtained from the VSM measurements. By substituting Equation 5.2 and 5.3 into Kittle formula, one can estimate the value of perpendicular anisotropy constant $K_\perp$ and the Landé g factor based on the fitting parameters. The fitting curves shown as solid red curves in Figure 75 are in good agreement with the measured frequency, and the best fitting parameters are presented in Table 5. The obtained values of perpendicular anisotropy constants $K_\perp$ are comparable to the reported results [165], and the Landé g factor for transition-metal (TM) magnetic materials is around 2 [158], which is also in good agreement with the fitting results. However, to further improve the accuracy of the fitting parameters, more measurements at different magnetic fields are necessary and the value of Landé g factor is also a main reason behind the error. One may notice that when the external field was set higher than 7000 Oe, the precession frequency shows a step-like nonlinear trend as the applied external field increased. This does not obey the Kittel formula. Additional Fourier transformation on the precession signals are also performed to examine and compare the precession frequency obtained by empirical fitting formula mentioned above. The results display the same trend as shown by the figures in a previous Ph.D thesis (Dr. X. Zou) [169], the magnetite (Fe_3O_4) films showed the similar precession frequency trend, but the explanation remains an open issue. As far as we are aware, none of the existing literatures ever report or explain such a step-like frequency trends as a function of applied external field. As mentioned earlier, the Landé g factor could affect the frequency dispersion dynamics. However, the Landé g factor is material dependent, which has nothing to do with the applied magnetic field. Besides, the fitted Landé g factor is comparable with the g factor in TM. The reasons of the step like nonlinear trend in Figure 74 could be due to magnetization dynamics, in the future work, we may vary the thickness of Co to systematically investigate the material structure and magnetization dynamics of Co/Pt multilayer.

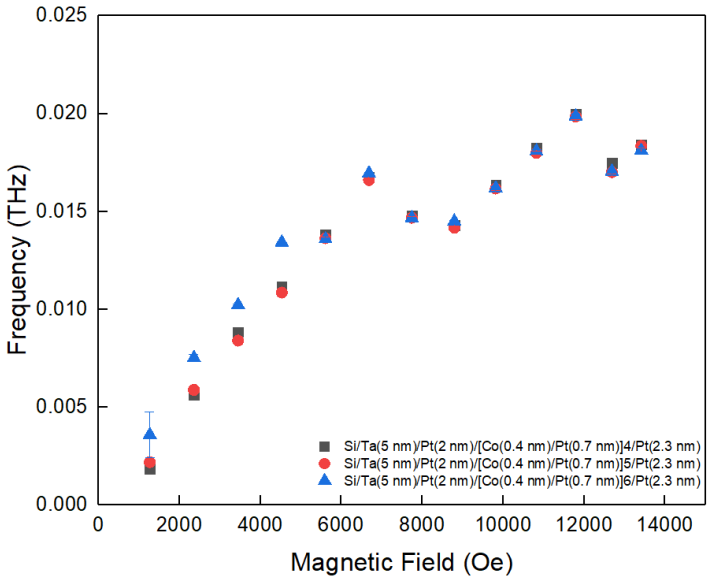

Figure 74. Precession frequency obtained via fitting phenomenological formula as a function of the external magnetic field.

External Field (Oe) H_{ext}	$[Co/Pt]_4$ Frequency (GHz)	$[Co/Pt]_5$ Frequency (GHz)	$[Co/Pt]_6$ Frequency (GHz)
13414±50	18.43±0.19	18.36±0.13	18.13±0.08
12689±50	17.49±0.17	17.01±0.11	17.05±0.07
11791±50	19.97±0.18	19.85±0.15	19.87±0.11
10821±50	18.24±0.17	17.99±0.11	18.09±0.1
9814±50	16.36±0.15	16.17±0.09	16.2±0.08
8793±50	14.29±0.13	14.17±0.07	14.5±0.05
7743±50	14.79±0.13	14.68±0.07	14.67±0.04
6681±50	16.79±0.16	16.6±0.08	16.96±0.04
5608±50	13.83±0.09	13.64±0.06	13.6±0.04
4529±50	11.18±0.06	10.86±0.03	13.43±0.04
3446±50	8.85±0.039	8.4±0.034	10.23±0.05
2358±50	5.63±0.082	5.89±0.059	7.53±0.169
1266±50	1.83±0.015	2.19±0.152	3.59±1.18

Table 4. Summary of the precession frequency of three [Co/Pt]x samples with different layer repeats number retrieved from phenomenological formula fitting.

Sample	Landé g factor	Magnetization Saturation (emu/cc)	$K_\perp$ (erg/cc)
$[Co/Pt]_4$	1.9±0.15	1830	2.17×10^7
$[Co/Pt]_5$	1.83±0.123	2070	2.75×10^7
$[Co/Pt]_6$	1.772±0.254	2260	3.11×10^7

Table 5. Obtained Landé g factors and perpendicular anisotropy constant $K_\perp$ from the fitting results.

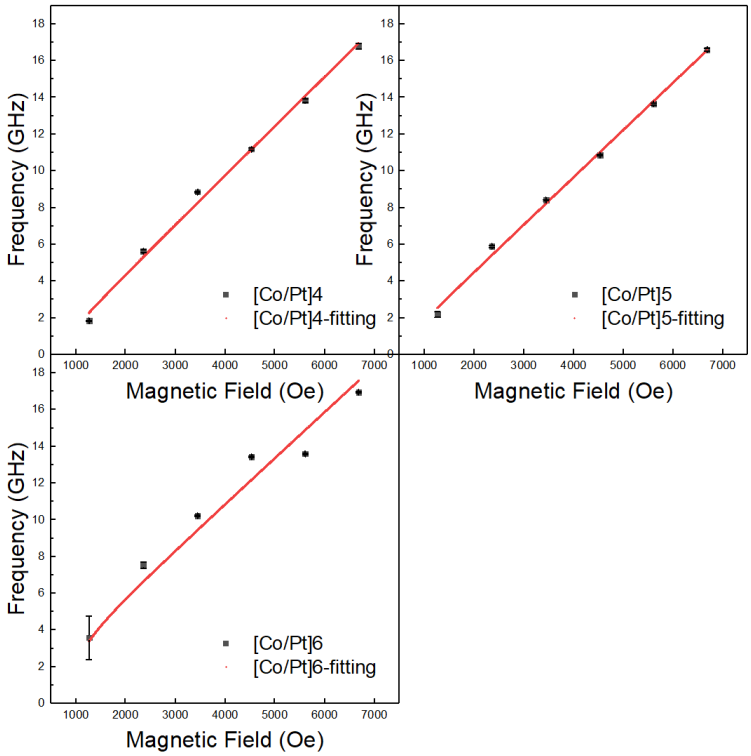

Figure 75. Precession frequency f as a function of the external applied field in three samples, the red curves are the fitting results based on the Kittle formula.

Now we examine the Gilbert damping constant. The damping constant presented here is the effective magnetic damping constant α_{eff}, which can be written as the summation of both intrinsic and extrinsic contributions,

$$\alpha_{eff} = \alpha_{int} + \alpha_{ext} \tag{5.5}$$

In the absence of demagnetization and crystalline anisotropy fields, the expression for the Gilbert damping is given by [140, 143, 170]:

$$\alpha = \frac{1}{\tau\omega} \tag{5.6}$$

Here, ω is the angular frequency, ω=2πf, and τ is the relaxation time, both obtained from the phenomenological formula fitting. The effective damping constant (α_{eff}) are obtained for all three samples and presented in Figure 76. The effective damping of all three samples decreases significantly with the increasing of external applied field. This external field dependence of the effective damping is commonly observed in other previous works [147, 170]. As shown in Equation 5.2, the α_{eff} consists of both intrinsic and extrinsic components. The extrinsic damping component mainly comes from the magnetic inhomogeneity or two-magnon scattering [67]. At low external magnetic fields, the contribution from the magnetic inhomogeneity and two-magnon scattering is significant, which leads to extrinsic damping in addition to the intrinsic damping. As the external field increases, the influence of the magnetic inhomogeneity reduces and the coherent precession dominants, which eliminates the contribution of the extrinsic component of the magnetic damping leading to a decreasing of damping [67]. Finally, the damping reaches its intrinsic value when the external field is sufficient large to maintain a coherent spin precession. The extrinsic damping at low external fields shows a layer repetition dependence with the extrinsic damping increase as the layer number increases. As the layer number increases, the inhomogeneity in the local fields and higher orders of the interface roughness increases resulting in increased extrinsic damping contribution.

To explore the dependence of intrinsic damping on the layer repetition, a zoom-in graph of the intrinsic damping at high external fields from all three samples is plotted in Figure 76 (b) together with the corresponding relaxation time as a function of external magnetic field plotted in Figure 76 (a). The $[Co/Pt]_6$ sample show a longer relaxation time compared with other two samples with less repeat number. This time scale is associated with the dissipation of energy between the lattice and surroundings, in another word, the angular momentum transfer from spin to the lattice, which decreases with the addition of the [Co/Pt] layer. Moreover, as the external field getting higher, the energy dissipation rate is getting faster. The sample with more [Co/Pt] layer repeats number has a higher effective damping constant compared to the sample has less repetition. For the external field of 13414±50 Oe, i.e, the maximum field we can achieve with the current electromagnet, the value of effective damping constant α_{eff} for $[Co/Pt]_6$ sample is 0.101±0.008, which is about 44% larger compared with the

value of α_{eff} for $[Co/Pt]_4$ sample α_{eff} =0.07±0.01. The dependence of intrinsic damping on the layer repeat number suggests an intrinsic contribution from the Co/Pt interface. The values of α_{eff} retrieved from our samples are slightly lower than the similar samples measured by others [153]. Anjan Barman *et al* reported an [Co/Pt] multilayer sample with 5 repeat number and the damping constant around 0.125, which is higher than our result of 0.096±0.005. This could be due to the highest external field they applied in their experiments was only 3.08 kOe, at such level of external applied field, a considerable contribution of extrinsic damping component should be taken into account. Another possible reason could be that the thickness of the capping layer (Pt) of their sample is thinner than ours. The increasing of the Pt layer thickness might enhance the damping due to spin-pump effect. The electronic structure at the interface is the key for the spin pumping. Electrons in the conduction band coupled with the exchanged split d band allows the spin current transport from the ferromagnetic layer to non-magnetic layer through interface. The transferred spin current induced by the magnetization dynamics will dissipate via SOC or spin-flip. Thus, the spin-pump effect pumps the spin angular momentum adiabatically from the ferromagnetic layer into the non-magnetic layer, leading to an enhancement of the damping [171-174].

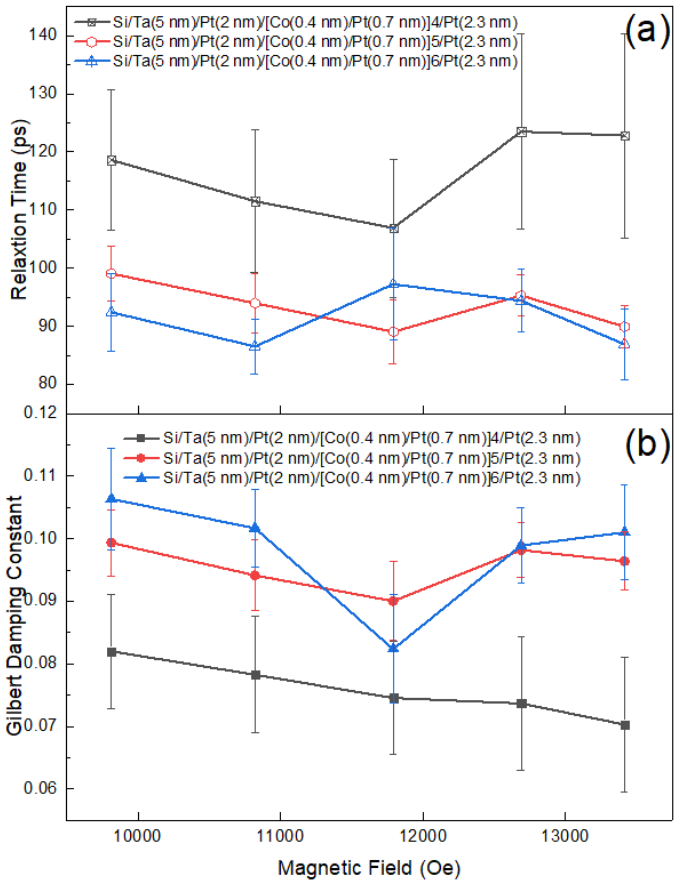

Figure 76. (a) Relaxation time τ fitting results from the empirical phenomenological formula. (b) Effective damping constant of three [Co/Pt]x samples at Higher external magnetic field $H_{ext} \geqslant 10$ kOe.

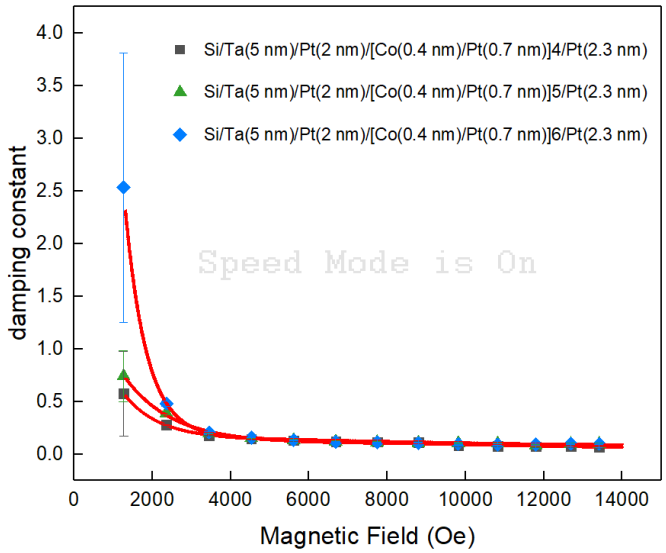

Figure 77. 12 Effective Gilbert damping constant of all three [Co/Pt]x samples as a function of the applied field. The red curves are the fitting by double exponential decay.

External Field (Oe) H_{ext}	α_{eff}		
	$[Co/Pt]_4$	$[Co/Pt]_5$	$[Co/Pt]_6$
13414±50	0.071±0.011	0.096±0.005	0.101±0.008
12689±50	0.074±0.011	0.098±0.004	0.099±0.006
11791±50	0.075±0.009	0.090±0.006	0.082±0.009
10821±50	0.079±0.009	0.094±0.006	0.102±0.006
9814±50	0.082±0.009	0.099±0.005	0.106±0.008
8793±50	0.115±0.009	0.110±0.005	0.108±0.003
7743±50	0.117±0.009	0.113±0.005	0.111±0.003
6681±50	0.122±0.010	0.122±0.005	0.120±0.003
5608±50	0.131±0.008	0.136±0.005	0.135±0.003
4529±50	0.145±0.007	0.154±0.004	0.159±0.004
3446±50	0.176±0.005	0.197±0.005	0.207±0.007
2358±50	0.230±0.010	0.389±0.013	0.480±0.026
1266±50	0.576±0.401	0.742±0.241	2.533±1.289

Table 6. Summary of the effective damping constant of the three sample with different [Co/Pt]x layers as a function of the applied external magnetic field.

5.4 Discussion and Conclusion

In this chapter, laser-induced spin dynamics of out-of-plane magnetized [Co/Pt] multilayer has been investigated by means of time resolved pump-probe magneto-optical Kerr effect measurements under different external magnetic fields. Uniform precession spin wave (Kittel Mode) is observed. The damping constants of the [Co/Pt] multilayer samples are determined by phenomenological fitting. The effective damping constant α_{eff} shows a significant external field and [Co/Pt] layer repeats number dependence. The effective damping constants decrease as the external field increased. The inhomogeneous line broadening (ILB) and other extrinsic contributions such as interfacial effects, two magnon-scattering are probably responsible for the large damping constant observed at low external magnetic fields. When the external field reached to a certain extent (in our case larger than 10 kOe), the extracted damping constants of all the three samples remain the same at around 0.07 for $[Co/Pt]_4$, 0.09 for $[Co/Pt]_5$ and 0.1 for $[Co/Pt]_6$, respectively. There is no distinct external field and frequency dependence in the variation of the damping constants. This suggest that the extrinsic influence is now relatively small, and the intrinsic damping dominates at high fields. Further enhancement in intrinsic damping with increased [Co/Pt] layer repeat number is observed at high fields. The larger intrinsic damping constant in the $[Co/Pt]_6$ sample could be due to the out-of-phase magnetization precession in different Co layers within one multilayer stack. Moreover, the increased lattice mismatching in [Co/Pt] sample with more layer repeat number could also be a source. The increased dislocation may promote electron hopping between two different sites which increases the intrinsic damping in thicker films [169, 175]. Due to all the possible intrinsic mechanisms related with spin-orbit coupling [176], the larger effective damping constant observed in $[Co/Pt]_6$ sample indicates that the spin-orbit coupling in the $[Co/Pt]_x$ systems is different. The enhancement of spin-orbit coupling contribution becomes more dominant as the film thickness increases. In order to investigate the relationship between the spin-orbit coupling with the damping dynamics, the X-ray magnetic circular dichroism (XMCD) measurements [177] can be used to detect and calculate the spin-orbit moment of different systems in future work.

Chapter 6 Helicity Dependent All-Optical Switching (HD-AOS) in Co/Pt Thin Films

6.1 Introduction

Nowadays, the manipulation of the magnetization of magnetic systems without resorting to an applied external magnetic field has received increasing attention, both for fundamental understanding the relationship of light and magnetism but also for accelerating the major scientific endeavors such as the quest for future high density and high speed write/read magnetic recording technologies [14, 178]. In 2007, Stanciu *et al*., first demonstrated that a circularly polarized femtosecond laser pulse not only demagnetizes the ferrimagnetic GdFeCo, but also reverse the magnetization state to another direction without applying any external magnetic field [44], and the final magnetization state is sensitive to the helicity of the polarized light. In another word, the left-hand (σ-) circularly polarized light will trigger one magnetization state (M-), while the right-hand (σ+) circularly polarized light will trigger another completely opposite magnetization state (M+). This novel mechanism, so called Helicity Dependent All-Optical Switching (HD-AOS) provides a way to control magnetism faster than the traditional processional switching with potentially low energy consumption [29]. Meanwhile, to explain the mechanisms behind it, lots of efforts have been put into the development of the theoretical models for HD-AOS. Some of them were based on the existence of an effective field induced by the circularly polarized light via the inverse Faraday effect (IFE) [29, 179] or by the angular momentum transfer from photons to magnetic systems [180]. Later, the models have been focused on the formation of a transient ferromagnetic state due to different demagnetization times for rare-earth and transmission-metal sublattices, and the helicity of light only plays a secondary role [45]. All-optical switching (AOS) in the ferrimagnetic GdFeCo thin film has been concluded due to a purely thermal effect, the AOS depends only on the amount of energy absorbed by the magnetic system, independent of the wavelength or helicity of the laser pulses [181-184]. More recently, the reversal of magnetization states in GdFeCo can also be achieved by laser induced ultrafast hot electrons [167, 185, 186], which provided further solid evidence of the

thermal origins of AOS observed in GdFeCo. This AOS in GdFeCo is referred as Helicity-Independent Switching (HIS).

The pioneering work of the AOS all focused on rare-earth transition-metal (RE-TM) such as GdFeCo [44, 46], TbCo [48, 49], TbFeCo [50, 51], DyCo [53] etc., as well as synthetic ferrimagnets[53]. In all those cases, this laser induced magnetization switching can only be observed in ferrimagnetic systems with two distinct sublattices that are antiferromagnetically exchange-coupled. It raises a question, whether AOS is specific to the ferrimagnetic materials? Due to the strategic significance of the rare-earth elements, discovery of alternative All-Optical Switching magnetic materials becomes one of the most pressing and important challenges. Until 2014, C-H. Lambert, et al., achieved AOS in ferromagnetic Co/Pt thin films and nanostructures [54]. More recently [187], B. Koopmans had experimentally demonstrated that both thermal single-pulse AOS as well as SHE induced domain wall motion can be combined in a Pt/Co/Gd racetrack with perpendicular magnetic anisotropy, they exploit the chiral Neél structure of the DW's for coherent and efficient motion of the optically written domains. Their work successfully combined the AOS with racetrack memory technologies. And show that the Pt/Co/Gd racetrack is an ideal candidate to facilitate the integration of AOS with spintronics.

The difference between the initial studied GdFeCo and the Co/Pt, as well as some Tb-based ferrimagnetic materials is that the AOS in the later materials are strongly helicity dependent [52, 188]. For these materials, one helicity state correspondences to one specific magnetization orientation, contrary to the Helicity Independent All-Optical Switching (HI-AOS). This phenomenon is referred as Helicity Dependent Switching (HD-AOS). It is worthy to mention that GdFeCo also show a dependence on helicity for single pulses applied to the thin film for a narrow window of laser fluence [189], and this was quantitatively explained as a results of magnetic circular dichroism (MCD) [83]. Despite of intense research being carried out on AOS, the underlying physics of HD-AOS in a wider variety of materials remain unclear and under debate, especially in terms of the roles of helicities of laser pulses [181, 189-191]. This chapter aims at exploring the role of circular polarization of laser pulses on HD-AOS by varying the degree of circular polarization.

Magnetization Manipulation	Ultrafast Demagnetization	All-Optical Helicity Independent Switching	All-Optical Helicity Dependent Switching
Light	[28]	[45, 83, 183, 192, 193]	[44, 53, 54, 194, 195]
Hot Electrons	[196, 197]	[185]	[198]

Table 7. Summary of the key literatures in the related area.

6.2 Sample Growth and Experimental setup

The Co/Pt sandwich structure samples were sputtered on Silicon substrates by our collaborators from Chinese Academy of Science. All the growth processes were performed in the clean room to prevent any contamination. The base pressure of the sputtering system was better than 4×10^{-5} pa and the Ar pressure was controlled as 0.5 pa during the sputtering. The sputtering rates for Co and Pt were 0.43 Å/s and 0.55 Å/s respectively, and a 5nm Ta was used as a buffering layer for lattice-matching between the substrate and Pt layer. The sputtering rate for Ta was 0.98 Å/s and the purity were 99.9% for all targets. The structure of the samples is Si/Ta (5 nm)/Pt (2 nm)/ [Co (x nm)/Pt (0.7 nm)]/Pt (2.3 nm), The values in parentheses represent the layer thicknesses and the thickness of Co layer was varied from 0.4 nm to 1.2 nm at a step of 0.2 nm. Figure 78 gives a schematic diagram of the samples. The exact composition of the alloys was also confirmed by Prof. Jiangwang Cai from the institute of Physics, Chinese Academy of Science.

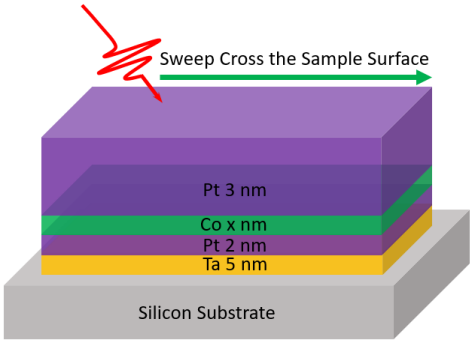

Figure 78. Schematic diagram of the samples structure.

A diagram of the experimental set-up for the all-optical magnetization switching is schematically shown in Figure 79. A LED lamp was used as the illumination source to image the magnetization state of the sample. The wavelength of the LED was 455nm, and the detailed setting of the imaging system can be found in the Chapter 4 of this thesis. The laser pulses were generated by an amplified mode-locked Ti: sapphire laser system producing Gaussian pulses at a center wavelength of 800 nm. The pulse duration FWHM was 100 fs, the repetition rate was 1 kHz. The laser pulses were adjusted from circularly polarization to linearly polarization by rotating the fast-axis of a zero-order quarter-wave plate respect to the optical axis of a linear polarizer (2nd

polarizer see Figure 79). The laser pump pulses were made collinear with the LED probe light by the golden mirror and then both lights were focused onto the sample plane by a long-work-distance objective lens with NA=0.55. The scattered LED light from the sample was then collected by the same optical objective lens and directed into a near-crossed polarizer before focused onto the CCD matrix. A combination of a linear polarizer (1st polarizer) and an optical half-wave plate in the laser beam path was used to precisely control of the laser fluence illuminated onto the samples. The fluence of the laser pulses was estimated from the laser power measured by a power meter. Due to a relative fluctuation in magnitude from pulse to pulse, which varies typically between 1%~2%, the pulse power was averaged over a period of several seconds. The ellipticity of the final pulses reached to the sample was examined by putting an analyzer into the beam path after the triangle golden coated mirror in Figure 79. The elliptical ratio was obtained by rotating the analyzer and recording the maximum and minimum transmitted laser power.

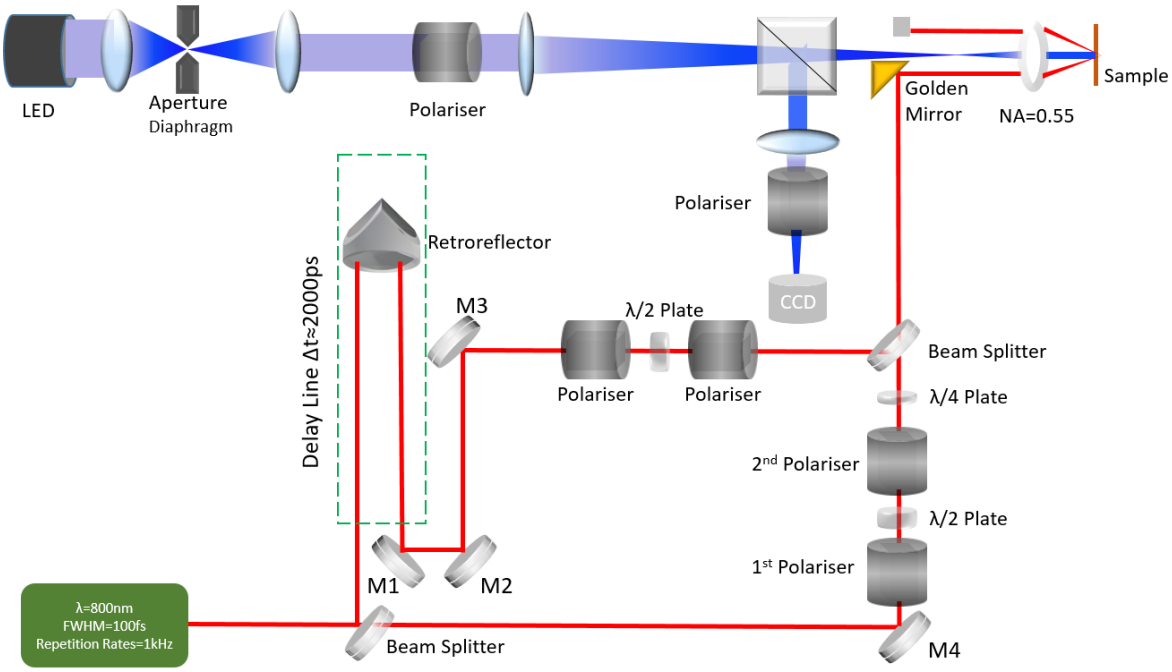

Figure 79. Schematic diagram of the set-up for All-Optical Helicity Dependent Switching experiments, the blue corresponds to the LED beam path, while the red corresponds to the laser beam path.

6.3 Kerr Imaging, Polar MORK and VSM Measurements

The static magnetic properties of Co/Pt thin films were characterized via polar MOKE loops, VSM loops, and wide-filed MOKE (Magneto-Optical Kerr Effect) imaging. The magnetic hysteresis loops and magnetization saturation were measured by a VSM at ambient temperature with magnetic fields applied both along the out-of-plane and in-plane of the sample as plotted in Figure 80. A maximum external magnetic field of 15,000 Oe was applied to make sure the samples were fully saturated. The magnetic domain structure of each sample at its remanence state was also captured by a wide-field MOKE imaging system and presented as the inserts in Figure 80. The '⊙' and '⊗' in the MOKE images denote two different magnetic states, '⊙' corresponds to the white domain, which the magnetization state pointing into the plane, while '⊗' corresponds to the black domain, which the magnetization state pointing out of the plane.

The reason why a piece of magnetic material breaks into multi-domains, rather than exists in a single-domain state is to minimize its internal energy [30]. As shown in the MOKE images, the average domain size decreases as the thickness of Co increases. This is because, in the thin-film limit, the equilibrium domain size increases with decreasing film thickness in order to reduce the magnetic static energy [199].

The VSM loops has shown a strong perpendicular magnetic anisotropy of all films with a squared hysteresis loop (black dots with left-axis and bottom-axis) along the out-of-plane orientation indicating the easy axis. Besides, Polar MOKE was also taken so that we can make a comparison with the VSM measurements.

The saturation field of the hard-axis hysteresis loops (red dots with left-axis and top-axis) along the in-plane orientation varies between samples demonstrating a Co thickness dependence of the perpendicular magnetization anisotropy (UMA). The effective uniaxial anisotropy constant K_u^{eff} is determined by $K_u^{eff}=(H_k \cdot M_s)/2$, where M_s is the magnetization saturation also obtained via VSM measurements [200]. The anisotropy field is 694 Oe when the Co thickness is only 0.4 nm. The values of the anisotropy field H_k increases as the thickness of Co increases, and gets to a maximum of 10665 Oe when the Co thickness reaches to 0.8 nm. Then the anisotropy field begins

to decrease as the thickness of Co increases further (see summary in Table 8). In the meantime, the easy axis begins to slightly rotate from out-of-plane to in-plane as the hysteresis loop along out-of-plane orientation becomes less square in Figure 80(e).

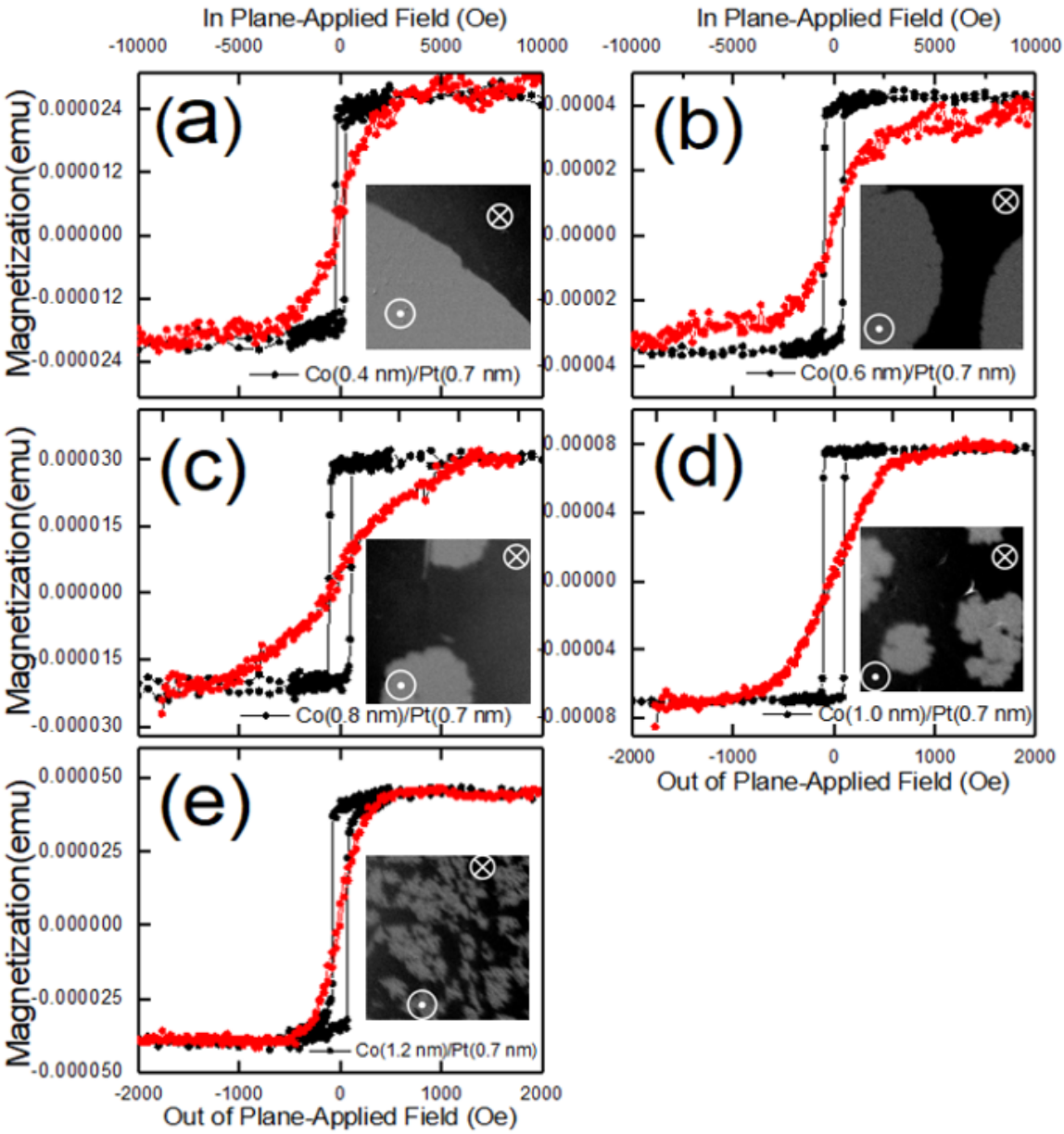

Figure 80. Magnetic hysteresis loops measured via VSM, the five samples are with different Co thickness. The black and red hysteresis loops represent easy and hard axis respectively. The inset images are the multidomain states at zero external field captured via our Kerr imaging system.

Figure 81 is the saturation magnetization retrieved from the VSM measurement, the effective magnetization saturation was calculated by M_s=M/V, where M is the

saturation moment from the easy axis loop and V is the volume of the sample. It is worthy to mention that when calculating the volumes of the samples, I considered two different scenarios: with the Pt layer and without the Pt layers (see Figure 81), I found that only when treating Co/Pt as a ferromagnetic single layer and the magnetization contributed only by the Co atoms, then the calculated effective magnetization saturation will match with the values reported in other literatures [165, 201]. The saturation magnetization of Co/Pt samples was found varies from 1512 emu/cc, 1655 emu/cc, 1722 emu/cc, 1904 emu/cc and 2070 emu/cc for Co thickness = 0.4 nm, 0.6 nm, 0.8 nm,1 nm and 1.2 nm, respectively. The calculated anisotropy constants (K_u^{eff}) are also in good agreement with previous works reported by other researchers [192, 201, 202].

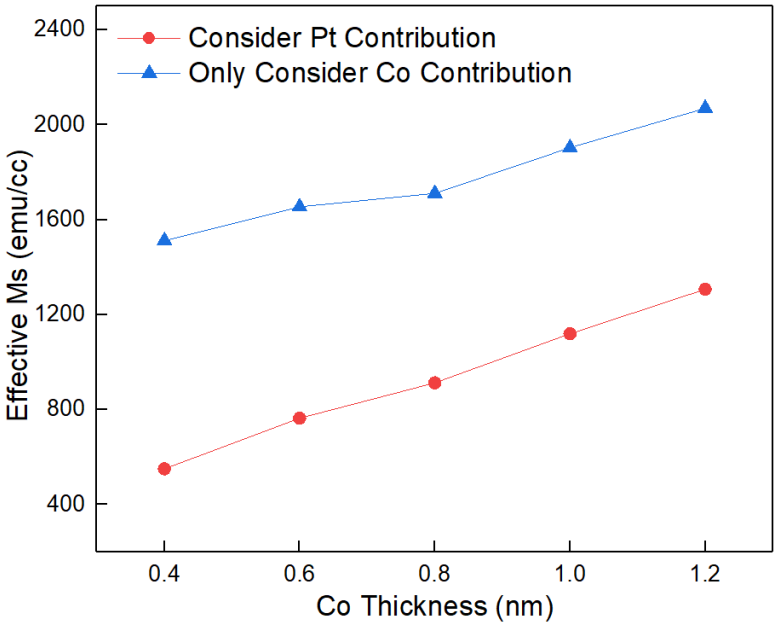

Figure 81. Effective magnetization saturation of five samples measured at 300 K as a function of different Co thickness. Two different volume modes were calculated in order to compare the values.

Sample Information	Hard Axis Saturation Field (Oe)	Easy Axis Saturation Field (Oe)	Anisotropy Field (Oe)	K_u^{eff} (Merg/cm^3)
Co (0.4 nm)/Pt (0.7 nm)	738.59±40	43.76±2	694.83	0.52
Co (0.6 nm)/Pt (0.7 nm)	10615.63±80	97.22±2	10518.41	8.70
Co (0.8 nm)/Pt (0.7 nm)	10775.19±80	109.83±4	10665.36	9.12
Co (1.0 nm)/Pt (0.7 nm)	9275.19±70	104.79±3	9170.4	8.93
Co (1.2 nm)/Pt (0.7 nm)	511.62±10	76.42±3	435.20	0.45

Table 8. Summary of the saturation field of the hysteresis loops along both easy and hard axis, and the calculated uniaxial anisotropy constant Ku.

Figure 82 is the normalized hysteresis loops of five thin film samples with different Co thickness measured by Kerr imaging system. The relative saturation Kerr magnitude (as shown in the insert) between different samples are in good agreement with their saturation magnetization obtained from the VSM measurements. Figure 83 is the coercive fields (H_c) versus Co thickness retrieved from the hysteresis loops obtained by Polar MOKE and VSM measurements. The H_c almost doubled as the Co thickness increased from 0.4 nm to 0.6 nm and continue to rise till the thickness reaches to 0.8 nm, then decreased slightly after Co thickness reaches to 1 nm and 1.2 nm. The coercive fields retrieved from the VSM and the Polar MOKE are nearly identical.

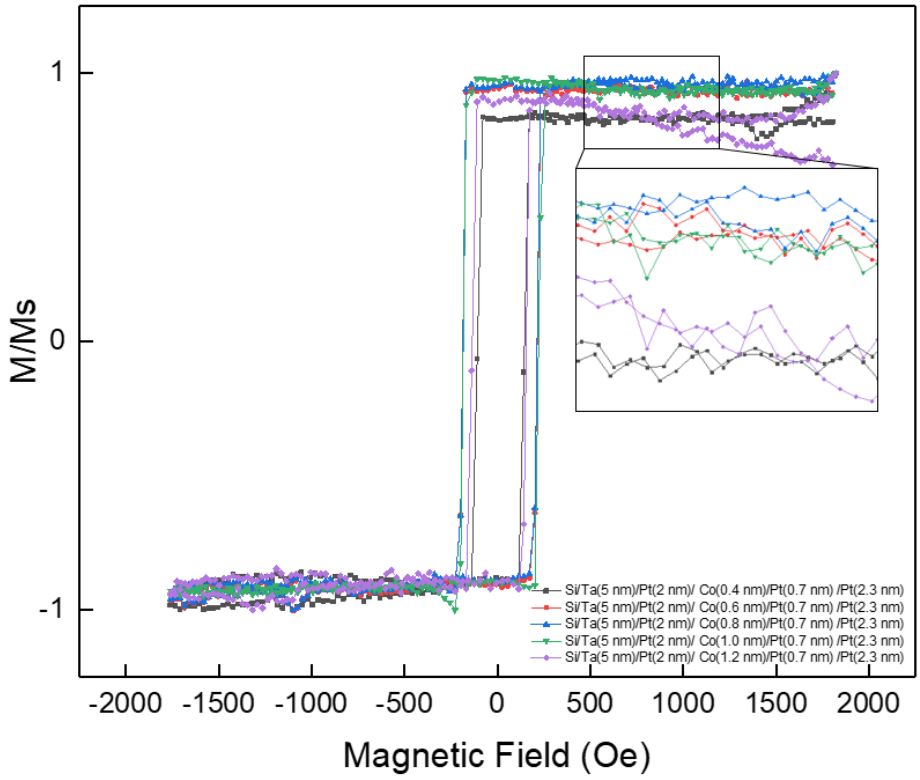

Figure 82. Normalized Hysteresis Loops of five thin film samples with different Co thickness at their easy axis, the loops were obtained from the wide field Kerr Imaging system.

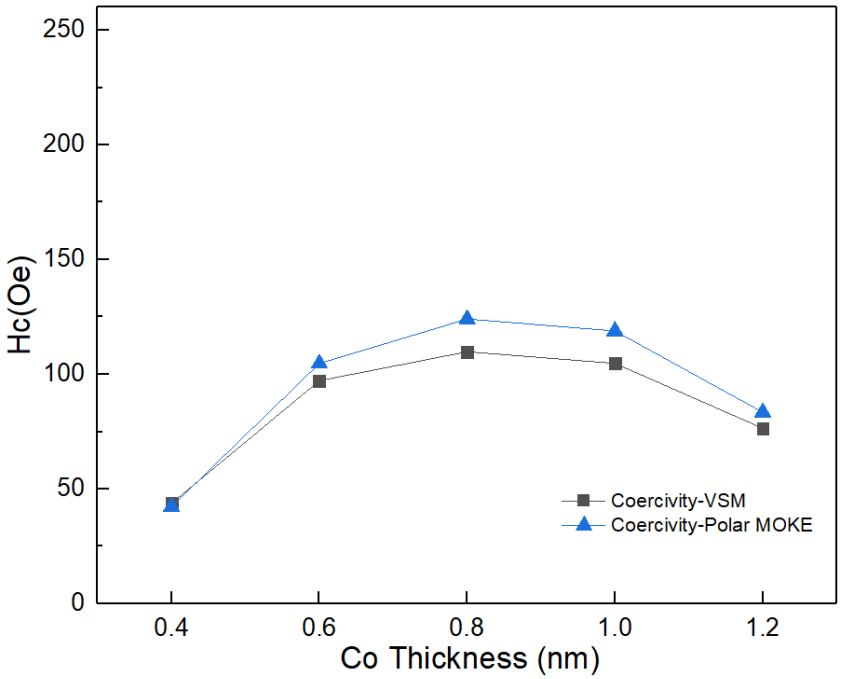

Figure 83. Coercivities of the samples with different Co thickness, retrieved by two different techniques.

6.3 Helicity Dependent All-Optical Switching: Results and Analysis

To investigate helicity dependent all-optical magnetization reversal, the final state of the sample magnetization after the laser pulses excitation was studied as a function of the laser pulse power and degree of ellipticity. The magnetization evolution in all five Co/Pt samples with different Co thickness were recorded by taking magnetic contrast images using a wide-field MOKE imaging technique as shown in Figure 79. During the experiments, the samples were initially magnetized up (⊙ white domain) and down (⊗ black domain) and then leave at its remnant state by applying an external magnetic field to create a multi-domain state (see the inserts in Figure 80) before laser illumination. Then the multi-domain state got modified after the laser beam swiping across the sample. During the experiments, the laser beam was incident. The degree of ellipticity of the laser beam was adjusted from right-circular (+45°) to linear (0°) and to left-circular (-45°) polarization by changing the angle between the fast axis of the quarter-wave plate and the optical axis of the half-wave plate in steps of 5° as illustrated in Figure 84. The optical axis of the linear polariser is set along 0°.

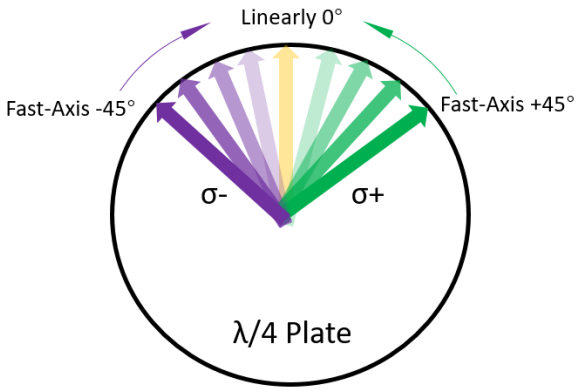

Figure 84. Schematic diagram of how to change the degree of ellipticity of laser pulse via adjusting the angle of a λ/4 plate. The optical axis of the linear polariser is set along 0°.

By swiping the laser pulse with a particular degree of ellipticity horizontally over a region of the sample with defined initial magnetization domain structure, a stripe domain along the swiping path was formed and subsequently imaged by the Kerr imaging system. Then the degree of ellipticity of laser was adjusted to the next value

and the laser spot was moved to a lower position on the sample and swiped again horizontally across. Then the above steps repeated and, in the end, an MOKE image with the initial domain pattern plus multiple stripe-domain was finally captured. The MOKE images shown in this chapter are the subtracted images between the final MOKE images and the MOKE image taken at the magnetization saturation, to obtain magnetic contrast. The thermal demagnetization is characterized by the formation of magnetic domains with random white (⊙) or black (⊗) orientation, whereas HD-AOS describes fully deterministic magnetization reversal of the samples, exhibiting either pure white domain stripe or black domain stripe after exposing by laser pulse. AOS only happened in a relatively narrow laser fluence window [29, 203], below or above the fluence will cause the thermal demagnetization occurs. A laser fluence of 6 mJ/cm^2 was found to be able to trigger AOS in Co/Pt sandwich sample with Co thickness of 0.8 nm. The magnetic domain stripes of this sample excited by the laser beam with various degree of ellipticity are presented in Figure 85. For the left two figures, the helicity of the pump laser pulse varied from right hand circularly polarization (σ+) to linearly polarization (L), whereas the right two figures, the helicity of the pump laser pulse varied from left hand circularly polarization (σ-) to linearly polarization (L), respectively.

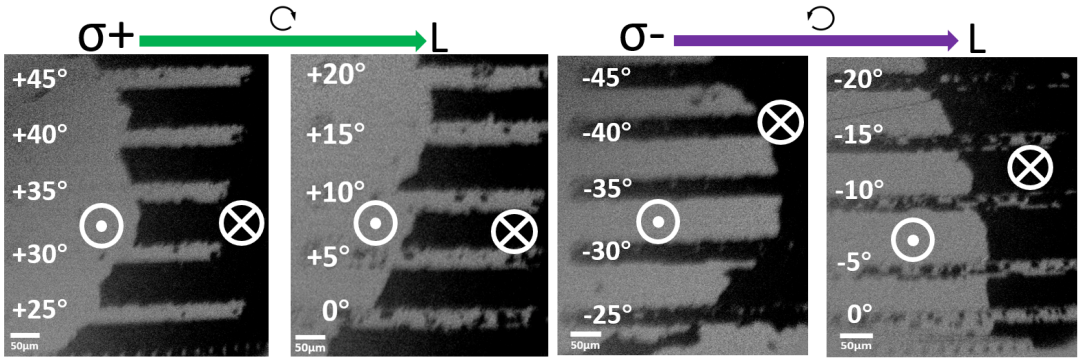

Figure 85. MOKE images of All-optical magnetization switching induced by laser beam with 20 different degree of ellipticity in the Co/Pt sample with Co thickness of 0.8 nm at a fixed laser fluence of 5.6 mJ/cm^2. The left two images are taken when the degree of ellipticity of laser beam changes from 45° (σ+) to 0°(Linearly) in steps of 5°; and the right two images are taken when the degree of ellipticity of laser beam changes from -45° (σ-) to 0° (Linearly) in steps of 5°. The dark contrast corresponds to magnetization pointing into the plane (⊗), and the white contrast pointing out of the plane (⊙).

Firstly, the λ/4 plate was rotated with its fast axis aligned +45° respect to the optical axis of the polarizer placed just before it. This orientation produced a right-circularly polarized (σ+) laser beam which reversed the magnetization in the white domain (⊙) but does not affect the magnetization of the black domain (⊗). Then the λ/4 plate rotated to +40°, +35°, and +30°, no distinct difference in magnetic contrast was observed compared to that obtained at +45°. Even though the laser beam was no longer circularly polarized and become elliptical, the laser pulse can still reverse the white magnetic domain (⊙) to the black domain (⊗). As the λ/4 plate continuously rotated from +25° to 0°, random multi-domain pattern occurred along the swiped path in both the white and black domains indicating that the laser pulses began to demagnetize instead of revering white domain (⊙) to black domain (⊗). The demagnetized states consist of small domains which are randomly black and white oriented by each excitation event. This demagnetization phenomenon getting more and more profound as the fast axis of the λ/4 plate rotating from 25° to 0°. The similar scenario was observed when the sample was exposed to pump laser pulses with the degree of ellipticity changing from -45° to 0° (σ- to linear). The left-circularly/elliptically polarized laser pulses with degree of ellipticity between -45° to -30° reversed, this time, the white magnetic domain (⊙) to the black domain (⊗) instead. Demagnetization occurred when the degree of ellipticity of laser illumination is between -25° to 0° as shown in the right two images in Figure 85.

To explore the combination effect of laser fluence and degree of ellipticity on HD-AOS, systematical measurements were performed on all five Co/Pt sandwich layer samples as presented in the following. To simply the experimental procedure without compromising physical insight, the laser fluence was varied, and for each laser fluence, the degree of ellipticity was varied between +45° to 0° only. For all the five samples, the circularly polarized laser pulses with various laser fluence were first applied in order to examine whether the samples can be switched by a circularly polarized laser or not. Then the degree of ellipticity of the laser pulses were varied together with laser fluence on the samples which exhibited HD-AOS. HD-AOS were observed in Co/Pt sandwich sample with Co thickness of 0.6 nm and 0.8nm. The other three samples of Co thickness of 0.4 nm, 1 nm and 1.2 nm, only heat-induced demagnetization was found.

6.3.1 Si/Ta/Pt/ Co (0.4 nm)/Pt

Wide-field Kerr images of the Co/Pt sample with Co thickness of 0.4 nm taken under various laser fluence from 4.5 mJ/cm^2 to 17 mJ/cm^2 are shown in Figure 86.

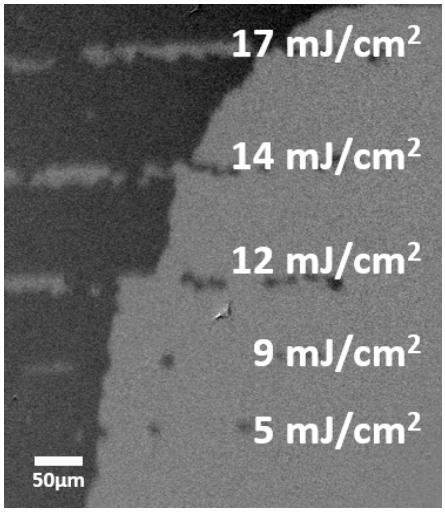

Figure 86. MOKE images of Si/Ta/Pt/ Co (0.4 nm)/Pt /Pt sample after being swiped by the right-circularly polarized laser pulse with different laser fluence.

The above figure shows the magnetization states after exposing to the right-circularly polarized pump laser pulses with different laser fluence. Apparently, only random white and black domains were observed in the beam path after excitation of the laser pulses. The circularly polarized laser pulses are unable to reverse the magnetization from one state to another. When the pump laser fluence was higher than 12 mJ/cm^2, the part of the sample, where the laser beam has illuminated, was found magnetically hardened, i.e., the coercivity of this part increased. This could be due to that the local crystal structure may be modified by the heat of the laser pulses. The Co thickness of this sample is 0.4 nm, and this thickness may be too thin to undertake the laser pulses of such high power. As far as I know, there is no literature ever reported a successful AOS observation on a sample that Co thickness is less than 0.6 nm.

6.3.2 Si/Ta/Pt/ Co (0.6 nm)/Pt

When the thickness of Co increases to 0.6 nm, the sample begins to switch from one saturation state to another by the circularly polarized pump laser pulses. Figure 87 shows the MOKE image of the domain pattern after being swiped by the right-circularly polarized pump laser pulses with different laser power from 20 μW to 40 μW. The permanent effect caused by laser heating occurred when the laser power was increased to 40 μW, which was the maximum power applied for this sample.

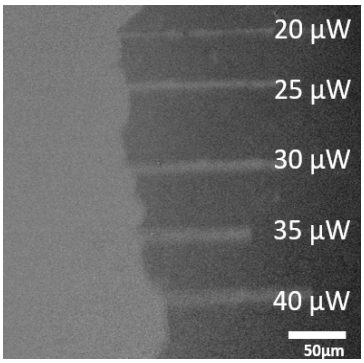

Figure 87. MOKE image of domain pattern in Si/Ta/Pt/ Co (0.6 nm)/Pt /Pt sample after being swiped by the right-circularly polarized laser pulses with different laser power.

As we can see from Figure 87, the right-circularly polarized pump laser pulses reverse the black domain (⊗) to the white domain (⊙), and not affect the original white domain. In order to get a qualitative measure of to what extent the circularly polarized pump laser pulses reverse the domain from one state to another, a digital image processing via Matlab was employed to calculate how 'white" the reversed stripe domain is. In the digital image processing, the contrast is reflected by a greyscale value and stored in computer, and the greyscale value of each pixel of those acquired images was stored in 12-bit binary in our Kerr imaging system. If a pixel is complete black, its greyscale gives a value '0', and when a pixel is complete white, the greyscale value is '4096'. Therefore, the laser-induced switching rate of a black domain region turning into a white stripe domain can be characterised by the grey scale of the region. In the following analysis, for each stripe domain swiped by laser beam, a region of a fixed area within each beam path is selected, and the greyscale value of each pixel in that region is summed. This sum of the greyscale of each region is then normalised with the sum of greyscale values of a reference region from the original white domain,

which gives the switching percentage of this strip domain. Therefore, the switching rate is given by:

$$\rho = \frac{\sum laser}{\sum Ref} \times 100\%$$

Where $\sum laser$ denotes the sum up greyscale value of a fixed region irradiated by laser pulses, $\sum Ref$ denotes the sum up greyscale value of a reference region with the same area size in the original white domain part.

Now, systematically measurements were conducted by rotating the λ/4 plate from σ+ (+45°) to L (0°) at a step of 5°, and sweeping the laser cross the sample surface at each step. This process was repeated at each laser power employed in Figure 87. For each laser power, the final states of HD-AOS induced by various degree of ellipticity were capture by a MOKE image and presented at the left side of each panel of Figure 88. The magnetization switching percentage for each stripe of each MOKE image was calculated and the results are also present next to its MOKE image, at the right side of each panel of Figure 88.

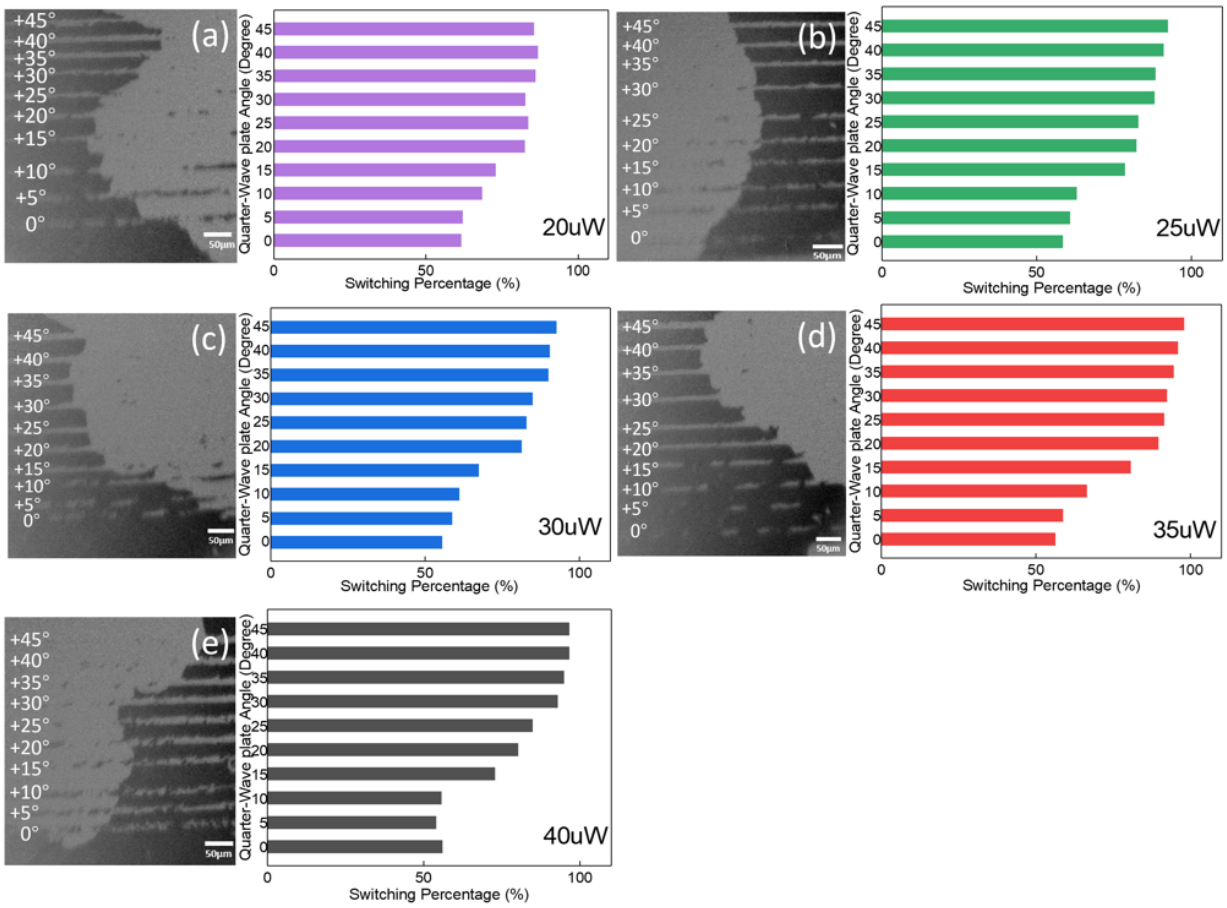

Figure 88. HD-AOS Co (0.6 nm)/Pt thin film swiped by laser pulses. The white digits denote the fast axis angle of the λ/4 plate angle, which was rotated from +45° (right-hand circularly polarized/σ-) to 0° (Linearly polarized/L). The left side of each panel is the Kerr images under different laser power., and the right side is histogram of the calculated switching percentage of each swiped strip domain. From [(a) to (e)] laser power varies from 20 μW, 25 μW, 30 μW, 35 μW, and to 40 μW, respectively.

In Figure 88 (a), when the laser power is 20 μW, the maximum switching percentage achieved is only 86% even with a prefect left circularly (σ–) polarized beam (the λ/4 plate at +45°). This indicates that there is still small part of black domains remain unswitched, which can hardly be seen from the image by our naked eyes. Interestingly, the λ/4 plate was rotated to +40°, +35°, and +20°, the switching percentage remains almost the same, which is around 86±5%. Until the λ/4 plate rotated to 15° or below, the switching percentage drops drastically to around 55±5%. This region has a greyscale half way between black and white. This indicates that the selected region irradiated by the laser consists of random black and white domains and

has a net magnetization equal to zero. When the laser power increased to 25 μW, for the first four angles of the λ/4 plate (+45°, +40°, +35°, +30°), the switching percentage has no obvious difference, until the λ/4 plate angle below +30°, the switching percentage begins to drop abruptly. The trend of degree of ellipticity dependence is slightly different among the measurements with the other laser power of 30 μW, 35 μW, and 40 μW.

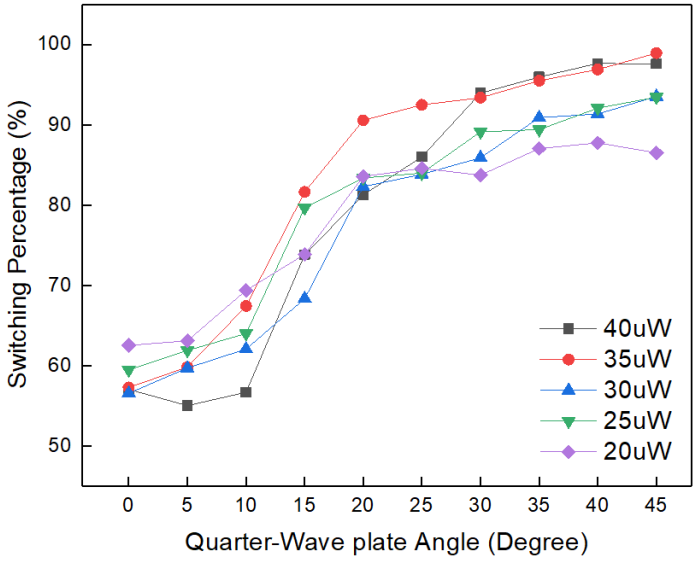

Figure 89. The switching percentage of Co (0.6 nm)/Pt thin film as a function of degree of ellipticity under 5 different pump laser power.

To understand the dependence of degree of ellipticity on the switching percentage, the switching percentage is plotted as a function of the fast axis angle of the λ/4 plate for each laser power in Figure 89. At the +45°, when the laser power increases in steps of 5 μW from 20 μW to 35 μW, the switching percentage increases gradually from 86±5% to 99±2%. When the fast axis angle is between +30° to +45°, the switching percentage is increased as the laser power increases from 20 μW to 35 μW. When the fast axis angle is at +20° or +25°, the 35 μW laser power can achieve a distinct higher switching percentage than that at lower laser powers at the same degree of ellipticity. When the pump power reaches to 40 μW, the switching percentage is slightly lower than the switching percentage at 35 μW laser power. As mentioned earlier in this section, the 40 μW laser power started to cause some permanent damage of the sample surface, which results in a lower greyscale value compared to that at 35 μW laser

power. At this laser power, a highest degree of demagnetization is also observed when the laser polarization is linear (0°). This group of experiments unambiguously demonstrates the dependence of HD-AOS on combination of the degree of ellipticity and the power of laser. The more circular the laser polarization is, the less the laser power is needed to achieve the same switching percentage. Also, the degree of circularly polarization of laser is somehow not that critical, because even when the λ/4 plate angle is set down to 35°, the laser pulses can still reverse the magnetization.

6.3.3 Si/Ta/Pt/ Co (0.8 nm)/Pt

Similarly sets of experiments were carried on Co/Pt thin film sample with the Co thickness of 0.8 nm in order to study the thickness dependence of AOS observation. The laser power was again varied from 20 μW to 25 μW, 30 μW, 35 μW and 40 μW, for each laser power, the Kerr images of the final states of HD-AOS induced by various degree of ellipticity are presented at the left side and the calculated switching percentage of each ellipticity are presented at the right side of each panel in Figure 90. To understand the dependence of degree of ellipticity on the switching percentage, the switching percentage is again plotted as a function of the fast axis angle of the λ/4 plate for each laser power in Figure 91. And to directly compare the Co thickness dependence, the switching percentage induced by right-circularly polarized laser (at+45°) for the two samples with Co thickness of 0.6 nm and 0.8 nm are plotted as a function of laser power in Figure 92. The switching percentage in this Co/Pt thin film with 0.8 nm Co thickness increases almost linearly when the λ/4 plate rotates from 0° to 45°. On the other hand, in Figure 89, the switching percentage in the sample with 0.6 nm Co thickness has a steep increase when the λ/4 plate at an angle between 20° to 25°. The switching percentage before and after this angle regime stays flat for all different laser power. Also, for the same pump power, the switching percentage is different for these two sample with different Co thickness. Comparing Figure 88 (a) and Figure 90 (a), for example, one can see that 20 μW laser power is not sufficient to either demagnetize the magnetization a thicker Co sample at linear polarization or reverse it at circular polarization. This trend also applies to the other four different pump laser powers, as for the laser of power 35 μW with right-circular polarization (at

+45°) the switching percentage is 99±2% for the sample with Co thickness of 0.6 nm, while 97±2% for the sample with Co thickness of 0.8 nm. This could due to that a thicker film needs more energy to achieve the same effect in a thinner film. However, the 40 μW laser power again caused permanent damage to the sample and hence no higher laser power was applied.

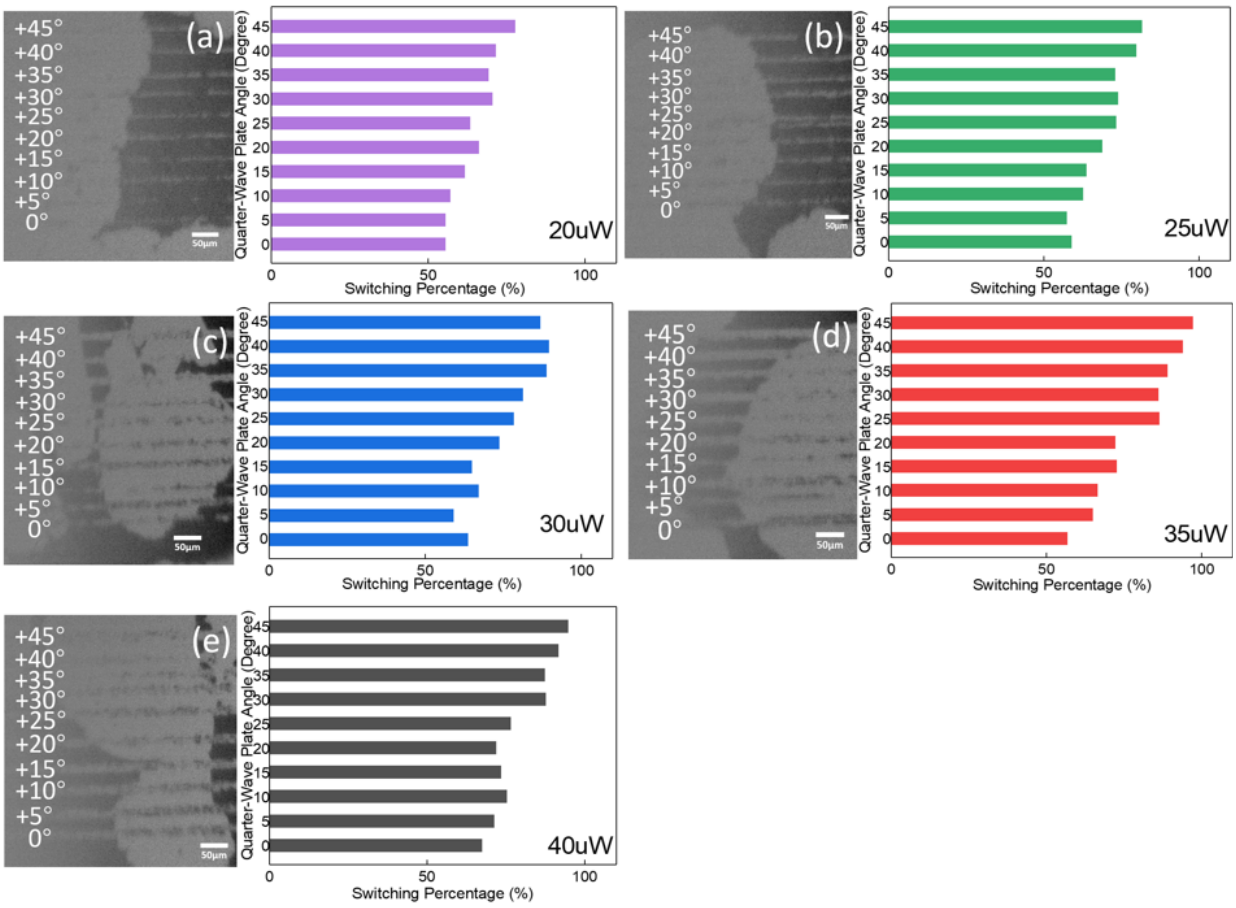

Figure 90. HD-AOS of Co (0.8 nm)/Pt thin film swiped by laser pulses. The white digits denote the fast axis angle of the λ/4 plate angle, which was rotated from +45° (right-hand circularly polarized/σ-) to 0° (Linearly polarized/L). The left side of each panel is the Kerr images under different laser power, and the right side is histogram of the calculated switching percentage of each swiped strip domain. From [(a) to (e)] laser power varies from 20 μW, 25 μW, 30 μW, 35 μW, and to 40 μW, respectively.

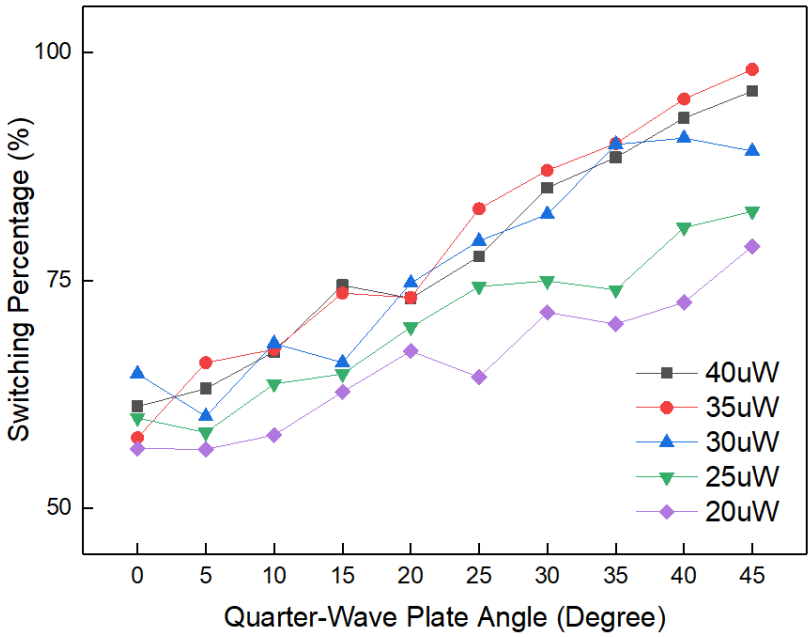

Figure 91. The switching percentage of Co (0.8 nm)/Pt thin film sample as a function of degree of ellipticity under 5 different pump laser power.

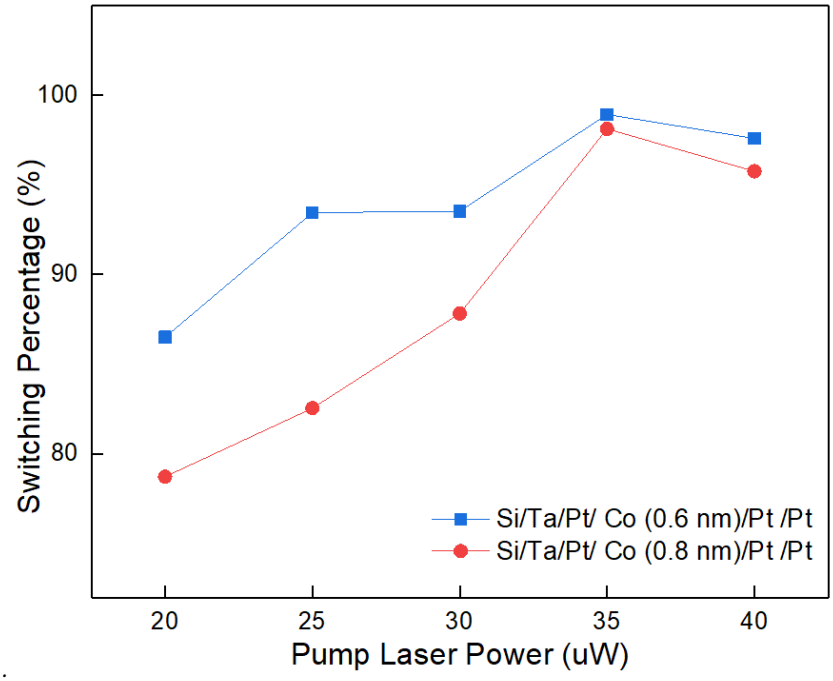

Figure 92. The switching percentage of the two Co/Pt thin films with different Co thickness versus the five pump laser powers. The λ/4 plate is set at +45°, producing right-circularly polarized laser (σ+) pulses.

6.3.4 Si/Ta/Pt/ Co (1 nm)/Pt and Si/Ta/Pt/ Co (1.2 nm)/Pt

Similarly sets of experiments were also conducted on Co/Pt thin film sample with the Co thickness of 1 nm and 1.2 nm. However, no AOS phenomenon was observed on either of these two samples. Only demagnetization pattern was observed for each laser power used. The MOKE images captured under different laser power are presented in Figure 93 for both samples. As presented in the inserts of Figure 80, the magnetic domain size is strongly dependent on the magnetic layer thickness, the reason of this is due to the competition between the dipolar energy and the domain wall energy stabilizing small and large domains. In 2016, S. Mangin *et al* concluded that one of the criterions for the observation of AOS is that the equilibrium size of magnetic domains forming during the cooling process should be larger than the laser spot size [165]. After the circularly polarized laser pulses pumped the magnetized sample, the magnetization tends to break into tiny small domains, if the magnetic domain size inside the material is larger than the laser spot size, then AOS can be observed, otherwise thermal demagnetization will be observed. Moreover, in 2017, J. Y. Bigot *et al* also mentioned that the AOS in ferromagnetic films requires that the laser spot matches with the specific domain sizes [204]. Back to our case, this could be the reason that we didn't successfully observe the AOS in this two samples, but only thermal demagnetization was observed.

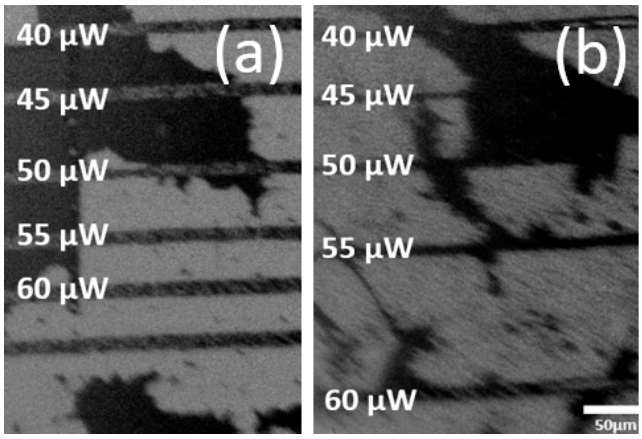

Figure 93. Co/Pt thin film swiped by circularly polarized laser with different pump power. (a) is Co thickness of 1nm (b) is Co thickness of 1.2 nm

6.4 Conclusion

In conclusion, I had investigated all-optical magnetic ordering manipulation experiments on five ferromagnetic Co/Pt rare-earth free thin films with different Co thickness. For the samples with the Co thicknesses of 0.6 nm and 0.8 nm, I successfully observed the HDAOS. By rotating the angle of the λ/4 plate, I varied the degree of the polarization of the laser pulses to explore the detailed mechanism of AOS observation. The most important finding is that the underlying mechanism for the AOS phenomenon in Co/Pt thin film is unequivocally linked to the helicity, but the degree of the helicity of the pump laser is somehow not that critical. For the λ/4 plate angle going down even to -35°, an elliptically polarized laser pulses can still switch the magnetization state to another opposite state very well. The AOS observation in Co/Pt is can be explained by an effective magnetic field generated by circularly polarized light via Inverse Faraday Effect (IFE), and the effective magnetic field is maximum for circularly polarized light, while it vanishes for linearly polarized light. More recently, S. Mangin reported that the DW will move in one direction depended with the light helicity, which will result in the shrinkage or growth of domains of opposite magnetization [195]. This discovery is important to understand the mechanism behind this helicity-dependent laser-induced magnetization switching in Co/Pt. Back to our experiments, the laser beam was scanned across the opposite magnetic domains with two distinct magnetization states, thus, a different absorption rate of the white magnetic domain (⊙) and the black domain (⊗) would result in an additional temperature gradient across the DW according to the MCD effect. Therefore, MCD effect will trigger the temperature gradient acts as an effective field that can drive the DW towards the regions with higher temperature if it is greater than the depinning field at the laser temperature [205]. According to Ref [206], a MCD of 2% corresponds to a temperature gradient of about 10 K. In Co/Pt thin films, the width of the domain wall is around 10 nm, thus the temperature gradient across the DW due to MCD is on the order of 1 K/nm, based on the calculation, an estimated effective field of 7 mT is found [195], and this small effective field is close to the value used in the previously discussed athermal model and is on the same order of magnitude as depinning fields in Co/Pt thin films [166, 207]. Moreover, the pure thermal effect cannot be involved to explain the our AOS observation in the [Co/Pt]. In the RE-TM system, the different

ultrafast demagnetization rate of the sublattices accompany with the conservation of angular momentum leads the toggle switching of the magnetization, however in the [Co/Pt] system, such explanation lacks requisite preconditions. Overall, the observation of AOS in our experiments shall attribute to the combined contribution of IFE and MCD effect. Our findings provide insightful reference for the future developing of the magnetic storage devices. These experiments unambiguously demonstrate that all-optical magnetization reversal can be achieved by polarized femtosecond laser pulses, and the femtosecond pump laser pulses are indeed very novel and efficient stimuli for the manipulation of the magnetic order. However, the current research is largely based on semi-empirical models of the effective magnetic fields and heat pulses [208], given the development of compact femtosecond laser source [209], it is still a long journey to provide high-speed design protocols for the practical magnetic storage devices.

Chapter 7 Summary and Future Work

7.1 Summary

The controlling of the magnetization process in magnetic nanostructures is highly relevant to potential applications in future magnetic recording technologies. My work mainly focused on the experimental studies of the magnetization switching driven by magnetic field and laser field in a variety of magnetic materials, in order to provide insightful support for the future applications. Two types of key experimental techniques have been involved to investigate the magnetization dynamics. One is the self-built wide-field magneto-optical Kerr imaging system, which is used to study the domain walls motion in patterned Permalloy nanowires with different notch geometries. Another one is the pump and probe time-resolved magneto-optical Kerr effect (TR-MOKE) technique, which is used to investigate the laser-induced precession dynamics in the highly perpendicular ferromagnetic Co/Pt multilayer. Finally, those two techniques were combined together in order to investigate the influence of the laser helicity to the observation of the all optical switching in Co/Pt thin films. In the following, the conclusions based on the experimental results are presented with suggestions for future work.

In *Chapter 4*, I have successfully built the wide-field Kerr imaging system. A set of Permalloy nanowires with different notch depth as well as notch geometries were fabricated by E-beam lithography. The SEM measurements show the all the nanowires are well defined and have a relatively high quality. It has been demonstrated that the Kerr imaging is capable of the observation of the magnetic field driven domain wall propagation in the planar Permalloy nanowires. Digital image enhancement helps to increase domains contrast for nano-structures even with very weak Kerr effect. Our Kerr imaging system is also able to do spatial-resolved analysis, which means it can analyse any region of interest in the nanowire. In this project, I had selected four different regions in the nanowires, the nucleation pad, the junction between nucleation pad and the wire part, before notch and after notch. Interestingly, I found that when the notch depth reaches to 200 nm, the coercivity difference at after notch region, with the same notch geometry but opposite orientations (left and right) can reach up to 82%.

On the other hand, this effect is relatively weak in the other nanowires with the notch depth greater than 200 nm. Considering the stochastic depinning scenarios via different domain wall types, I had repeated the measurements for 40 times to get the averaged loops. As expected, the averaged loops at the region after notch show a step like magnetization reversal process, which indicates two distinct depinning processes. However, the depinning field of the left type notch is always larger than that of the right type notch geometry. In order to find out the mechanism of domain wall propagation in different notch geometries, micromagnetic simulation via Mumax was used to simulate the experimental results. The simulation results show a good agreement with the experiments. Moreover, the simulated spin configurations inside the wall show a highly dependence on the notch edge slope close to the nucleation pad. Thus, the engineering of the detailed notch geometries may substantially eliminate the stochastic depinning process, which is of great importance for the applications of the nanowire in the future data storage devices. Due to its flexibility and versatility, the setup was also modified to investigate the magnetic samples with strong perpendicular anisotropy as presented in *Chapter 6*.

The pump and probe TR-MOKE technique is a powerful tool to study the magnetization precession and the magnetic damping. It allows direct observation of the magnetization precession in time domain using femtosecond laser pulses. In *Chapter 5*, I had investigated the laser-induced magnetization precession dynamics in Co/Pt multilayers structures. By the phenomenological fitting formula, the relaxation time and precessional frequency were retrieved from the Kerr signals, thus the effective Gilbert damping constants α_{eff} of the Co/Pt multilayer with different layer repetition were calculated. The results show that the α_{eff} has a significant external field and layer repetition number dependence. The α_{eff} increases as the external field decreases. We propose that the inhomogeneous line broadening (ILB) and other extrinsic conditions, such as interfacial effects and two magnon-scattering, are potentially the main factors contributing to the large damping constant observed at the lower external magnetic field. When the external applied field is increased to a certain level, the values of the extracted α_{eff} tend to stay 'steady'. This could be due to at the higher level of applied field, the extrinsic influence is relatively small. Any significant contribution from two-magnon scattering can be excluded from the mechanism and

the main origin of the effective damping at higher external field is an intrinsic mechanism. The enhancement of the α_{eff} value with more Co/Pt layer repeation could be due to the interfacial effect or decoherence. As the repeation number is increased, so as the lattice mismatching in Co/Pt structures is increased. This increased dislocation may promote electron hopping between two different sites which increases the intrinsic damping in the thicker films.

In *Chapter 6*, I had experimentally investigated the optical response of ferromagnetic Co/Pt multilayers under the 100fs laser pulses without applying any external field. The experimental techniques involved in the previous chapters were combined. The magneto-optical response of the Co/Pt films under the action of 100 fs laser beam was probed using a magneto-optical Kerr microscope in order to image the magnetic domains in transmission. By rotating the angle of the quarter-wave (λ/4) plate, I had demonstrated that the percentage of the all optical switching (AOS) of the Co/Pt thin films decreases with the decrease of the degree of laser helicity, highlighting the essential role of the helicity of the pumping laser in the AOS observation. However, the degree of the helicity of the laser is somehow not that critical, for even the λ/4 plate angle downs to +35°, a relatively poor circularly polarized pump laser pulses can still reverse the magnetization state to another opposite state very well. The two major mechanisms heavily debated in the literatures are the inverse Faraday effect (IFE) and the magnetic circular dichroism (MCD). Here, the effective field induced by the IFE could be used to explain the helicity dependent all optical switching observed in the Co/Pt thin films. Our results should have contributed significantly to a further understanding of the AOS mechanism in the ferromagnetic materials, which is very important for the applications of the AOS in high accessing rate data storage devices.

7.2 Future Work

For further research purposes, it is suggested that the following ideas could be considered. Regarding the experiments of domain wall motion in nanowires, more experiments involving different notch geometries can be continued. In this thesis, the notch structure is located at one side of the nanowire, and in the future research, we can put the notch structure at both sides of the wire, so that a 'bow-tie' structure can be formed. We will be able to study the symmetry dependence of the depinning field. Moreover, domain wall motion via spin transfer torque is one of current research interests. The electrodes can be patterned on the nanowire, and threshold current needed for depinning the nanowires with different notch geometries can be investigated. For the laser induced precession dynamics in Co/Pt multilayers. In this thesis, the pump laser was linearly polarized, and in the future study, the pump laser with different helicities can be used, so that the helicity dependence of precession dynamics in Co/Pt multilayers can be investigate. Since we had successfully demonstrated the AOS in Co/Pt thin films, there could be some interesting observation in helicity depend laser induced coherent control of spin precession in Co/Pt. For the all optical magnetic switching, several important features remain to be confirmed, and thus further theoretical and experimental work would be required in the future to get a better understanding of the all optical switching. Until now, the AOS has only been observed in magnetic systems involving perpendicular anisotropy, it would be very interesting to study the opto-magnetic effect on other magnetic materials like magnetite and CoFeB. Another interesting topic is to use a time-resolved magneto-optical imaging technique. However, performing a time-resolved imaging of the domain structures requires both high temporal and spatial resolutions, which requires further improvement of the experimental techniques. Furthermore, to what extend does the thermal effect influence the AOS observations remains unclear. We propose to use a duel-pump setup. The first pump beam is to heat the sample and thus the first one is linearly polarized. The second one aims to switch the sample, therefore, the second laser beam will be circularly polarized. Finally, since all the experiments are heavily dependent on the performance and condition of the scientific instruments, the improvements of them are very necessary. Powerful processing capabilities, reliable

and reasonable design of the hardware and user interface can further improve the lab efficiency, which could bring more opportunities for greater discoveries.

Abbreviations

3TM	Three Temperature Model
AOS	All Optical Switching
AFM	Atomic Force Microscope
BS	Beam Sampler
BCC	Body Centred Cubic
CCD	Charge-Coupled Device
CMOS	Complementary Metal-Oxide-Semiconductor
CW	Continuous Wave
CCW	Clockwise Domain Wall
CCCW	Counterclockwise Domain Wall
DOS	Density of State
DW	Domain Wall
DDW	Domain Wall Width
EA	Easy Axis
EBL	Electron Beam Lithography
FCC	Face Centered Cubic
FM	Ferromagnetic Metal
FMR	Ferromagnetic Resonance
FWHM	Full Width at Half Maximum
GMR	Giant Magnetoresistance
HA	Hard Axis
HDD	Hard Disk Drive
HD-AOS	Helicity-Dependent All-Optical Switching
HI-AOS	Helicity-Independent All-Optical Switching
IPA	Isopropyl Alcohol
IFE	Inverse Faraday Effect
LCP	Left-handed Circularly Polarized
LLB	Landau-Lifshitz-Bloch
LLG	Landau-Lifshitz-Gilbert
LED	Light Emitting Diode
LIB	Inhomogeneous Line Broadening

MFM	Magnetic Force Microscope
MIBK	Methyl Isobutyl Ketone
MBE	Molecular Beam Epitaxy
MCD	Magnetic Circular Dichroism
MFM	Magnetic Force Microscopy
ML	Monolayer
MOKE	Magneto-Optic Kerr Effect
MR	Magneto-Resistance
MRAM	Magnetoresistive Random-Access Memory
MTJ	Magnetic Tunnel Junction
NM	Non-Magnetic Metal
OOMMF	Objective Oriented Micromagnetic Framework
PMMA	Polymethyl-Methacrylate
PLD	Pulsed Laser Deposition
PM	Permanent Magnet
PMR	Perpendicular Magnetic Recording
PSSW	Perpendicular Standing Spin Wave
PMA	Perpendicular Magnetization Anisotropy
RCP	Right-handed Circularly Polarized
RT	Room Temperature
RM	Racetrack Memory
SC	Semiconductor
SOC	Spin-orbit Coupling
SEM	Scanning Electron Microscope
SQUID	Superconducting Quantum Interference Device
STEM	Scanning Transmission Electron Microscope
STT	Spin Transfer Torque
SNR	Signal to Noise Ratio
TEM	Transmission Electron Microscopy
TMR	Tunneling Magnetoresistance
TRMOKE	Time-Resolved Magneto-optic Kerr Effect
UHV	Ultrahigh Vacuum
UMA	Uniaxial Magnetic Anisotropy

VSM	Vibrating Sample Magnetometer
VW	Vortex Wall
XMCD	X-ray Magnetic Circular Dichroism

List of Symbols

α	Magnetic Damping Constant
α_{eff}	Effective Magnetic Damping Constant
β	Faraday Rotation
ε	Permittivity Tensor
$\hbar$	Planck's Constant
$\hbar$	Reduced Planck's Constant
ϕ	Work Function
θ_k	Kerr Rotation
γ	Gyromagnetic Ratio
ρ	Resistivity
μ_r	Relative Magnetic Permeability
μ_0	Magnetic Constant Permeability of Free Space
μ_B	Bohr Magneton
ξ	Spin-Orbit Interaction Energy
λ	Wavelength of Light
ω	Angular Frequency
τ	Precession Decay Time
τ_E	Electron Scattering Time
$\langle \boldsymbol{S} \rangle$	Spin Operator
$\mathcal{H}$	Hamiltonian
$\mathcal{J}_{ij}$	Exchange Integral
J_c	Threshold Current Density
f	Frequency of the Magnetization Precession
g	Landé g factor
$\boldsymbol{k}$	Wave Vector
k_B	Boltzmann Constant
m	Magnetic Moment
s	total spin number
B	magnetic flux density
$D\ (E_F)$	Density of States at Fermi Level

E_F	Fermi Energy
G_{ij}	Coupling Constant between Electrons, Spins, and Lattice
$\boldsymbol{H}$	Magnetic Field
$\boldsymbol{H_{eff}}$	Effective Magnetic Field
I	Light Intensity
J	Exchange Constant
J_c	Threshold Current Density in MTJ
K_u	Uniaxial Anisotropy Constant
K_1	First-order Cubic Anisotropy Constant
M_s	Saturation Magnetization
$\boldsymbol{M}$	Magnetization
T_C	Curie Temperature
T_M	Magnetization Compensation Temperature
T_e	Electron Temperature
T_s	Spin Temperature
T_l	Lattice Temperature

Bibliography

[1] M. G. G. Farmington Hills, "Magnetism," DISCovering Science.Gale Research, 1996. Reproduced in Discovering Collection., 2000.

[2] "http://en.chinaculture.org/library/2008-02/01/content_26344.htm," Web Page.

[3] H. C. Oerstead, "Experiments on the effect of a current of electricity on the magnetic needles," Annals of Philosophy, vol. 16, pp. 273-276, 1820.

[4] "https://en.wikipedia.org/wiki/Magnetic_tape," Magnetic Tape, En.wikipedia.org. (2018).

[5] M. N. Baibich et al., "Giant magnetoresistance of (001)Fe/(001)Cr magnetic superlattices," Phys Rev Lett, vol. 61, no. 21, pp. 2472-2475, 1988.

[6] J. S. B. D. A. Thompson, "The future of magnetic data storage technology," IBM J. RES. DEVELOP., vol. 44, pp. 311-322, 2000.

[7] M. P. C. Tsang, H. Santini, .et al., "12 Gb/in/sup 2/ recording demonstration with SV read heads and conventional narrow pole-tip write heads," IEEE Transactions on Magnetics, vol. 35, no. 2, pp. 689 - 694, 1999.

[8] H. L. K. O'Grady, "The limits to magnetic recording-media considerations," Journal of Magnetism and Magnetic Materials, vol. 200, pp. 616-633, 1999.

[9] "https://en.wikipedia.org/wiki/Perpendicular_recording," Perpendicluar Recording, En.wikipedia.org. (2018).

[10] M. Hashimoto, K. Miura, H. Muraoka, H. Aoi, and Y. Nakamura, "Influence of Magnetic Cluster-Size Distribution on Signal-to-Noise Ratio in Perpendicular Magnetic Recording Media," IEEE Transactions on Magnetics, vol. 40, no. 4, pp. 2458-2460, 2004.

[11] S. A. M. Tofail, I. Z. Rahman, and M. A. Rahman, "Patterned nanostructured arrays for high-density magnetic recording," Applied Organometallic Chemistry, vol. 15, no. 5, pp. 373-382, 2001.

[12] D. J. Sellmyer, Yu, M., Thomas, R. A., Liu, Y., & Kirby, R. D. , "Nanoscale design of films for extremely high density magnetic recording," Physics of Low-Dimensional Structures, vol. 1-2, pp. 155-166, 1998.

[13] D. W. a. M. Doerner, "Extremely High-density Longitudinal Magnetic Recording Media," Annu. Rev. Mater. Sci, vol. 30, p. 611, 2000.

[14] M. H. Kryder et al., "Heat Assisted Magnetic Recording," Proceedings of the IEEE, vol. 96, no. 11, pp. 1810-1835, 2008.

[15] J. C. Mallinson, "Recording limitations, in Magnetic Recording Technology," McGraw-Hill,.

[16] H. H. S. S. O. Kim, M. P. Stoykovich, N. J.Ferrier, J. J. de Pablo, and P. F. Nealey, "Epitaxial self-assembly of block copolymers on lithographically defined nanopatterned substrates," Nature, vol. 424, p. 411, 2003.

[17] J. Moritz et al., "Writing and reading bits on pre-patterned media," Applied Physics Letters, vol. 84, no. 9, pp. 1519-1521, 2004.

[18] E. Chen et al., "Advances and Future Prospects of Spin-Transfer Torque Random Access Memory," IEEE Transactions on Magnetics, vol. 46, no. 6, pp. 1873-1878, 2010.

[19] F. J. A. J. A. Katine, and R. A. Buhrman, "Current-Driven Magnetization Reversal and Spin-Wave Excitations in Co/Cu/Co Pillars," Phys Rev Lett, vol. 84, pp. 3149-3152, 2000.
[20] S. S. Parkin et al., "Giant tunnelling magnetoresistance at room temperature with MgO (100) tunnel barriers," Nat Mater, vol. 3, no. 12, pp. 862-867, 2004.
[21] K. L. Wang, J. G. Alzate, and P. Khalili Amiri, "Low-power non-volatile spintronic memory: STT-RAM and beyond," Journal of Physics D: Applied Physics, vol. 46, no. 7, p. 074003, 2013.
[22] S. Ikeda et al., "Tunnel magnetoresistance of 604% at 300K by suppression of Ta diffusion in CoFeB / MgO / CoFeB pseudo-spin-valves annealed at high temperature," Applied Physics Letters, vol. 93, no. 8, p. 082508, 2008.
[23] J. J. Cha et al., "Atomic-scale spectroscopic imaging of CoFeB/Mg–B–O/CoFeB magnetic tunnel junctions," Applied Physics Letters, vol. 95, no. 3, p. 032506, 2009.
[24] K. Lee and S. H. Kang, "Development of Embedded STT-MRAM for Mobile System-on-Chips," IEEE Transactions on Magnetics, vol. 47, no. 1, pp. 131-136, 2011.
[25] W. Jiang et al., "Direct imaging of thermally driven domain wall motion in magnetic insulators," Phys Rev Lett, vol. 110, no. 17, p. 177202, 2013.
[26] J. Z. Sun, "Spin-current interaction with a monodomain magnetic body: A model study," Physical Review B, vol. 62, pp. 570-578, 2000.
[27] P. S. Institute, "Ultrafast Magnetization Dynamics on the Nanoscale," SwissFEL Science Case, pp. 19-31.
[28] E. Beaurepaire, J.-C. Merle, A. Daunois, and J.-Y. Bigot, "Ultrafast Spin Dynamics in Ferromagnetic Nickel," Phys Rev Lett, vol. 76, no. 22, pp. 4250-4253, 1996.
[29] A. Kirilyuk, A. V. Kimel, and T. Rasing, "Ultrafast optical manipulation of magnetic order," Reviews of Modern Physics, vol. 82, no. 3, pp. 2731-2784, 2010.
[30] A. Hubert, Schäfer, Rudolf, "Magnetic Domains," 1998.
[31] G. X. D. A. Allwood, C. C. Faulkner, D. Atkinson, D. Petit, R. P. Cowburn, "Magnetic Domain-Wall Logic," Science, vol. 309, p. 1688, 2005.
[32] M. H. Stuart S. P. Parkin, Luc Thomas, "Magnetic Domain-Wall Racetrack Memory," Science, vol. 320, pp. 190-194, 2008.
[33] C. S. I. Tudosa, A. B. Kashuba, F. King, H. C. Siegmann, "The ultimate speed of magnetic switching in granular recording media," Nature, vol. 428, pp. 831-833, 2004.
[34] S. I. A. M. B. Agranat, A. B. Granovskii, and G. I. Rukman, "Interaction of picosecond laser pulses with the electron, spin, and phonon subsystems of nicke," Sov. Phys. JETP, vol. 59, pp. 804-806, 1984.
[35] A. Vaterlaus, D. Guarisco, M. Lutz, M. Aeschlimann, M. Stampanoni, and F. Meier, "Different spin and lattice temperatures observed by spin-polarized photoemission with picosecond laser pulses," Journal of Applied Physics, vol. 67, no. 9, pp. 5661-5663, 1990.

[36] A. Vaterlaus, T. Beutler, and F. Meier, "Spin-lattice relaxation time of ferromagnetic gadolinium determined with time-resolved spin-polarized photoemission," Phys Rev Lett, vol. 67, no. 23, pp. 3314-3317, 1991.
[37] E. Carpene, E. Mancini, C. Dallera, M. Brenna, E. Puppin, and S. De Silvestri, "Dynamics of electron-magnon interaction and ultrafast demagnetization in thin iron films," Physical Review B, vol. 78, no. 17, 2008.
[38] M. v. K. B. Koopmans, J. T. Kohlhepp, and W. J. M. de Jonge, "Ultrafast Magneto-Optics in Nickel: Magnetism or Optics?," Phys Rev Lett, vol. 85, pp. 844-847, 2000.
[39] G. P. Zhang, W. Hübner, G. Lefkidis, Y. Bai, and T. F. George, "Paradigm of the time-resolved magneto-optical Kerr effect for femtosecond magnetism," Nature Physics, vol. 5, no. 7, pp. 499-502, 2009.
[40] A. V. N. Ganping Ju, "Ultrafast Time Resolved Photoinduced Magnetization Rotation in a Ferromagnetic/Antiferromagnetic Exchange Coupled System," Phys Rev Lett, vol. 82, pp. 3705-3708, 1999.
[41] M. v. Kampen, B. Koopmans, J. T. Kohlhepp, and W. J. M. d. Jonge, "Laser-induced precession in canted-spin ferromagnets," Journal of Magnetism and Magnetic Materials, vol. 240, p. 3, 2002.
[42] M. Van Kampen et al., "All-optical probe of coherent spin waves," Phys Rev Lett, vol. 88, no. 22, p. 227201, 2002.
[43] J. Hohlfeld, T. Gerrits, M. Bilderbeek, T. Rasing, H. Awano, and N. Ohta, "Fast magnetization reversal of GdFeCo induced by femtosecond laser pulses," Physical Review B, vol. 65, no. 1, p. 012413, 2001.
[44] C. D. Stanciu et al., "All-optical magnetic recording with circularly polarized light," Phys Rev Lett, vol. 99, no. 4, p. 047601, 2007.
[45] I. Radu et al., "Transient ferromagnetic-like state mediating ultrafast reversal of antiferromagnetically coupled spins," Nature, vol. 472, no. 7342, pp. 205-208, 2011.
[46] M. Savoini et al., "Highly efficient all-optical switching of magnetization in GdFeCo microstructures by interference-enhanced absorption of light," Physical Review B, vol. 86, no. 14, p. 140404, 2012.
[47] C. E. Graves et al., "Nanoscale spin reversal by non-local angular momentum transfer following ultrafast laser excitation in ferrimagnetic GdFeCo," Nat Mater, vol. 12, no. 4, pp. 293-298, 2013.
[48] S. Alebrand et al., "Light-induced magnetization reversal of high-anisotropy TbCo alloy films," Applied Physics Letters, vol. 101, no. 16, p. 162408, 2012.
[49] S. Alebrand et al., "Subpicosecond magnetization dynamics in TbCo alloys," Physical Review B, vol. 89, no. 14, p. 144404, 2014.
[50] T. Y. Cheng et al., "Temperature Dependence of All-Optical Ultrafast Magnetization Switching in TbFeCo," IEEE Transactions on Magnetics, vol. 48, no. 11, pp. 3387-3389, 2012.
[51] T. Cheng et al., "Dual-pump manipulation of ultrafast demagnetization in TbFeCo," Physical Review B, vol. 93, no. 6, p. 064401, 2016.
[52] X. Lu et al., "Roles of heating and helicity in ultrafast all-optical magnetization switching in TbFeCo," Applied Physics Letters, vol. 113, no. 3, p. 032405, 2018.

[53] S. Mangin et al., "Engineered materials for all-optical helicity-dependent magnetic switching," Nat Mater, vol. 13, no. 3, pp. 286-292, 2014.
[54] C. H. Lambert, S. Mangin, B. S. D. C. S. Varaprasad, Y. K. Takahashi, M. Hehn, and E. E. Fullerton, "All optical control of ferromagnetic thin films and nanostructures," Science, vol. 345, no. 6202, pp. 1337-1340, 2014.
[55] D. Jiles, "Introduction to Magnetism and Magnetic Materials," 1998.
[56] R. C. O'Handley, "Modern Magnetic Materials Principles and Applications," Wiley, 2000.
[57] S. Chikazumi, "Physics of ferromagnetism," 2nd ed, Oxford University Press, 1997.
[58] "https://archive.cnx.org/contents/57fb8d0a-b4be-4b89-beb5-e1ce01520de9@1/chapter-7-section-7-6-3-hysteresis-loops-of-hard-iron-and-soft-iron," Web Page.
[59] "https://en.wikipedia.org/wiki/Stoner%E2%80%93Wohlfarth_model," Stoner–Wohlfarth model, En.wikipedia.org. (2018).
[60] "https://commons.wikimedia.org/wiki/File:Domain_walls_by_Zureks.png," Domain walls by Zureks.png, En.wikipedia.org. (2018).
[61] E. J. Torok, A. L. Olson, and H. N. Oredson, "Transition between Bloch and Néel Walls," Journal of Applied Physics, vol. 36, no. 4, pp. 1394-1399, 1965.
[62] J. Miltat, "Spin Dynamics in Confined Magnetic Structures," Springer, 2001.
[63] C. J´ozsa, "Optical detection of the magnetization precession," PhD Thesis, Technische Universiteit Eindhoven, 2006.
[64] S. Karakurt, R. W. Chantrell, and U. Nowak, "A model of damping due to spin–lattice interaction," Journal of Magnetism and Magnetic Materials, vol. 316, no. 2, pp. e280-e282, 2007.
[65] L. D. a. L. Landau, E.M., "On the Theory of the Dispersion of Magnetic Permeability in Ferromagnetic Bodies," Phys. Z. Sowjetunion, vol. 8, pp. 153-164, 1935.
[66] T. L. Gilbert, "A Lagrangian formulation of the gyromagnetic equation of the magnetic field," Phys. Rev., vol. 100, p. 1243, 1955.
[67] S. Azzawi, A. T. Hindmarch, and D. Atkinson, "Magnetic damping phenomena in ferromagnetic thin-films and multilayers," Journal of Physics D: Applied Physics, vol. 50, no. 47, p. 473001, 2017.
[68] M. D. Kaufmann, Ph.D. thesis, Georg-August-Universitat Gottingen, 2006.
[69] H. Suhl, "Theory of the magnetic damping constant," IEEE Transactions on Magnetics, vol. 34, no. 4, pp. 1834 - 1838, 1998.
[70] V. L. S. a. H. N. Bertram, "Impurity relaxation mechanism for dynamic magnetization reversal in a single domain grain," Physical Review B, vol. 61, no. 22, p. 14893, 2000.
[71] C. Kittel and E. Abrahams, "Relaxation Process in Ferromagnetism," Reviews of Modern Physics, vol. 25, no. 1, pp. 233-238, 1953.
[72] M. C. Hickey and J. S. Moodera, "Origin of intrinsic Gilbert damping," Phys Rev Lett, vol. 102, no. 13, p. 137601, 2009.
[73] M. Fahnle and D. Steiauf, "Handbook of Magnetism and Advanced Magnetic Materials," New York, Wiley, vol. 1, 2007.

[74] K. Gilmore, Y. U. Idzerda, and M. D. Stiles, "Identification of the dominant precession-damping mechanism in Fe, Co, and Ni by first-principles calculations," Phys Rev Lett, vol. 99, no. 2, p. 027204, 2007.
[75] K. Zakeri et al., "Spin dynamics in ferromagnets: Gilbert damping and two-magnon scattering," Physical Review B, vol. 76, no. 10, p. 104416, 2007.
[76] "https://en.wikipedia.org/wiki/Faraday_effect," Faraday effect, En.wikipedia.org. (2018).
[77] J. A. C. Bland, M. J. Padgett, R. J. Butcher, and N. Bett, "An Intensity-Stabilized He-Ne-Laser for Measuring Small Magneto-Optic Kerr Rotations From Thin Ferromagnetic-Films," Journal of Physics E-Scientific Instruments, vol. 22, pp. 308-312, 1989.
[78] Z. J. Yang and M. R. Scheinfein, "Combined three-axis surface magneto-optical Kerr effects in the study of surface and ultrathin-film magnetism," Journal of Applied Physics, vol. 74, no. 11, pp. 6810-6823, 1993.
[79] A. V. Kimel, A. Kirilyuk, P. A. Usachev, R. V. Pisarev, A. M. Balbashov, and T. Rasing, "Ultrafast non-thermal control of magnetization by instantaneous photomagnetic pulses," Nature, vol. 435, no. 7042, pp. 655-657, 2005.
[80] A. Kirilyuk, A. V. Kimel, and T. Rasing, "Controlling spins with light," Philos Trans A Math Phys Eng Sci, vol. 369, no. 1951, pp. 3631-3645, 2011.
[81] P. S. Pershan, J. P. van der Ziel, and L. D. Malmstrom, "Theoretical Discussion of the Inverse Faraday Effect, Raman Scattering, and Related Phenomena," Physical Review, vol. 143, no. 2, pp. 574-583, 1966.
[82] C. Stamm et al., "Femtosecond modification of electron localization and transfer of angular momentum in nickel," Nat Mater, vol. 6, no. 10, pp. 740-743, 2007.
[83] A. R. Khorsand et al., "Role of magnetic circular dichroism in all-optical magnetic recording," Phys Rev Lett, vol. 108, no. 12, p. 127205, 2012.
[84] R. A. Beth, "Mechanical Detection and Measurement of the Angular Momentum of Light," Physical Review, vol. 50, no. 2, pp. 115-125, 1936.
[85] "https://en.wikipedia.org/wiki/Circular_polarization," Circular polarization, En.wikipedia.org. (2018).
[86] J. Stöhr, "Magnetism From Fundamental to Nanoscale Dynamics," Springer, 2006.
[87] M. Niemeyer et al., "Spin coupling and orbital angular momentum quenching in free iron clusters," Phys Rev Lett, vol. 108, no. 5, p. 057201, 2012.
[88] P. Carra, B. T. Thole, M. Altarelli, and X. Wang, "X-ray circular dichroism and local magnetic fields," Phys Rev Lett, vol. 70, no. 5, pp. 694-697, 1993.
[89] S. R. P. Gambardella, M. Veronese, S. S. Dhesi, C. Grazioli, A. Dallmeyer, I. Cabria, R. Zeller, P. H. Dederichs, K. Kern, C. Carbone, H. Brune, "Giant Magnetic Anisotropy of Single Cobalt Atoms and Nanoparticles," Science, vol. 300, p. 4, 2003.
[90] B. T. Thole, P. Carra, F. Sette, and G. van der Laan, "X-ray circular dichroism as a probe of orbital magnetization," Physical Review Letters, vol. 68, no. 12, pp. 1943-1946, 1992.

[91] J. T. Lau, A. Föhlisch, R. Nietubyć, M. Reif, and W. Wurth, "Size-Dependent Magnetism of Deposited Small Iron Clusters Studied by X-Ray Magnetic Circular Dichroism," Physical Review Letters, vol. 89, no. 5, p. 057201, 2002.
[92] C. B. K. W. Edmonds, S. H. Baker, S. C. Thornton, and C. Norris, "Doubling of the orbital magnetic moment in nanoscale Fe clusters," Physical Review B, vol. 60, pp. 472-476, 1999.
[93] J. Stohr, "Exploring the microscopic origin of magnetic anisotropies with X-ray magnetic circular dichroism (XMCD) spectroscopy," Journal of Magnetism and Magnetic Materials, vol. 200, pp. 470-497, 1999.
[94] K. Fauth, "https://www.researchgate.net/post/What_is_quenching_of_orbital_angular_momentum," ResearchGate, 2019.
[95] W. C. Koehler, "Magnetic Properties of Rare-Earth Metals and Alloys," Journal of Applied Physics, vol. 36, no. 3, pp. 1078-1087, 1965.
[96] L. Rettig et al., "Itinerant and Localized Magnetization Dynamics in Antiferromagnetic Ho," Phys Rev Lett, vol. 116, no. 25, p. 257202, 2016.
[97] H. C. S. Joachim Stöhr, "Magnetism From Fundamental to Nanoscale Dynamics," Springer, 2006.
[98] R. Schafer, "Investigation of Domains and Dynamics of Domain Walls by the Magneto-optical Kerr-effect," Handbook of Magnetism and Advanced Magnetic Materials, vol. 3, 2007.
[99] I. V. Soldatov and R. Schafer, "Selective sensitivity in Kerr microscopy," Rev Sci Instrum, vol. 88, no. 7, p. 073701, 2017.
[100] Z. B. H. Hujan, "Magneto–Optical Kerr Effect Microscopy Investigation on Permalloy Nanostructures," MSc Thesis, University of York, 2013.
[101] X. Lu, "Ultrafast Laser-induced Magnetisation Dynamics: Gilbert damping of Metal and Half-metal," Ph.D Thesis, University of York, 2018.
[102] M. S. E. Hadri, "Magnetization reversal mechanism leading to all-optical helicity dependent switching.," Ph.D Thesis, Université de Lorraine, 2016.
[103] R. M. M. Diegel, E. Halder, "360 degree domain wall investigation for sensor applications," IEEE Transactions on Magnetics, vol. 40, no. 4, pp. 2655-2657, 2004.
[104] L. K. Bogart, D. Atkinson, K. O'Shea, D. McGrouther, and S. McVitie, "Dependence of domain wall pinning potential landscapes on domain wall chirality and pinning site geometry in planar nanowires," Physical Review B, vol. 79, no. 5, 2009.
[105] Y. Gao et al., "Stochastic domain wall depinning in permalloy nanowires with various types of notches," AIP Advances, vol. 6, no. 12, p. 125124, 2016.
[106] Y. Gao et al., "Depinning of domain walls in permalloy nanowires with asymmetric notches," Sci Rep, vol. 6, p. 32617, 2016.
[107] S. Lepadatu and Y. B. Xu, "Direct observation of domain wall scattering in patterned Ni80Fe20 and Ni nanowires by current-voltage measurements," Phys Rev Lett, vol. 92, no. 12, p. 127201, 2004.
[108] S. Lepadatu, A. Vanhaverbeke, D. Atkinson, R. Allenspach, and C. H. Marrows, "Dependence of domain-wall depinning threshold current on pinning profile," Phys Rev Lett, vol. 102, no. 12, p. 127203, 2009.

[109] S. Lepadatu, J. Wu, and Y. B. Xu, "Current-induced magnetization switching in asymmetric necked wires," Applied Physics Letters, vol. 91, no. 6, p. 062512, 2007.
[110] P. Lendecke, R. Eiselt, G. Meier, and U. Merkt, "Temperature dependence of domain-wall depinning fields in constricted Permalloy nanowires," Journal of Applied Physics, vol. 103, no. 7, p. 073909, 2008.
[111] D. C. H. Ohno, F. Matsukura, T. Omiya, E. Abe, T. Dietl, Y. Ohno, K. Ohtani, "Electric-field control of ferromagnetism," Nature, vol. 408, p. 944, 2000.
[112] F. Matsukura, Y. Tokura, and H. Ohno, "Control of magnetism by electric fields," Nat Nanotechnol, vol. 10, no. 3, pp. 209-220, 2015.
[113] T. A. Moore, T. J. Hayward, D. H. Y. Tse, J. A. C. Bland, F. J. Castaño, and C. A. Ross, "Magnetization reversal in individual micrometer-sized polycrystalline Permalloy rings," Journal of Applied Physics, vol. 97, no. 6, p. 063910, 2005.
[114] S. Goolaup, S. C. Low, M. C. Sekhar, and W. S. Lew, "Dependence of pinning on domain wall spin structure and notch geometry," Journal of Physics: Conference Series, vol. 266, p. 012079, 2011.
[115] A. Pushp et al., "Domain wall trajectory determined by its fractional topological edge defects," Nature Physics, vol. 9, no. 8, pp. 505-511, 2013.
[116] D. Atkinson, D. S. Eastwood, and L. K. Bogart, "Controlling domain wall pinning in planar nanowires by selecting domain wall type and its application in a memory concept," Applied Physics Letters, vol. 92, no. 2, p. 022510, 2008.
[117] I. Will, A. Ding, and Y. Xu, "Proximity effect of magnetic permalloy nanoelements used to induce AMR changes in magnetic biosensor nanowires at specific receptor sites," Journal of Magnetism and Magnetic Materials, vol. 388, pp. 5-9, 2015.
[118] D. S. Eastwood, J. A. King, L. K. Bogart, H. Cramman, and D. Atkinson, "Chirality-dependent domain wall pinning in a multinotched planar nanowire and chirality preservation using transverse magnetic fields," Journal of Applied Physics, vol. 109, no. 1, p. 013903, 2011.
[119] M. Hayashi, L. Thomas, C. Rettner, R. Moriya, and S. S. P. Parkin, "Dynamics of domain wall depinning driven by a combination of direct and pulsed currents," Applied Physics Letters, vol. 92, no. 16, p. 162503, 2008.
[120] D. M. Burn and D. Atkinson, "Effective pinning energy landscape perturbations for propagating magnetic domain walls," Sci Rep, vol. 6, p. 34517, 2016.
[121] J. Akerman, M. Muñoz, M. Maicas, and J. L. Prieto, "Selective injection of magnetic domain walls in Permalloy nanostripes," Journal of Applied Physics, vol. 115, no. 18, p. 183909, 2014.
[122] J. Brandão et al., "Control of the magnetic vortex chirality in Permalloy nanowires with asymmetric notches," Journal of Applied Physics, vol. 116, no. 19, p. 193902, 2014.
[123] L. K. Bogart, D. S. Eastwood, and D. Atkinson, "The effect of geometrical confinement and chirality on domain wall pinning behavior in planar nanowires," Journal of Applied Physics, vol. 104, no. 3, p. 033904, 2008.

[124] W. Zhu et al., "Depinning of vortex domain walls from an asymmetric notch in a permalloy nanowire," Applied Physics Letters, vol. 101, no. 8, p. 082402, 2012.
[125] D. M. Burn and D. Atkinson, "Control of domain wall pinning by localised focused Ga + ion irradiation on Au capped NiFe nanowires," Journal of Applied Physics, vol. 116, no. 16, p. 163901, 2014.
[126] L. Serrano-Ramón et al., "Modification of domain-wall propagation in Co nanowires via Ga+ irradiation," The European Physical Journal B, vol. 86, no. 3, p. 30926, 2013.
[127] X. F. Hu et al., "Discontinuous properties of current-induced magnetic domain wall depinning," Sci Rep, vol. 3, p. 3080, 2013.
[128] Sutikno, "Optimization and Characterization of Electron Beam Resist Using Atomic Force Microscopy," Jurnal Pendidikan Fisika Indonesia, vol. 5, pp. 67-74, 2009.
[129] D. G. H. Shazia Yasin , H. Ahmed, "Comparison of MIBK/IPA and water/IPA as PMMA developers for electron beam nanolithography," Microelectronic Engineering, vol. 61–62, pp. 745–753, 2002.
[130] M. T. Bryan, D. Atkinson, and R. P. Cowburn, "Experimental study of the influence of edge roughness on magnetization switching in Permalloy nanostructures," Applied Physics Letters, vol. 85, no. 16, p. 3510, 2004.
[131] "http://mumax.github.io/."
[132] T. Schneider, A. A. Serga, B. Leven, B. Hillebrands, R. L. Stamps, and M. P. Kostylev, "Realization of spin-wave logic gates," Applied Physics Letters, vol. 92, no. 2, p. 022505, 2008.
[133] L. Bai, M. Kohda, and J. Nitta, "Observation of spin wave modes depending on a tunable periodic magnetic field," Applied Physics Letters, vol. 98, no. 17, p. 172508, 2011.
[134] L. Chen et al., "Emergence of anisotropic Gilbert damping in ultrathin Fe layers on GaAs(001)," Nature Physics, vol. 14, no. 5, pp. 490-494, 2018.
[135] M. A. W. Schoen et al., "Ultra-low magnetic damping of a metallic ferromagnet," Nature Physics, vol. 12, no. 9, pp. 839-842, 2016.
[136] M. Nakayama et al., "Spin transfer switching in TbCoFe / CoFeB / MgO / CoFeB / TbCoFe magnetic tunnel junctions with perpendicular magnetic anisotropy," Journal of Applied Physics, vol. 103, no. 7, p. 07A710, 2008.
[137] S. Mangin, D. Ravelosona, J. A. Katine, M. J. Carey, B. D. Terris, and E. E. Fullerton, "Current-induced magnetization reversal in nanopillars with perpendicular anisotropy," Nature Materials, vol. 5, no. 3, pp. 210-215, 2006.
[138] A. Capua, S.-h. Yang, T. Phung, and S. S. P. Parkin, "Determination of intrinsic damping of perpendicularly magnetized ultrathin films from time-resolved precessional magnetization measurements," Physical Review B, vol. 92, no. 22, p. 224402, 2015.
[139] A. Natarajarathinam, Z. R. Tadisina, T. Mewes, S. Watts, E. Chen, and S. Gupta, "Influence of capping layers on CoFeB anisotropy and damping," Journal of Applied Physics, vol. 112, no. 5, p. 053909, 2012.

[140] B. Liu et al., "Transient enhancement of magnetization damping in CoFeB film via pulsed laser excitation," Applied Physics Letters, vol. 109, no. 4, p. 042401, 2016.
[141] N. Mo et al., "Origins of the damping in perpendicular media: Three component ferromagnetic resonance linewidth in Co–Cr–Pt alloy films," Applied Physics Letters, vol. 92, no. 2, p. 022506, 2008.
[142] X. Lu, L. J. Atkinson, B. Kuerbanjiang, Y. Wang, and V. K. L. e. al., "Evidence of coupling between magnon excitation and the Gilbert damping in half-metallic oxides," arXiv:1710.10938v1, 2017.
[143] A. Ganguly et al., "Tunable Magnetization Dynamics in Interfacially Modified Ni81Fe19/Pt Bilayer Thin Film Microstructures," Sci Rep, vol. 5, p. 17596, 2015.
[144] P. He et al., "Quadratic scaling of intrinsic Gilbert damping with spin-orbital coupling in L10 FePdPt films: experiments and Ab initio calculations," Phys Rev Lett, vol. 110, no. 7, p. 077203, 2013.
[145] D. Guarisco, R. Burgermeister, C. Stamm, and F. Meier, "Magnetization reversal in the picosecond range measured with time‐resolved magneto‐optical Kerr effect," Applied Physics Letters, vol. 68, no. 12, pp. 1729-1731, 1996.
[146] B. Lenk, G. Eilers, J. Hamrle, and M. Münzenberg, "Spin-wave population in nickel after femtosecond laser pulse excitation," Physical Review B, vol. 82, no. 13, p. 134443, 2010.
[147] A. J. Schellekens, L. Deen, D. Wang, J. T. Kohlhepp, H. J. M. Swagten, and B. Koopmans, "Determining the Gilbert damping in perpendicularly magnetized Pt/Co/AlOx films," Applied Physics Letters, vol. 102, no. 8, p. 082405, 2013.
[148] Y. Hashimoto, S. Kobayashi, and H. Munekata, "Photoinduced precession of magnetization in ferromagnetic (Ga,Mn)As," Phys Rev Lett, vol. 100, no. 6, p. 067202, 2008.
[149] V. Kamberský, "Ferromagnetic Resonance Damping in Metals," Czech. J. Phys., Sect. B, vol. 26, p. 1366, 1976.
[150] S. Mizukami et al., "Gilbert damping in perpendicularly magnetized Pt/Co/Pt films investigated by all-optical pump-probe technique," Applied Physics Letters, vol. 96, no. 15, p. 152502, 2010.
[151] V. Kamberský, "On the Landau–Lifshitz relaxation in ferromagnetic metals," Canadian Journal of Physics, vol. 48, no. 24, pp. 2906-2911, 1970.
[152] P. Bruno, "Physical Origins and Theoretical Models of Magnetic Anisotropy," Ferienkurse des Forschungszentrums Jürich, Jürich, 1993.
[153] A. Barman, S. Wang, O. Hellwig, A. Berger, E. E. Fullerton, and H. Schmidt, "Ultrafast magnetization dynamics in high perpendicular anisotropy [Co／Pt]n multilayers," Journal of Applied Physics, vol. 101, no. 9, p. 09D102, 2007.
[154] P. Neilinger et al., "Ferromagnetic resonance study of sputtered Pt/Co/Pt multilayers," Applied Surface Science, vol. 461, pp. 202-205, 2018.
[155] J. W. K. a. F. Y. Yang, "Oscillatory interlayer coupling in Co/Pt multilayers with perpendicular anisotropy," Physical Review B, vol. 71, no. 224403, 2005.
[156] H. W. v. K. a. W. B. Zeper, "Controlling the Curie temperature of Co/Pt multilayer magneto-optical recording media," Journal of Magnetism and Magnetic Materials, vol. 120, pp. 271-273, 1993.

[157] Y. X. NIE Ying, ZHANG Pang, SANG Hai, "Magnetization and coercivity in Co/Pt multilayers with constant total Co layer thickness," Transcations of Nonferrous Metals Society of China, vol. 20, p. 6, 2010.
[158] S. Mizukami et al., "Long-lived ultrafast spin precession in manganese alloys films with a large perpendicular magnetic anisotropy," Phys Rev Lett, vol. 106, no. 11, p. 117201, 2011.
[159] S. Iihama, Q. Ma, T. Kubota, S. Mizukami, Y. Ando, and T. Miyazaki, "Damping of Magnetization Precession in Perpendicularly Magnetized CoFeB Alloy Thin Films," Applied Physics Express, vol. 5, no. 8, p. 083001, 2012.
[160] S. Mizukami, H. Abe, D. Watanabe, M. Oogane, Y. Ando, and T. Miyazaki, "Gilbert Damping for Various Ni80Fe20Thin Films Investigated Using All-Optical Pump–Probe Detection and Ferromagnetic Resonance," Applied Physics Express, vol. 1, p. 121301, 2008.
[161] Z. Chen, M. Yi, M. Chen, S. Li, S. Zhou, and T. Lai, "Spin waves and small intrinsic damping in an in-plane magnetized FePt film," Applied Physics Letters, vol. 101, no. 22, p. 222402, 2012.
[162] V. Grolier, J. Ferré, A. Maziewski, E. Stefanowicz, and D. Renard, "Magneto-optical anisometry of ultrathin cobalt films," Journal of Applied Physics, vol. 73, no. 10, pp. 5939-5941, 1993.
[163] F. Busse, M. Mansurova, B. Lenk, M. von der Ehe, and M. Munzenberg, "A scenario for magnonic spin-wave traps," Sci Rep, vol. 5, p. 12824, 2015.
[164] S. Mizukami et al., "Laser-Induced Fast Magnetization Precession and Gilbert Damping for CoCrPt Alloy Thin Films with Perpendicular Magnetic Anisotropy," Applied Physics Express, vol. 3, no. 12, p. 123001, 2010.
[165] M. S. El Hadri et al., "Domain size criterion for the observation of all-optical helicity-dependent switching in magnetic thin films," Physical Review B, vol. 94, no. 6, p. 064419 2016.
[166] P. J. Metaxas et al., "Creep and flow regimes of magnetic domain-wall motion in ultrathin Pt/Co/Pt films with perpendicular anisotropy," Phys Rev Lett, vol. 99, no. 21, p. 217208, 2007.
[167] Y. Xu, M. Deb, G. Malinowski, M. Hehn, W. Zhao, and S. Mangin, "Ultrafast Magnetization Manipulation Using Single Femtosecond Light and Hot-Electron Pulses," Adv Mater, vol. 29, no. 42, p. 1703474, 2017.
[168] G. Malinowski, K. C. Kuiper, R. Lavrijsen, H. J. M. Swagten, and B. Koopmans, "Magnetization dynamics and Gilbert damping in ultrathin Co48Fe32B20 films with out-of-plane anisotropy," Applied Physics Letters, vol. 94, no. 10, p. 102501, 2009.
[169] X. Zou, "Spin Dynamics of Magnetite and RE-TM Thin Films," Ph.D Thesis, University of York, 2010.
[170] A. J. Schellekens, L. Deen, D. Wang, J. T. Kohlhepp, H. J. M. Swagten, and B. Koopmans, "Determining the Gilbert damping in perpendicularly magnetized Pt/Co/AlOx films," Applied Physics Letters, vol. 102, no. 8, 2013.
[171] J. O. Rantschler et al., "Effect of 3d, 4d, and 5d transition metal doping on damping in permalloy thin films," Journal of Applied Physics, vol. 101, no. 3, p. 033911, 2007.

[172] G. Woltersdorf, M. Buess, B. Heinrich, and C. H. Back, "Time resolved magnetization dynamics of ultrathin Fe(001) films: spin-pumping and two-magnon scattering," Phys Rev Lett, vol. 95, no. 3, p. 037401, 2005.
[173] S. Azzawi et al., "Evolution of damping in ferromagnetic/nonmagnetic thin film bilayers as a function of nonmagnetic layer thickness," Physical Review B, vol. 93, no. 5, p. 054402, 2016.
[174] Y. Liu, Z. Yuan, R. J. Wesselink, A. A. Starikov, and P. J. Kelly, "Interface enhancement of Gilbert damping from first principles," Phys Rev Lett, vol. 113, no. 20, p. 207202, 2014.
[175] R. Urban, G. Woltersdorf, and B. Heinrich, "Gilbert damping in single and multilayer ultrathin films: role of interfaces in nonlocal spin dynamics," Phys Rev Lett, vol. 87, no. 21, p. 217204, 2001.
[176] A. H. Morrish, "The Physical Principles of Magnetism," New York: IEEE PRESS, 2001.
[177] Y. Yan, "Interface Magnetic Properties in Ferromagnetic Metal/Semiconductor and Related Heterostructures," Ph.D Thesis, University of York, 2017.
[178] J.-Y. Chen, L. He, J.-P. Wang, and M. Li, "All-Optical Switching of Magnetic Tunnel Junctions with Single Subpicosecond Laser Pulses," Physical Review Applied, vol. 7, no. 2, p. 021001, 2017.
[179] J. P. van der Ziel, P. S. Pershan, and L. D. Malmstrom, "Optically-Induced Magnetization Resulting from the Inverse Faraday Effect," Physical Review Letters, vol. 15, no. 5, pp. 190-193, 1965.
[180] C. D. Stanciu et al., "Ultrafast spin dynamics across compensation points in ferrimagneticGdFeCo: The role of angular momentum compensation," Physical Review B, vol. 73, no. 22, p. 220402, 2006.
[181] A. Kirilyuk, A. V. Kimel, and T. Rasing, "Laser-induced magnetization dynamics and reversal in ferrimagnetic alloys," Rep Prog Phys, vol. 76, no. 2, p. 026501, 2013.
[182] R. Chimata et al., "All-thermal switching of amorphous Gd-Fe alloys: Analysis of structural properties and magnetization dynamics," Physical Review B, vol. 92, no. 9, p. 094411, 2015.
[183] T. A. Ostler et al., "Ultrafast heating as a sufficient stimulus for magnetization reversal in a ferrimagnet," Nat Commun, vol. 3, p. 666, 2012.
[184] R. F. L. Evans, T. A. Ostler, R. W. Chantrell, I. Radu, and T. Rasing, "Ultrafast thermally induced magnetic switching in synthetic ferrimagnets," Applied Physics Letters, vol. 104, no. 8, p. 082410, 2014.
[185] R. B. Wilson, J. Gorchon, Y. Yang, C.-H. Lambert, S. Salahuddin, and J. Bokor, "Ultrafast magnetic switching of GdFeCo with electronic heat currents," Physical Review B, vol. 95, no. 18, p. 180409, 2017.
[186] U. Atxitia, T. A. Ostler, R. W. Chantrell, and O. Chubykalo-Fesenko, "Optimal electron, phonon, and magnetic characteristics for low energy thermally induced magnetization switching," Applied Physics Letters, vol. 107, no. 19, p. 192402, 2015.
[187] M. L. M. Lalieu, R. Lavrijsen, and B. Koopmans, "Integrating all-optical switching with spintronics," Nat Commun, vol. 10, no. 1, p. 110, 2019.

[188] Y. Tsema et al., "Helicity and field dependent magnetization dynamics of ferromagnetic Co/Pt multilayers," Applied Physics Letters, vol. 109, no. 7, p. 072405, 2016.
[189] K. Vahaplar et al., "All-optical magnetization reversal by circularly polarized laser pulses: Experiment and multiscale modeling," Physical Review B, vol. 85, no. 10, p. 104402, 2012.
[190] R. Moreno, T. A. Ostler, R. W. Chantrell, and O. Chubykalo-Fesenko, "Conditions for thermally induced all-optical switching in ferrimagnetic alloys: Modeling of TbCo," Physical Review B, vol. 96, no. 1, p. 014409, 2017.
[191] J. Gorchon, Y. Yang, and J. Bokor, "Model for multishot all-thermal all-optical switching in ferromagnets," Physical Review B, vol. 94, no. 2, p. 020409, 2016.
[192] J. Gorchon et al., "Single shot ultrafast all optical magnetization switching of ferromagnetic Co/Pt multilayers," Applied Physics Letters, vol. 111, no. 4, p. 042401, 2017.
[193] J. Gorchon et al., "Role of electron and phonon temperatures in the helicity-independent all-optical switching of GdFeCo," Physical Review B, vol. 94, no. 18, p. 184406, 2016.
[194] C. Schubert et al., "All-optical helicity dependent magnetic switching in an artificial zero moment magnet," Applied Physics Letters, vol. 104, no. 8, p. 082406, 2014.
[195] Y. Quessab et al., "Helicity-dependent all-optical domain wall motion in ferromagnetic thin films," Physical Review B, vol. 97, no. 5, p. 054419, 2018.
[196] N. Bergeard et al., "Hot-Electron-Induced Ultrafast Demagnetization in Co/Pt Multilayers," Phys Rev Lett, vol. 117, no. 14, p. 147203, 2016.
[197] A. Eschenlohr et al., "Ultrafast spin transport as key to femtosecond demagnetization," Nat Mater, vol. 12, no. 4, pp. 332-336, 2013.
[198] S. Iihama et al., "Single-Shot Multi-Level All-Optical Magnetization Switching Mediated by Spin Transport," Adv Mater, vol. 30, no. 51, p. e1804004, 2018.
[199] O. Hellwig, A. Berger, J. B. Kortright, and E. E. Fullerton, "Domain structure and magnetization reversal of antiferromagnetically coupled perpendicular anisotropy films," Journal of Magnetism and Magnetic Materials, vol. 319, no. 1-2, pp. 13-55, 2007.
[200] Y. Yan et al., "Element specific spin and orbital moments of nanoscale CoFeB amorphous thin films on GaAs(100)," AIP Advances, vol. 6, no. 9, p. 095011, 2016.
[201] M. Charilaou, C. Bordel, P. E. Berche, B. B. Maranville, P. Fischer, and F. Hellman, "Magnetic properties of ultrathin discontinuous Co/Pt multilayers: Comparison with short-range ordered and isotropicCoPt3films," Physical Review B, vol. 93, no. 22, p. 224408, 2016.
[202] T. K. J Valentin, D Weller, "Micromagnetic analysis of magnetization reversal in CoPt alloy films," Journal of Physics D: Applied Physics, vol. 29, p. 1111, 1996.
[203] R. Medapalli et al., "Multiscale dynamics of helicity-dependent all-optical magnetization reversal in ferromagnetic Co/Pt multilayers," Physical Review B, vol. 96, no. 22, 2017.

[204] M. Vomir, M. Albrecht, and J. Y. Bigot, "Single shot all optical switching of intrinsic micron size magnetic domains of a Pt/Co/Pt ferromagnetic stack," Applied Physics Letters, vol. 111, no. 24, p. 242404, 2017.
[205] F. Schlickeiser, U. Ritzmann, D. Hinzke, and U. Nowak, "Role of Entropy in Domain Wall Motion in Thermal Gradients," Phys Rev Lett, vol. 113, no. 9, p. 097201, 2014.
[206] J. Mendil et al., "Resolving the role of femtosecond heated electrons in ultrafast spin dynamics," Sci Rep, vol. 4, p. 3980, 2014.
[207] S. B. J. Gorchon, J. Ferré, V. Jeudy, A. B. Kolton, and T. Giamarchi, "Pinning-Dependent Field-Driven Domain Wall Dynamics and Thermal Scaling in an Ultrathin Pt/Co/Pt Magnetic Film," Phys Rev Lett, vol. 113, no. 2, p. 027205, 2014.
[208] G. P. Zhang, Z. Babyak, Y. Xue, Y. H. Bai, and T. F. George, "First-principles and model simulation of all-optical spin reversal," Physical Review B, vol. 96, no. 13, p. 134407, 2017.
[209] U. Keller, "Recent developments in compact ultrafast lasers," Nature, vol. 424, pp. 831-838, 2003.